An LES Wall Treatment

with a Self-Sustaining Model

by Jing Li

A dissertation submitted in partial fulfillment of
the requirements for the degree of
Doctor of Philosophy
(Mechanical Engineering)

at the

University of Wisconsin – Madison

2023

Date of final oral examination: 07/27/2023

The dissertation is approved by the following members of the Final Oral Committee:

Mario F. Trujillo, Professor, Mechanical Engineering
Mark Anderson, Associate Professor, Mechanical Engineering
Alejandro Roldan Alzate, Associate Professor, Biomedical Engineering
Sage Kokjohn, Associate Professor, Mechanical Engineering
Riccardo Bonazza, Professor, Mechanical Engineering

Abstract

A wall model has been developed for coarse meshed wall-bounded LES flows, to provide fluctuating wall shear stress by modeling a significant rolling phenomenon in a turbulent boundary layer. The rolls massively exist in the near-wall region to facilitate mass and momentum exchange. By analyzing the DNS near-wall flow field, relationships of rolls to fluctuating wall shear stress are extracted and used to convert dynamic rolling information, which is traced by updating the self-sustaining processing equations, into fluctuating wall shear stress. The above relationships and effectiveness of conversion have been verified and shown to match the statistics of the DNS near-wall flow.

This wall model is applied to every wall-adjacent cell, providing the desired wall shear stress to the LES solver in each iteration step. To evaluate the model's performance, a channel flow case is used, which includes verifying the force balance and checking the mean velocity profile. A comparison with a control group demonstrates improvements in near-wall fluctuations, TKE, and Reynolds stress. The velocity and total pressure contours confirm that this model provides more detailed fluctuations on walls. The test results on further mesh convergence and stretched grid indicate that the model performs reasonably well.

Acknowledgments

First, I would like to express my sincere gratitude to Professor Mario F. Trujillo for his great guidance, support, and encouragement in the past two years of supervision. I am deeply grateful for the time and effort that the professor has invested, especially, in spending a lot of time reviewing my thesis and providing valuable advice.

Second, to extend a special thanks to Professor Christopher J. Rutland for providing me with the opportunity to continue studying my favorite topic 5 years ago and for sharing his ideas in research, which have served as the backbone of my thesis. Professor's guidance, expertise, and dedication to academic excellence have been instrumental in shaping my research and academic growth. I am honored to have had the privilege of being his student.

Further, I would like to thank Professor Fabian Waleffe at the Mathematics Department at UW-Madison. The main theory applied in this proposal was developed by him. Invaluable suggestions and corrections were received from meetings with him. I also want to thank my prelim and oral committee members. They are professors Sage Kokjohn, Mark Anderson, Alejandro Roldan Alzate, and Riccardo Bonazza.

Additionally, Thanks to Dr. Hongjang Li, Dr. Yangdongfang Yang, Dr. Harsh Sapra, and all students in ERB-1008 for helpful suggestions and friendship. Special thanks to the ERC Computer Administrator Joshua Leach.

Finally, I would like to thank my patients for their love and support.

Funding for my study is partially provided by a TA position from the Department of Mechanical Engineering. Thanks for working with Jeff Roessler and Professor Krishnan Suresh about ME331. Thanks to Professor Xiaoping Qian my former advisor who transferred me to UW-Madison.

Thanks to ChatGPT, Grammarly, and Quillbot online Apps as free proofreading tools for checking and improving the grammar and overall quality of this thesis.

Table of Contents

List of Figures

List of Tables

Nomenclature

A, A^+	Model coefficients
B	A constant, of 5.2
C	A model constant
c_p	Model constant
$\mathbf{A}_k, \mathbf{C}_k$	Perturbation covariance
D	Damping coefficient
d	Wall distance
d_1	Wall distance from the center of the wall adjacent cell to a wall surface
$d_{p_0 z}$	The maximum value of total pressure gradient in the spanwise direction
d_Ω	Core vorticity wall distance
E	Spectrum energy
e^*, e^t	Errors
F_i	The left-hand side of the boundary layer equation
h	A wall distance, or a half-channel height
h_R, h_v	Model variables of heights wrt. rolling radius and viscous
k	Turbulent kinetic energy
L	Length of a channel
l_i	Downstream slip length
N_B^u	Shape functions
n	Wall normal unit vector
N_{DNS}, N_{LES}, N_{WMLES}	The computational cost of the DNS, LES, and WMLES
N_i, C_i, S_i	Vertices on wall cells, or patches
M	The magnitude of mean shear
M	Magnitude vector of mean shear, streaks, rolls, and instabilities

p	Pressure
p^+	A pressure gradient parameter
p_w	Wall pressure
p_0	Total pressure
Pr_t	A constant
R	A model coefficient (in Chapter 2), and a coefficient of determination (in Chapter 3)
R_{tau}	A model ratio
Re	Reynolds number
Re_τ	Friction Reynolds number
r	The radius of a roll
r^h	A ramp function
Δs	A streamwise displacement
S_{ij} , $\bar{S}_{ij}$	Mean rates of strain
s_i	The path length of vertices
s_1	Pressure source term
t	Time
T_{ij} , T_{yy} ,	Reynolds stress, and its components
U	Far-field velocity(in Chapter 2), mean velocity (in Chapter 2), and the Magnitude of streaks
$u_{\|\|}$	The velocity of the wall parallel component
u_{bulk}	A bulk velocity of a channel flow
u_i , u_j , u_k	Velocity components
u_τ	Friction velocity
u^+	Dimensionless velocity
u'	Fluctuating velocity
u_p	A pressure-viscosity velocity

$\bar{\mathbf{u}}_h, \tilde{\mathbf{u}}_h$	Discrete velocity, represented as a conventional polynomial component, and an enrichment component
V	Magnitude of rolls
$\mathbf{u}_1, v_1$	Velocities at the center of a wall-adjacent cell
$\mathbf{u}_w$	Wall velocity
v_∞	Velocity at the far field, or the center of the channel flow
v_H , v_L	High- / low-speed flow
x_i , x_j , x_k	Coordinates
x', y', z'	Coordinates in a parametric domain
$\hat{v}_k$	Fourier expansion of the velocity perturbation fields
W	The magnitude of instabilities, or a channel width
Δx	Grid size
y , y^+	Coordinates, wall-normal direction, in the physical and plus units
y_1	Distance from the center of a wall-adjacent cell to a wall
y_m^+	A Werner & Wengle model constant
Δy	Wall-adjacent cell height

Greek letters:

α	A wave number
α_τ	A wall model coefficient
$\sigma_m, \sigma_u, \sigma_v, \sigma_w$	The SSP model coefficients
β	A wave number
$\hat{\boldsymbol{\phi}}_k$	Fourier expansion of the perturbation fields
Φ_{011}	A rolling mode
γ	A linear growth angle, or a wave number

δ	Boundary layer thickness,
δ_v	Boundary layer viscous length scale
δ_{ij}	Kronecker delta
Δ_{shear}	The magnitude of fluctuating wall shear stress
$\hat{\eta}_k$	Fourier expansion of the vorticity perturbation fields
κ	The Von Karman constant, 0.41
κ_m , κ_u , κ_v , κ_w	The SSP model coefficients
$\mu_{t,wm}$	Wall modeled turbulent viscosity
ν	Kinematic molecular viscosity
ν_t	Turbulent viscosity
$\nu_{t,wm}$	Wall modeled turbulent viscosity
$\mathbf{\Gamma}$	Lyapunov equation
τ	Shear stress
τ_w	Wall shear stress
$\overline{\tau}_w$	Averaged wall shear stress
$\overline{\tau}_{w,L}$, $\overline{\tau}_{w,R}$	Averaged wall shear stress from the spanwise left/right side cells
$\tau_{w,i}$	Components of wall shear stress
$\hat{\tau}_{w,i}$	Wall shear stress on the i-th vertex of a wall patch
τ_{ij}^{RANS}	Tensile stress
$\Omega_{\max}$	The core vorticity
ψ	An enrichment function
$\mathbf{\Psi}$	A stream function

Operators and functions

$F_0(\cdot)$, $\Phi(\cdot)$	Universal non-dimensional functions
loglaw(d), $f_{profile}(\cdot)$	Velocity profile function
$p_{PDF}(\tau_w)$	A piecewise fitted PDF curve function
$s_{PDF}(\tau_w)$	Arc length function
$\tilde{\phi}(\mathbf{x},t)$	Filtering function
$\langle\cdot\rangle$	Time average
$\langle\cdot\rangle_{xz}$	Averaging across the xz-plate
$(\cdot)$	Spatial average
$\overline{(\cdot)}$	Ensemble average
$(\cdot)$	Curve fitting predictor
$\|\cdot\|$	Distance
∇	Gradient

Chapter 1 Introduction

1.1 Motivations

Large-Eddy Simulation (LES) solves large energy-carrying motions while also modeling smaller unresolved eddies. However, the size of eddies in a given flow is directly linked to the scales where the majority of turbulent kinetic energy is concentrated. In the case of wall turbulence, this scale gradually reduces toward a wall, which forces the LES to resolve up to the smallest dissipating eddies at a very near wall. The length scale of these energetic eddies is comparable to the resolution of Direct Numerical Simulation (DNS), which is why the LES method is so computationally expensive when dealing with high Reynolds-number wall flows.

However, when a coarse LES mesh is used in combination with a SubGrid-Scale (SGS) model, the mean velocities of the near-wall grid points are frequently predicted poorly, not to mention their fluctuations. This poor prediction happens in the attached boundary layers and may be even more severe in complicated flows that involve adverse pressure gradients.

Since adding more grid points is not feasible, an alternative approach known as Wall Modeled Large-Eddy Simulation (WMLES) has been developed. This approach involves augmenting the shear stress directly (wall modeling) while maintaining a coarse grid WMLES models the transport of momentum from the inner to the outer layer and only resolves the outer layer, leaving the inner layer modeled. According to Choi & Moin [1], the computing cost of WMLES is proportional to the Reynolds number ($N_{WMLES} \sim \mathrm{Re}^{1.0}$) of the problem. Compared to the DNS and resolved LES, WMLEWS provides savings of 1-2 orders of magnitude,

$N_{DNS} \sim \mathrm{Re}^{37/14}$ and $N_{LES} \sim \mathrm{Re}^{13/7}$, making it a practical option for high Reynolds-number engineering applications.

1.2 Overview

Instead of being resolved like in a traditional LES, turbulent motions in the inner layer are modeled in the WMLES. Wall models can be classified into two types [2]: (1) wall stress modeling and (2) hybrid LES/RANS. Wall stress modeling enables LES to occupy the entire computational domain down to the wall, and the wall models and equations are kept separate from the LES solution. In contrast, the hybrid technique divides the computational domain into two sub-domains. The LES subdomain occupies the outer majority of a turbulent boundary layer, while the RANS subdomain dominates the inner layer. The two subdomains communicate through a specific interface.

Wall stress modeling methods provide the boundary condition of the LES domain that extends to the wall, ensuring the correct value of the wall shear stress τ_w. Two techniques are available based on how this τ_w is computed. The majority of approaches are RANS-based approaches, while the other approaches include various existing methods. RANS-based approaches may solve full RANS equations, which results in PDE-based wall stress modeling models, or they may incorporate simplifications that lead to ODE or algebraic formulations. But each of these equations is discretized separately from the LES domain discretization.

There are two types of hybrid LES/RANS wall models: (1) zonal [3][4], and (2) seamless approaches [5]. Zonal approaches need interface locations, with either LES or RANS equations solved in a distinct computational domain. Seamless techniques, on the other hand, use a byproduct

of the solution or grid size to decide which equations to solve, rather than relying on an explicit interface. A Detached Eddy Simulation (DES) [6] with a grid designed to relocate an interface down towards the wall is a feasible seamless method because its RANS region fills the inner layer rather than the entire boundary layer. Further Delayed-DES (DDES) [7] and Improved Delayed-DES (IDDES) [8] were created to offer superior wall modeling capabilities.

Additional approaches include using data-driven neural networks [9], constructing a target velocity profile through control-based strategies to achieve a desired wall-parallel shear stress [10], implementing dynamic slip boundary condition models [11][12], and using a function enrichment model [13],.

1.3 Challenges

The WMLES was first attempted in the early 1970s [14][15] and underwent significant development around 2000 [16][17], becoming increasingly popular in recent years [2]. Various RANS-based models share a principal idea of savings that only resolve a turbulent boundary layer via a gradual decrease of the wall-normal extent of the grid towards the wall. However, this simplification ignores wall parallel resolution, especially in the spanwise direction, which is significant for capturing streamwise rolls, a major mechanism of momentum exchange in a near-wall region. As a result, it is unable to identify velocity fluctuations as significant LES quantities. In 2016, Park & Moin[18], employed a grid of wall-parallel resolutions $\frac{\Delta x}{\delta} \leq 0.05$ to conclude that (1) the WMLES's pressure fluctuations are recovered within a few percent of the DNS, but (2) the skin friction fluctuations continue to be underestimated. These findings confirm the validity of the

approximation $\frac{\partial p}{\partial y} = 0$, simplified from the wall-normal momentum equation, at high Reynolds, indicating that pressure fluctuation can be imposed from the outer layer. Meanwhile, near-wall eddies (or rolling structures) are connected to fluctuations in skin friction or wall shear stress.

Section 3.1 concludes that filtered solutions obtained from a low-resolution wall-parallel grid are inadequate in capturing both the magnitude and the probability density distribution of fluctuations. To address this issue, an attempt is made to model rolling effects toward wall shear, allowing for the generation of reasonable fluctuating wall shear stress values on coarse-gridded walls while maintaining a low computational cost.

The present study assumes that near-wall rolls are responsible for interchanging different speed flows in the wall-normal direction, causing velocity variation that results in fluctuating wall shear stresses. A wall model is proposed and calibrated using both a self-sustaining process (SSP) from Waleffe and Hamilton (1997) [19][20][21], and statistical data. There are difficulties in (1) practical implementation of the SSP, which uses low-order truncations to describe the x-independent flow, massively on a coarsely meshed wall boundary; (2) checking and calibrating the model to ensure it functions as intended and produces reasonable results that are close to statistical data; and (3) maintaining simplicity, physically clarity, and computationally efficiency.

Before proceeding to the subsequent sections, it is acknowledged in this thesis that the rolling mechanism is still under investigation [22][23][24][25]. Conversely, the SSP has been appropriately conceptualized, and experimentally verified [26], and has garnered subsequent [27] and related studies [28]. The proposed wall model based on this SSP shows promise.

1.4 Objectives

An ideal wall model should produce reasonable $\overline{\boldsymbol{\tau}}_w$ values at each time step of the simulation while accounting for the fluctuating components of wall shear stress in LES as they become critical, especially when coarse near-wall grid smoothing solutions considerably. Modeling these fluctuations may increase simulation accuracy overall, therefore, this thesis develops a novel approach to constructing a wall model that takes into consideration the near-wall rolling features that lead to the fluctuation of wall shear stress.

This thesis studies near-wall rolls in DNS channel flow and establishes statistical connections between rolls and fluctuations to enhance the proposed wall model. These statistical relationships are revealed by using pairs of roll and fluctuation samples that were detected and measured from the channel flow. Nevertheless, coarse grid resolution in a practical case tends to smooth out rolls, so this thesis intends to find an indicator in such a coarse solution field that can detect a probable rolling tendency for subsequent modeling of fluctuations.

The SSP model is employed to update near-wall rolling information. However, before incorporating it into the wall model, this thesis must offer adequate evidence that the SSP results accurately reflect wall-bounded shear flow. This SSP, originally derived from free shear flow, uses truncated modes to represent flows, which may result in errors when applied to a wall-bounded flow scenario. As a result, calibration and validation are necessary, requiring a suitable dynamic test case to revise the model and compare it to evaluate its performance.

The proposed LES wall model in this thesis considers the influence of near-wall rolling structures, which are typically filtered out in coarse meshes. However, the suggested method relies

on an independent dynamic system (SSP) to preserve these rolling characteristics outside the LES solver and translates them into fluctuating wall shear stress using statistical expressions from DNS. This approach is cost-effective and suitable for adjusting wall boundary conditions in coarse mesh simulations. Validation tests are conducted, and results are compared and explained to evaluate this proposed wall model.

1.5 Organization

The following is how this thesis is structured: Chapter 2 is a literature review that includes an introduction to turbulent boundary flow and wall shear stress concepts, as well as an overview of existing wall models, including wall shear stress and hybrid models. This chapter also discussed coherent structures, self-sustaining processes, and various models. Chapter 3 describes near-wall rolling structures in a DNS field, including the lifespan of rolls and their spatial association with fluctuating wall shear stress. The statistical relationship between rolls and total pressure gradient is also presented. The approach for abstracting the above relationships is provided at the end. Chapter 4 mainly focuses on the modeling of fluctuating wall shear stress, which is based on the assumption that near-wall rolls induce fluctuations. This chapter explains the SSP procedure and how LES field solutions are used to evaluate rolling magnitudes in this wall model. The amplitude of a roll is converted to the magnitude of fluctuation, which is then allocated to LES boundary conditions using statistical relationships. Chapter 5 validates the wall model with two tests. The first test traces changes in rolling magnitude and compares the modeled magnitudes of fluctuations to statistical curves for certain rolling sizes. The subsequent LES-coupled tests compare channel flow results, including force balance, mesh convergence, computational costs, and performance on meshes with wide spanwise spacing. This chapter also highlights the model's strengths,

weaknesses, and potential for improvement. Chapter 6 concludes this thesis and discusses potential future work.

Chapter 2 Literature Review

Wall models bypass resolving the near-wall region by using a large grid spacing grid to model flow or wall boundary conditions in the computational domain. In realistic high Reynolds wall-bounded flow, the reduction of grid points and corresponding larger computational time steps in WMLES may lead to a factor of a hundred-fold saving in the time-to-solution [1]. However, the modeled field differs from the realistic one which brings errors to the entire flow.

This chapter introduces boundary layer structures in 2.1.1, wall shear stress characteristics in 2.1.2, and near-wall coherent structures in 2.1.3 to better understand the turbulent boundary layer. Then, in section 2.2, current wall models are classified and briefly reviewed. Section 2.3 discusses the dynamic balance between energy production and dissipation in the turbulent boundary layer, including a self-sustaining mechanism and different available modeling methodologies.

2.1 Turbulent boundary layer

This section outlines the properties of turbulent boundary layers. A fully developed turbulent boundary layer is composed of multiple layers, each with different properties related to viscosity and Reynolds stress. Near the wall, there exist coherent structures that aid in the transfer of momentum and the exchange of distinct vertical flow layers, resulting in the generation of velocity fluctuations.

2.1.1 Structure of turbulent boundary layers

Depending on whether viscosity plays a significant role in physics, a turbulent boundary layer can be divided into two zones that overlap. In Figure 1, both the left orange (inner) and right light yellow (outer) regions are represented in two coordinates scaled by U, δ, or u_τ, δ_ν, where U, δ denotes the freestream velocity and a boundary layer thickness, respectively. The friction velocity is defined as $u_\tau = \sqrt{\tau_w / \rho}$, and a viscous length scale $\delta_\nu = \nu / u_\tau$, where the τ_w is a wall shear stress, ρ and ν denote the density and viscosity of the fluid. At high Reynolds numbers, there is a region of overlap between the two zones, defined [29] by $y^+ > 50$ and $y/\delta < 0.1$.

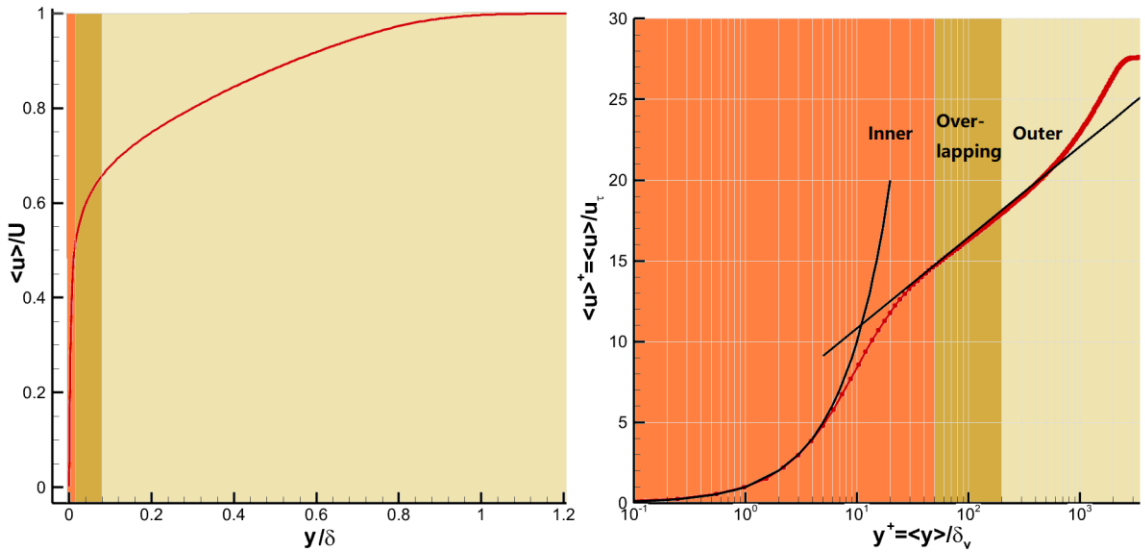

Figure 1: Regions of a turbulent boundary layer and velocity profiles

Figure 1 displays a red curve that represents a DNS mean velocity profile of a channel flow [30]. In a fully developed channel flow, this profile is completely determined by $\rho, \nu, \delta, u_\tau$ in expression (2.1).

$$\langle u \rangle = u_\tau F_0 \left(\frac{y}{\delta}, \mathrm{Re}_\tau \right) \tag{2.1}$$

The above F_0 is a universal non-dimensional function and $\mathrm{Re}_\tau = \delta / \delta_\nu$ is a friction Reynolds number. To derive the mean velocity profile, this expression (2.1) related to two non-dimensional parameters is written in terms $d\langle u \rangle / dy$ on the left-hand side

$$\frac{d\langle u \rangle}{dy} = \frac{u_\tau}{y} \Phi \left(\frac{y}{\delta_\nu}, \frac{y}{\delta} \right) \tag{2.2}$$

where Φ is another universal non-dimensional function. Depending on whether viscosity is dominant, simplification of either disregarding the y/δ term or vanishing dependency of y/δ_ν leads to a linear and log-law section of curves, respectively. Refer to Figure 1 for the black curves, their expressions are given in (2.3), and a detailed derivation in [29].

$$\begin{aligned} & u^+ = y^+, \quad y^+ < 8 \\ & u^+ = \frac{1}{\kappa} \ln y^+ + B, \quad y^+ > 30, \quad \text{where} \quad \kappa = 0.41, B = 5.2 \\ & \left(u^+ = \frac{u}{u_\tau}, \quad y^+ = \frac{y u_\tau}{\nu} \right) \end{aligned} \tag{2.3}$$

Research continues on the inner and outer interactions as well as the mechanisms of wall-attached eddies in the buffer layer $8 < y^+ < 30$. Numerous types of wall-attached eddies have been identified in the literature [31][32][33], such as horseshoe vortexes, hairpin vortexes, loop vortexes, and very large-scale motions (VLSMs). Section 2.1.3 will provide an overview of coherent structures.

Regarding interactions, classical theory [34] concurs that flows in both the inner and outer layers are independent until they asymptotically converge to the same one at the overlap zone.

However, a recent viewpoint [35] proposes that the physics in the outer and inner layers are unidirectionally coupled, which implies that flow in the outer layer is independent but has an impact on the inner layer.

2.1.2 Wall shear stresses

Since the mean pressure gradient is constant throughout the flow, $\frac{\partial \langle p \rangle}{\partial x} = \frac{dp_w}{dx}$, the streamwise direction of a channel flow may be described by a simplified mean-momentum equation

$$0 = \nu \frac{d^2 \langle u \rangle}{dy^2} - \frac{d}{dy} \langle u'v' \rangle - \frac{1}{\rho} \frac{d \langle p \rangle}{dx} \tag{2.4}$$

which can be rewritten as $\frac{d\tau}{dy} = \frac{dp_w}{dx}$, where the magnitude of shear stress as a function of wall distance $\tau(y)$ is

$$\tau = \rho \nu \frac{d \langle u \rangle}{dy} - \rho \langle u'v' \rangle \tag{2.5}$$

The viscous stress, $\rho \nu \, d\langle u \rangle / dy$, and the Reynolds stress, $-\rho \langle u'v' \rangle$, are two components of this stress. Figure 2 displays the changes in each in relation to wall distance, where the boundary condition $\mathbf{u}|_w = \mathbf{0}$ suppresses all Reynolds stresses in the near-wall region, leaving only the viscous contribution for the wall shear stress

$$\tau_w \approx \nu \left. \frac{d \langle u \rangle}{dy} \right|_w \tag{2.6}$$

When simulating with a fine mesh, the above viscous approximation is numerically accurate. However, if a coarse near-wall grid is used, applying the no-slip (Dirichlet) boundary condition may result in an underestimation of wall shear stress. This is because the inner layer grid is poorly resolved, resulting in underestimated field velocities. Thus, it is preferable to use the correct wall-shear stress (a Neumann boundary condition) instead.

The equilibrium assumption is another aspect of fluctuations that must be taken into account. This assumption asserts that the near-wall shear stress distribution is in equilibrium with the shear stress at the wall, However, it is not appropriate for transient simulations because of turbulent fluctuations and the possibility of local detached flow in complex situations. Refer to Figure 4 of the shear stress distribution that there is an up to 20% fluctuation of wall shear stress in a 10% near-wall region. Meanwhile, the Reynolds stresses and Turbulent Kinetic energy (TKE) as functions of outer region boundary-layer scaling in Figure 3 reveal the peak value of $\overline{u'^2}^+$, as a main component of TKE, occurring at a near-wall position below 10% of the boundary layer thickness. These findings are based on fine mesh numerical results.

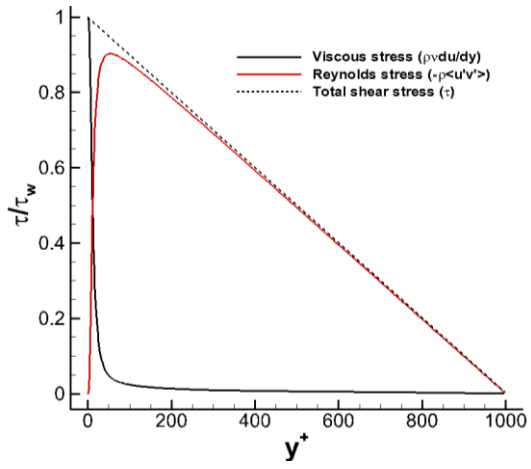

Figure 2: Reynolds shear stress and viscous changes in turbulent channel flow, from [30]

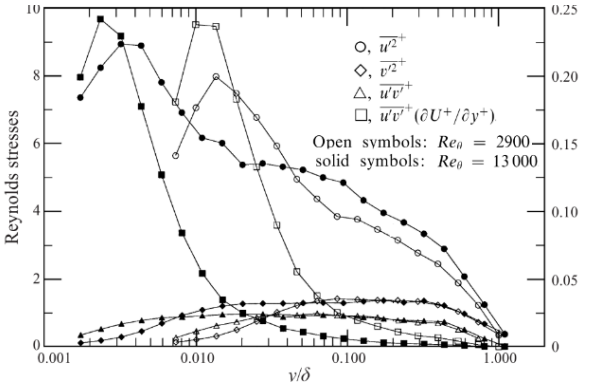

Figure 3: Reynolds stress and TKE, from [36]

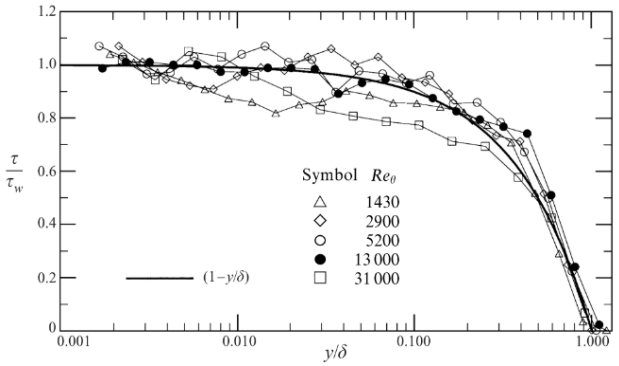

Figure 4: Shear stress distribution, from [36]

2.1.3 coherent structures

Coherent structures, such as individual hairpin vortex [37], symmetric hairpins [38], asymmetric hairpins (cane vortices), and horseshoes [31], can account for the above fluctuating features in the near-wall region, particularly under $y^+ \sim 100$, where the mixed contributions of viscous and Reynolds shear stress are observed in Figure 2. Figure 5 illustrates the hairpin vortex, as depicted by numerical studies [39]. The main hairpin is generated by enclosing a packet of low-speed fluid, which has a ramp-like shape with a linear growth angle γ. The swirling intensity of the hairpin vortex downstream as a result. Additional hairpins are generated behind the primary one if the strength of this current vortex is sufficient.

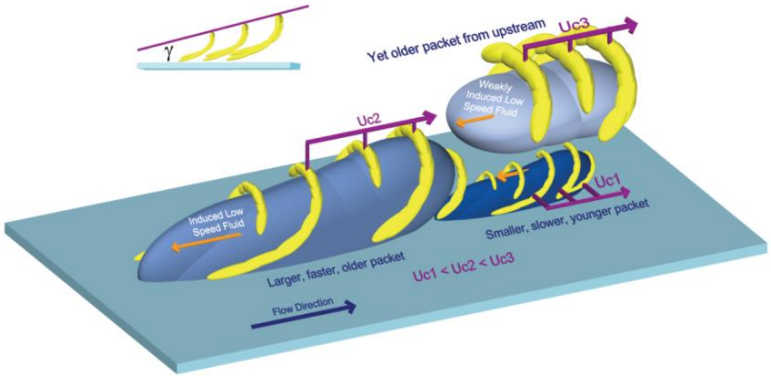

Figure 5: Conceptual scenario of hairpin vortices in the near-wall region, from [39]

A detailed description of the bursting sequence and the growth of hairpins is available in [32]. However, this study is primarily focused on a near-wall region at around $y^+ \sim 100$, which corresponds to the leg of hairpins. According to Zhou et al. [40], young hairpins are closely packed on the wall, with approximately 100-200 viscous units between the legs. Head et al. [37] report that hairpins have diameters on the order of 100 viscous units. As a result, Figure 6 illustrates a simplified model in which two streamwise counter-rotating vortices represent hairpin legs dominating the near-wall flow.

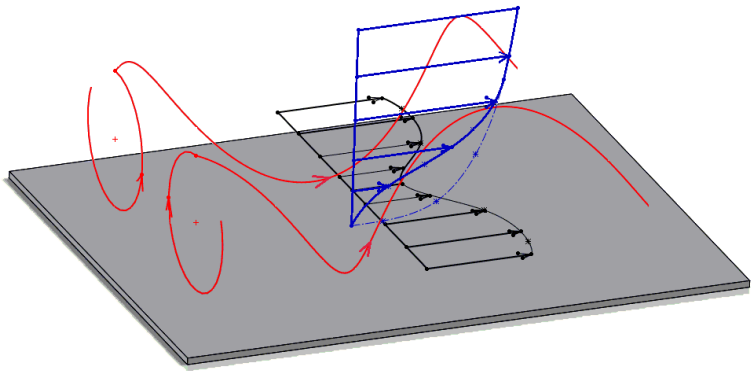

Figure 6: A pair of counter-rotating rolls and induced velocity variations (a similar Figure 7.42 in [29])

In the sketch above, these counter-rotating rolls assist in ejecting low-speed fluid away from the wall (ejection) as well as sweeping high-speed fluid toward the wall (sweep). This results in alternating low- and high-speed fluid, elongating in the streamwise direction along the spanwise direction, which is known as streaky flow. If this streaky flow takes on a shape of $\left[u(y,z),0,0\right]$, it is known as a streamwise streak, $\left[u(y,z)-\langle u(y)\rangle,0,0\right]$.

The aforementioned streak-roll interaction has been observed not only in numerical simulations [41][42] but also in experimental research [37] [43]. Additionally, Bakewell et al. [44] and Kline et al. [32] have shown that streaks are present in the region where $y^+ < 40$, and rolls are spaced approximately 100 wall viscous units apart in the spanwise direction. Streaks and rolls are both crucial features of a boundary layer [26] [45]. They dominate large-scale motion in the near-wall region ($y^+ < 100$) [44] and contribute to the conversion of kinetic energy from the mean flow to turbulent fluctuations.

2.2 Existing wall models

A comprehensive knowledge of the turbulent boundary layer is essential to construct a model with improved accuracy of the simulation. Based on how modeled near-wall layers are coupled with the resolved LES field, a variety of physics-based wall models have been developed and can be categorized into two types [2]: (1) wall stress modeling and (2) hybrid LES/RANS. Additionally, this section will discuss some non-physics-based techniques. Each model is introduced briefly, providing background information, its applications, as well as any notes or remarks.

2.2.1 Wall stress models

RANS-based models avoid resolving turbulence in the near-wall region by utilizing wall-model equations, denoted as (2.7)

$$\frac{\partial \langle u_i \rangle}{\partial t} + \frac{\partial \langle u_i \rangle \langle u_j \rangle}{\partial x_j} + \frac{\partial \langle p \rangle}{\partial x_i} = \frac{\partial}{\partial x_j}\left(\tau_{ij}^{RANS} + 2\nu \langle S_{ij} \rangle\right) \tag{2.7}$$

This equation is solved on a separate grid with the wall-normal direction refinement, which is located from a wall up to a specified distance h into the LES domain. The LES solution is sampled along the edges h to serve as a boundary condition for solving (2.7), and the wall shear stress computed from the solution (2.7) is fed back into the LES.

The aforementioned equation (2.7) holds for any turbulent boundary layer that has a flow of constant density. Different additional simplifications can be used to generate, PDE, ODE, and algebraic models.

PDE-based wall-stress models

Wang & Moin [46] used the mixing-length eddy viscosity model with near-wall damping to solve the equation (2.7)

$$\tau_{ij}^{RANS} = 2\nu_{t,wm}, \quad \nu_{t,wm} = \kappa \nu y_w^+ \left(1 - e^{-y_w^+/A}\right)^2 \tag{2.8}$$

where $y_w^+ = y u_\tau / \nu$ is a distance from the wall calculated using the local instantaneous friction velocity, u_τ. κ and A are model coefficients. Their research makes accurate predictions for low-order velocity statistics, consistent unsteady trailing–edge separation, and promising frequency spectra of surface pressure fluctuations. However, since it would only account for the unresolved

portion of the Reynolds stress, this model tends to overpredict the near-wall eddy viscosity. Cabot & Moin [47] also noted the significant Reynolds stress and proposed dynamically computing the model coefficient κ by matching the stress between the solutions from the inner and outer layers. Later, Kawai & Larsson [48] enhanced model consistency at a higher Reynolds number. Park & Moin [49] introduced this model into a fully unstructured mesh environment [49][50] and dynamically regulated the eddy viscosity based on the physical and mathematical constraints on the total Reynolds stress.

Additionally, these PDE-based approaches have been used in studies with complex geometries [51], and with high Reynolds separating flows [52]. Theoretically, these PDE-based models can account for transient, convective, and pressure-gradient effects. However, the drawbacks include (1) high computational cost. The ratio of the number of cells in the wall model to those in the LES is around 0.2-0.5 [50]; (2) it is difficult for users to mesh a near-wall grid. This grid should have full connectivity in all coordinate directions, provides a significant challenge in realistic and complicated geometries [2], and (3) be comparatively hard to implement.

ODE-based wall-stress models

It is possible to simplify the equation (2.7) to an unsteady thin boundary layer equation (TBLE) [47][53]

$$\frac{\partial \langle u_i \rangle}{\partial t} + \frac{\partial \langle u_i \rangle \langle u_j \rangle}{\partial x_j} + \frac{\partial \langle p \rangle}{\partial x_i} = \frac{\partial}{\partial y}\left[\left(\nu + \nu_t \right) \frac{\partial \langle u_i \rangle}{\partial y} \right] \tag{2.9}$$

Effects of unsteady (acceleration), convective, and pressure gradient are each represented by terms in the LHS of the equation (2.9). Some of these terms may not be taken into account in specific simplifications. The simplest approach sets all terms to zero as the so-called equilibrium

ODE/stress balance model, which is numerically at the least expensive and equivalent to the instantaneous log law model in the attached flow [47]. Hoffmann & Benocci [54] ignore the convective term and get improved results in the plane periodic channel case. There are similar studies that discuss the effects of the pressure gradient term. Wang [55] and Catalano et al. [56] retain only this term to simulate flows over a trailing edge and a circular cylinder, respectively. Duprat et al. [57] compare with/without the pressure gradient term in both channel and periodic hill cases. Chen et al. [58] apply this model with an immersed-interface method to complex geometries.

The integrated model [59] is based on the assumption that the LHS of the equation (2.9) is y-independent, designated as F_i, and an integral of $F_i = \frac{\partial}{\partial y}\left[\left(\nu + \nu_t\right) \frac{\partial \langle u_i \rangle}{\partial y} \right]$ is given

$$\left[\left(\nu + \nu_t\right) \frac{\partial \langle u_i \rangle}{\partial y} \right] = F_i y + C \tag{2.10}$$

where a constant C is determined at a wall $y = 0$: $\nu \frac{\partial \langle u_i \rangle}{\partial y} = C, \quad C = \langle \tau_{w,i} \rangle$. The wall shear stresses are obtained by integrating both sides (2.10)

$$\langle \tau_{w,i} \rangle = \left(\langle u_i \rangle \big|_h - F_i \int_0^h \frac{y}{\nu + \nu_t} dy \right) \Bigg/ \int_0^h \frac{dy}{\nu + \nu_t} \tag{2.11}$$

Because only the wall-normal direction is considered, the numerical integration from a wall to a height h in a 1D grid is possible. $\overline{u}_i$ is a good approximation of $\langle u_i \rangle$. The advantages of this approach are stability and low computing cost because numerical integration won't diverge and doesn't require iteration. As an alternative to numerical integration of the boundary layer equations,

Yang et al. [60] present a velocity profile with a viscous and a logarithmic layer of an extra linear term that accounts for pressure gradient effects.

Because the pressure gradient is in balance with others, Larsson et al. [2] recommended keeping all of the terms on the LHS of the equation (2.9). Additionally, Hickel et al. [61] recommended keeping the convective term for wall-parallel derivatives inside the embedded grid for a consistent reason. Their study modeled the convective term as either a function of velocity or a linear profile that matches the pressure gradient. Research into modeling the time derivative/temporal evolution is limited since this component adds a significant computational cost. Hoffmann & Benocci [54], however, did provide some provided some insight into how this temporal term was handled with.

To summarize, most ODE-based models need at least a 1D grid solver to respect y^+. They provided diverse physical modeling capabilities, based on distinct simplifications, but at a significantly lower computational cost than PDE models. Topics such as integral models, handling non-equilibrium terms, and dynamical eddy viscosity are still being researched [49].

Algebraic models

The equilibrium assumption is commonly used in algebraic models. Schuman [15] calculated wall shear stress by relating LES velocity to mean stress.

$$\tau_{w,x}\left(x,z\right)=\left\langle \tau_w \right\rangle \frac{\tilde{u}(x,y_1,z)}{\left\langle \tilde{u}(x,y_1,z)\right\rangle_{xz}} \tag{2.12}$$

where "$\tilde{}$" specifies a filtered value from the LES field, the subscription "1" indicates a value from the wall adjacent cell, and the xz-plane-wide spatial average of the data is represented by $\left\langle \bullet \right\rangle_{xz}$. The

mean stress $\langle \tau_w \rangle$ can either be predefined [15] or evaluated [62] using the log-law profile. This $\langle \tau_w \rangle$ evaluating process starts with sampling the LES solution from a certain wall distance h, then this solution is plugged into the log law velocity profile, and lastly, the result $\langle \tau_w \rangle$ is solved. Profiles covering a wider range, even below the log law, such as Reichard's law [63] and Spalind's law [64], are alternatives.

By taking into account the inclination of the vortical flow structures in the near-wall area, Piomelli [65] introduced a streamwise displacement, Δs, to connect the wall shear stress to an instantaneous velocity.

$$\tau_{w,x}(x,z) = \langle \tau_w \rangle \frac{\tilde{u}(x+\Delta s, y_1, z)}{\langle \tilde{u}(x, y_1, z) \rangle_{xz}}$$
$$\Delta s = y_1 \cot 8^\circ \quad (30 < y^+ < 50), \quad \Delta s = y_1 \cot 13^\circ \quad (y^+ > 50) \tag{2.13}$$

More physics is included in this model, which produces better channel flow outcomes at $\mathrm{Re}_\tau = 2000 \sim 5000$ [66]. In addition, Piomelli [65] offered an ejection model (2.14) that takes into account the effect of near-wall structures, where C is a dimensionless constant. Marusic [33] improved expression (2.15) by set α_τ to 0.1 (for a zero-pressure-gradient flow), to refer to both the mean and local velocity components.

$$\tau_{w,x}(x,z) = \langle \tau_w \rangle - C u_\tau \langle \tilde{v}(x+\Delta s, y_1, z) \rangle_{xz} \tag{2.14}$$

$$\tau_{w,x}(x,z) = \langle \tau_w \rangle - \alpha_\tau u_\tau \left[\tilde{u}(x+\Delta s, y_1, z) - \langle \tilde{u}(x, y_1, z) \rangle_{xz} \right] \tag{2.15}$$

Werner & Wengle [67][68] provides an explicit/analytical wall shear stress model that delivers the stress as a function of both wall distance and filtered velocity from the LES field by

using a power law in place of the log law. Unlike the implicit methods discussed above, no iterative process is required. The model assumed velocity profiles

$$u^+ = \begin{cases} y^+, & y^+ \le y_m^+ \\ A\left(y^+\right)^B, & y^+ > y_m^+ \end{cases} \tag{2.16}$$

where $A = 8.3$, $B = 1/7$, and the wall shear stress is given by

$$|\tau_w| = \begin{cases} \dfrac{2\rho\nu|\tilde{u}|}{\Delta y}, & if \quad |\tilde{u}| \le \dfrac{\nu}{2\Delta y} A^{\frac{2}{1-B}} \\ \rho\left\{\dfrac{1-B}{2} A^{\frac{1+B}{1-B}} \left(\dfrac{\nu}{\Delta y}\right)^{1+B} + \dfrac{1+B}{A}\left(\dfrac{\nu}{\Delta y}\right)^{B} |\tilde{u}|\right\}^{\frac{2}{1+B}}, & if \quad |\tilde{u}| > \dfrac{\nu}{2\Delta y} A^{\frac{2}{1-B}} \end{cases} \tag{2.17}$$

Kawai and Larsson [69] modeled the unresolved inner layer by solving

$$\frac{d}{dy}\left[\left(\mu + \mu_{t,wm}\right)\frac{dU_{\|}}{dy}\right] = 0 \tag{2.18}$$

In an overlapping layer between $y = 0$ and $y = h_{wm}$, the h_{wm} represents a boundary layer thickness, the wall-model eddy viscosity is taken from the mixing length

$$\mu_{t,wm} = \kappa\rho y\sqrt{\frac{\tau_w}{\rho}} D, \qquad D = \left[1 - \exp\left(-y^+/A^+\right)\right]^2 \tag{2.19}$$

Various equilibrium models work well in specific situations; Mason's model [70], for example, takes the roughness of walls into account, Wu and Squires [71] adapted the model to a curved wall geometry, Moeng [72] gave buoyancy adjustment, etc.

Although non-equilibrium factors were considered, boundary layers do not have a universal self-similar profile [73] because the near-wall length scales are not independent of a pressure gradient. According to Mellor [74], a pressure-viscosity velocity was defined as

$$u_p = \left(\frac{\nu}{\rho} \frac{dp}{dx} \right)^{1/3} \tag{2.20}$$

which is comparable to the friction velocity u_τ under a pressure gradient flow. Afzal [75] offered a velocity profile related to friction velocity, pressure gradient, and Reynolds number. This profile is also known as Afzal's law in expression (2.21)

$$u^+ = \frac{1}{\kappa} \ln\left(y^+\right) + C - \frac{2}{\kappa} \ln\left(\frac{\sqrt{1 + p^+ y^+} + 1}{2} \right) + \frac{2}{\kappa} \left(\sqrt{1 + p^+ y^+} - 1 \right) \tag{2.21}$$

where the pressure gradient parameter $p^+ = \frac{\nu}{\rho u_\tau^3} \frac{dp}{dx} = \left(\frac{u_p}{u_\tau} \right)^3$. The aforementioned model performed better in adverse pressure gradient scenarios than the log-law [76], and it produced comparable results to a dynamic wall model [77]. However, it is not valid at a point of separation or reattachment where u_τ vanishes (2.20). Manhart et al. [78] proposed a wall model in the viscous sub-layer under a pressure gradient, that integrates both u_τ and u_p on a scale $u_{\tau p} = \sqrt{u_\tau^2 + u_p^2}$ that will not vanish. Duprat et al. [57] expanded the above model beyond the viscous sub-layer.

Based on studies of the TBLE type wall model, Park, and Moin [49] reported that the wall-model eddy viscosity should be reduced from its standard RANS value. According to Cabot and Moin [47], this viscosity should only take into consideration the unresolved part of the Reynolds stress since the resolved portion carried by the nonlinear advection terms is not negligible. Wang and Moin [79] decreased this value $\mu_{t,wm}$ by dynamically matching the total turbulent stress (resolved + modeled) of the wall model to be equal to that of the LES at the matching location by effectively lowering the value of κ in (2.19) across the wall-model layer. This attempt has proved effective in low-to-moderate Reynolds numbers flows, but it does not work well at high Reynolds

numbers because $\mu_{t,wm}$ is too low, according to Kawai and Larsson's [48] research on flat-plate boundary layer and shock/boundary-layer interaction flows.

Park and Moin [49] suggested a dynamic eddy viscosity model that needs $\mu_{t,wm}$ to be satisfied

$$2\mu_{t,wm}\bar{S}_{ij}^{d} - \frac{2}{3}\bar{\rho}k\delta_{ij} - \bar{\rho}\bar{R}_{ij} \approx 2\mu_{t}^{*}\bar{S}_{ij}^{d} - \frac{2}{3}\bar{\rho}k^{*}\delta_{ij} \tag{2.22}$$

where superscript * denotes the quantities modeled in (2.19) with the standard value of model coefficients ($\kappa = 0.41$ and $\mathrm{Pr}_t = 0.9$). In this equation, the total Reynolds stress (resolved + modeled) in the non-equilibrium mode is determined using the traditional RANS-type model, instead of merely considering the unresolved stress.

Recent efforts to create an algebraic wall-stress model have found it difficult to develop one that is simple enough to not need embedding near-wall layers. Similar efforts to enhance the so-called RANS wall function have been attempted. For example, Craft et al. [80] developed an algebraic wall function, AWF, which analytically integrated the simplified TBLE into a wall-adjacent control volume for the wall shear stress and other parameters. Since the convection and pressure gradient factors are taken into consideration and this method may be expanded to handle complicated turbulent flow fields [81], this method is characterized as a non-equilibrium model. Similar efforts have been made to build an "algebraic" non-equilibrium wall stress model for LES, such as the SGS-AWF [82], in which the SGS eddy viscosity profile within a cell next to a wall is described as two-segment piecewise linear fluctuations, allowing analytically integration of the TBLE and obtaining the wall shear stress.

In General, algebraic approaches are accessible, affordable, and simple to use. Although traditional models for non-gradient flat walls were created, non-equilibrium and adverse pressure gradients adapted methods have recently undergone advancements [82][83].

2.2.2 Hybrid RANS/LES methods

Hybrid RANS/LES techniques [17][2] allow near-wall RANS simulation to couple with the LES in the majority of the outer flow. The computational domain is divided into two subdomains with a specific interface between them. The LES subdomain takes up the majority, whereas the RANS occupies the inner layer of the turbulent boundary layer. The main concept of a hybrid is that RANS is substantially less expensive close to the wall since the resolution of a grid in wall parallel directions has less significance than that of the wall-normal resolution. To properly resolve a turbulent boundary layer is to mesh a nice gradual decrease of the wall-normal extent of the cell towards a wall. As a result, the RANS runs on the refined near-wall grid that is only along the wall-normal direction after the LES uses a big (coarse) grid to determine the thickness of a boundary layer δ.

A Detached Eddy Simulation (DES) [84] was used for the channel flow and obtained a fairly accurate result [6]. In Nikitin's approach [6], the model evaluates local wall distance with filter size to decide whether the LES Subgrid-Scale (SGS) viscosity [85] or RANS turbulent viscosity (S-A model [86]) is used. The Reynolds dependency of computation cost becomes logarithmic as a result of this simulation. However, it has a significant disadvantage in that switching from RANS to LES mode inside attached boundary layers is completely related to the grid. After a near-wall grid refinement, the turbulent length scale from the RANS model can be bigger than the grid length scale, resulting in a "grid-induced separation" and reduced turbulent

viscosity. Menter et al. [87] proposed a blending function to shield the boundary layer. Spalart et al. [7] alternated the DES length scale to include a flow-dependent shielding function that preserves the RANS length scale in the attached boundary layer area regardless of local grid refinement, resulting in the so-called Delayed Detached Eddy Simulation (DDES). Travin et al. [88] provided additional functions to avoid early separation in the DDES. Shur et al. [8] further developed Improved Delayed Detached Simulation (IDDES) to ensure that wall-modeled LES is activated only when the inflow circumstances include resolved turbulent content and the grid is fine enough to resolve the greatest energy-containing boundary layer eddies.

Zonal

Other hybrid approaches include zonal, which computes a portion of the domain using RANS while solving the remainder using LES. Davidson et al. [3] introduced this "zonal" hybrid technique by coupling RANS in $0 < y^+ \leq 60$ with a $k-\omega$ turbulence model with a one-equation k_{sgs} model in the outer LES. The matching plane of this hybrid approach was chosen by the authors to be a pre-selected grid plane inside the log area. Similar hybrid approaches with distinct turbulence models were also developed by Baurle et al [89], Schluter et al [90], and Temmerman et al [4], and this hybrid concept made significant development in 2005.

Since RANS lacks turbulent fluctuations, treating the interface is crucial for zonal approaches. To address this issue, consider damping the modeled stresses [91], adding backscatter [92], and numerical smoothing [93].

Another issue is the "Log-Layer Mismatch" (LLM), which is caused by a matching plane and results in erroneous changes in the mean velocity profile in the near-wall RANS area when

coupling to the LES solution [94]. According to [95], the modeled wall-shear stress might differ from the actual one by approximately 15%. Efforts are being made to overcome this LLM, such as adding extra feedback forcing to yield accurate flow statistics [96] and tailoring the blending function between the RANS and LES eddy-viscosities [97].

The seamless hybrid technology means that the previously explicit specified interface is dynamically decided, allowing for a smooth transition from RANS to LES. In homogeneous flows, such a technique may be considered as an LES with a cutoff wavenumber that is constantly decreasing to zero. Fadai-Ghotbi et al. [5] created a seamless hybrid model based on transport equations for the subgrid stresses, employing the elliptic-blending method to account for the nonlocal kinematic blocking effect of the wall. Jakirlic et al. [98] introduced a general dissipation rate expression based on an analytically formulated energy spectrum to adopt both large and small eddy ranges and suppressed turbulence intensity towards the subgrid level in the region where large coherent structures exist, allowing a smooth transition from LES to RANS.

2.2.3 Other approaches

Aside from the "physics-based" approaches described above, in which governing equations are effectively averaged as RANS-like at near-wall cells, there are other approaches, such as using control-based strategies to produce a given target velocity profile for a desired wall-parallel shear stresses [10] and applying neural networks that use data-driven approaches [9].

Bae et al. [12] and Bose et al. [11] proposed a dynamic slip wall model concerning the fact that the second-order approximation of the boundary condition, $\overline{u}_i\big|_w = l_i \left.\dfrac{\partial \overline{u}_i}{\partial n}\right|_w$, degrades as the

filter size increases. The authors assumed a downstream slip length, l_i , that varied with wall-normal distance. This slip length, as well as the velocities, must be modeled. In their study, the slip boundary condition for a plane channel flow was supposed to be

$$\left\langle \bar{u}_i\big|_w \right\rangle = \left\langle l_i \frac{\partial \bar{u}_i}{\partial n}\bigg|_w \right\rangle + \left\langle v_i \right\rangle \tag{2.23}$$

Krank et al [13][99] recently published a wall model using function enrichment that allows for the resolution of the sharp boundary layer gradients present in high-Reynolds-number flows as well as the consideration of significant adverse pressure gradients and convective effects. Their approach was based on the extended finite element method, with the discrete velocity represented as a conventional polynomial component, $\bar{\mathbf{u}}_h$, and an additional enrichment component, $\tilde{\mathbf{u}}_h$.

$$\begin{aligned}
\mathbf{u}_h(\mathbf{x},t) &= \bar{\mathbf{u}}_h(\mathbf{x},t) + \tilde{\mathbf{u}}_h(\mathbf{x},t) \\
\bar{\mathbf{u}}_h(\mathbf{x},t) &= \sum_{B\in N^u} N_B^u(\mathbf{x})\bar{\mathbf{u}}_B(t) \\
\tilde{\mathbf{u}}_h(\mathbf{x},t) &= \sum_{B\in N_{enr}^u} N_B^u(\mathbf{x})\left[\psi(\mathbf{x},t) - \psi(\mathbf{x}_B,t)\right] r^h(\mathbf{x})\bar{\mathbf{u}}_B(t)
\end{aligned} \tag{2.24}$$

where N_B^u denotes shape functions and only a subset of nodes near the wall $N_{enr}^u \subset N^u$ is enriched. The variable $r^h(\mathbf{x})$ is a ramp function referred to [100], and $\psi(\mathbf{x},t)$ is an enrichment function established as an empirical single analytic function for the law-of-the-wall:

$$y^+(y,\tau_w) = \frac{\psi}{\kappa} + e^{-\kappa B}\left(e^{\psi} - 1 - \psi - \frac{\psi^2}{2!} - \frac{\psi^3}{3!} - \frac{\psi^4}{4!}\right) \tag{2.25}$$

where the definition of the wall coordinate is $y^+ = \frac{y}{\nu}\sqrt{\frac{\tau_w}{\rho}}$, $\kappa = 0.41$, $B = 5.17$, and $u^+ = \frac{\psi}{\kappa}$.

As a summary of this section, various wall models are introduced. The majority of the above models were created to replicate near-wall characteristics by either calculating averaged

wall shear stress or solving RANS-like near-wall equations. Only a few of them take into consideration near-wall fluctuation features, i.e. rolling structures cause momentum transportation. An overview of a self-sustaining mechanism and numerical simulation approaches are given in the next subsection.

2.3 Self-sustaining mechanism

Turbulence in wall-bounded flows is governed by a dynamic balance of turbulence energy production and dissipation. Kim et al. [101] believed a sequence of events that streaks lift, oscillate, and break down is the essence of turbulence production. Refer to Figure 6, in which streaks are generated by streamwise rolls that redistribute the mean shear. Mathematically, substituting a perturbed shear flow $\left[\bar{u}(y)+u'(y,z,t),v'(y,z),w'(y,z)\right]$ in the x-component of the N-S equation yields $\frac{\partial}{\partial t}u' = -v'\frac{dU}{dy}$, which confirms that u' grows in this shear flow with initial disturbance v'. On the other hand, streaks and rolls decay viscously. Therefore, there must be a mechanism to compensate for dissipation and sustain the balance of turbulence energy. Such a mechanism to maintain a turbulent flow in the near-wall region is named a self-sustaining mechanism.

Understanding this self-sustaining mechanism in wall-bounded turbulence is one of the fundamental problems. Hwang and Bengana [102] used over-damped LES to simulate the interaction of isolated eddies. Their numerical results numerically confirmed the streak-roll interaction inside the self-sustaining process, which was concluded as (a) the streak is significantly amplified by the streamwise vortical structures via the lift-up effect; (b) the amplified streak,

subsequently, experiences rapid meandering motion along the streamwise direction, and (c) the meandering streaks breakdown with the regeneration of new streamwise vortical structures.

Different approaches have been applied to investigate this mechanism, including stability analysis, DNS data interrogation, and model studies. Since the 1990s, numerous models were suggesting simulating this self-sustaining mechanism.

2.3.1 Existing approaches

Waleffe proposed the self-sustaining process (SSP) model [19], in which the streamwise rolls generate streaks and can be reenergized from the non-linear feedback of the inflectional instability in the spanwise velocity of streaks. Refer to the next section for a detailed review. This model was derived based on Couette flow but shared the same principle with other wall-bounded cases. Duriez [26] experimentally demonstrated the SSP that Waleffe proposed in a flat-plate case. The work used vortex generators to create rolls and presented the existence of a mechanism above certain Re, based on the growth of the energy of streaks and spanwise velocity perturbations.

Schoppa and Hussain [22] presented an alternated mechanism for the generation of rolls from linear streak transient growth (STG). Compared to the non-linear feedback from instability, the STG mechanism is more energetic and operates more frequently for numerous, weaker, normal-mode-stable streaks.

Farrell and Ioannou [23] constructed an approach, named as roll/streak growth process (RGP), in which streaks produce Reynolds stresses that coherently force the associated streamwise rolls. The stochastic structural stability theory (SSST) was applied to reveal a robust interaction

between the streamwise roll and streak structures. Equations of the SSST system for the streamwise roll and streak dynamics:

$$\frac{d\mathbf{C}_k}{dt} = \mathbf{A}_k(\mathbf{U})\mathbf{C}_k + \mathbf{C}_k\mathbf{A}_k^T(\mathbf{U}) + f_k^2\mathbf{Q}_k \tag{2.26}$$

$$\frac{d\mathbf{\Gamma}}{dt} = \mathbf{G}(\mathbf{\Gamma}) + \sum_k \mathrm{Re}(\mathbf{L}_{RS}\mathbf{C}_k) \tag{2.27}$$

Here (2.26) is the time-dependent Lyapunov equation. The operator on velocities $\mathbf{U}$ is written as a matrix $\mathbf{A}_k$ and $\mathbf{C}_k$ represents perturbation covariance, $\mathbf{C}_k = \left\langle \hat{\boldsymbol{\phi}}_k \hat{\boldsymbol{\phi}}_k^T \right\rangle$, where $\hat{\boldsymbol{\phi}}_k = \begin{pmatrix} \hat{v}_k \\ \hat{\eta}_k \end{pmatrix}$, with Fourier expansion of the perturbation fields (vertical velocity and vorticity) in x: $v = \sum_k \hat{v}_k(y,z,t)e^{ikx}$, $\eta = \sum_k \hat{\eta}_k(y,z,t)e^{ikx}$. The last term, $f_k^2\mathbf{Q}_k$, represents the stochastic forcing that consists of an amplitude scalar and a covariance of matrix determined from the spatial correlation of the forcing. The equation (2.27) includes $\mathbf{\Gamma} = \begin{pmatrix} \mathbf{U} \\ \mathbf{\Psi} \end{pmatrix}$ that represents the momentum of mean flow where $\mathbf{\Psi}$ is a stream function. Refer to [23] for detailed expressions of other matrices.

For the self-sustaining state $f = 0$, the SSST dynamics reduce to a nonlinear interaction between the first Lyapunov vector for each k and the streamwise-averaged flow, governed by

$$\begin{aligned} \frac{d\hat{\boldsymbol{\phi}}_k}{dt} &= \mathbf{A}_k(\mathbf{U})\hat{\boldsymbol{\phi}}_k \\ \mathbf{C}_k &= \hat{\boldsymbol{\phi}}_k\hat{\boldsymbol{\phi}}_k^T \\ \frac{d\mathbf{\Gamma}}{dt} &= \mathbf{G}(\mathbf{\Gamma}) + \sum_k \mathrm{Re}(\mathbf{L}_{RS}\mathbf{C}_k) \end{aligned} \tag{2.28}$$

Further study reveals that the instantaneous growth rate of perturbation energy can be partitioned into contributions from orthogonal growing and decaying subspaces determined from

eigenvalues of the Hermitian matrix $\mathbf{D} = \mathbf{A}_k + \mathbf{A}_k^T$. A neutral perturbation state is obtained by maintaining an equilibrium of time-averaged projections in both growing and decaying directions. In conclusion in this state, the streak grows by organizing the perturbation Reynolds stress to drive its associated streamwise roll while the perturbations are sustained by the parametric growth mechanism associated with the time dependence of the streak.

All the above approaches shared the consensus that streaks are maintained by streamwise rolls through the lift-up mechanism [24] and that streamwise rolls move low-speed fluid away from the wall and reduce relative streamwise velocity to generate spanwise fluctuation which forms streaks. However, the restricted nonlinear (RNL) approach [25], in another way, constructed a two-way interaction between the mean flow and the perturbation. This model was derived directly from the N-S equations, adopts the SSST, and retains only the streamwise mean-perturbation nonlinearities to achieve computational tractability. The RNL model is written as a system of (2.29)-(2.31)

$$\mathbf{U}_t + \mathbf{U}\cdot\nabla\mathbf{U} + \nabla P - \frac{1}{R}\Delta\mathbf{U} = -\left\langle \mathbf{u}'\cdot\nabla\mathbf{u}' \right\rangle \tag{2.29}$$

$$\mathbf{u}'_t + \mathbf{U}\cdot\nabla\mathbf{u}' + \mathbf{u}'\cdot\nabla\mathbf{U} + \nabla p - \frac{1}{R}\Delta\mathbf{u}' = \mathbf{e} \tag{2.30}$$

$$\nabla\cdot\mathbf{U} = 0, \qquad \nabla\cdot\mathbf{u}' = 0 \tag{2.31}$$

The equation (2.29) describes that the dynamics of a streamwise mean flow are driven by the divergence of streamwise averaged Reynolds stresses. Meanwhile, the equation (2.30) accounts for the interaction between streamwise perturbations and the mean flow. This interaction can be further linearized to yield $\mathbf{u}'_t = \mathbf{A}(\mathbf{U})\mathbf{u}' + \mathbf{e}$, where $\mathbf{e}$ represents a stochastic excitation. Comparisons between the results from both RNL and DNS demonstrated a good agreement in the

mean velocity fields and the time-averaged central component of the Reynolds stress. Also, the feedback from the mean flow to the perturbations that produce streaks was similar to those observed in the DNS results.

In this report, the SSP model is selected due to consideration of (1) efficiency, the SSP is governed by a set of low order ordinary differential equations (ODE); (2) reasonability, the phenomenon has been experimentally demonstrated in [26]; and (3) innovation, the SSP model was derived by projecting the N-S equations on an appropriate set of orthogonal modes. The following section provides a detailed review of this model.

2.3.2 Details of the SSP model

The model was proposed by Waleffe [19][103][21], based on an assumption that streamwise rolls generate streaks, and the span-wise inflectional instability of streaks with the determined amplitude of neutral modes contributes to the feedback of rolls. Therefore, the model simplified the self-sustaining mechanism to the cycle that "steady rolls lead to steady streaks that lead to a neutral mode that feedbacks steady rolls" [19]. In this model, the rolls are assumed as a key component in the entire domain to produce streaks, even though in certain situations [32][31] the streaks do exist in the physical flow without rolls.

Waleffe described the lowest-order truncation for the x-independent flow, $\mathbf{u}(y,z,t)=\begin{bmatrix} u(y,z,t) \\ v(y,z,t) \\ w(y,z,t) \end{bmatrix}$, which consists of 3 components written in (2.32)

$$\begin{bmatrix} u(y,z,t) \\ v(y,z,t) \\ w(y,z,t) \end{bmatrix} = M(t)\begin{bmatrix} \sin(\beta y) \\ 0 \\ 0 \end{bmatrix} + U(t)\begin{bmatrix} \cos(\gamma z) \\ 0 \\ 0 \end{bmatrix} + V(t)\begin{bmatrix} 0 \\ \gamma\cos(\beta y)\cos(\gamma z) \\ \beta\sin(\beta y)\sin(\gamma z) \end{bmatrix} \tag{2.32}$$

where amplitudes of mean shear, streaks, and rolls are denoted as M , U , and V as functions of time. The streaks without truncation are $u(y,z) = \sum_{n=0}^{\infty} U_n(y)\cos(n\gamma z)$, which is induced by rolls $\begin{bmatrix} v(y,z) \\ w(y,z) \end{bmatrix} = \begin{bmatrix} \gamma\cos(\beta y)\cos(\gamma z) \\ \beta\sin(\beta y)\sin(\gamma z) \end{bmatrix}$ that satisfy the continuity. Here variables β and γ are wave numbers. The lowest-order truncation for the streak instability mode (x-dependent velocity perturbations in v and w components) consists of an additional 5 components (see equation (9) in [19]).

The author substituted velocities ((2.32) and equation (9) in [19]) in the N-S equation (2.33) which is driven in the x-direction by $F(y) = F\sin(\beta y)$, then, projected onto 8 modes (Galerkin projection)

$$\left(\frac{\partial}{\partial t} + \frac{1}{R}\nabla^2\right)\mathbf{u} = -\mathbf{u}\cdot\nabla\mathbf{u} - \nabla p + F(y)\hat{\mathbf{x}} \tag{2.33}$$

By further reduction of the instability mode, the final low-order system is simplified as

$$\begin{aligned}
\left(\frac{d}{dt} + \frac{\kappa_m^2}{\mathrm{R}}\right)M &= \frac{\kappa_m^2}{\mathrm{R}} + \sigma_m W^2 - \sigma_u UV \\
\left(\frac{d}{dt} + \frac{\kappa_u^2}{\mathrm{R}}\right)U &= \sigma_u MV - \sigma_w W^2 \\
\left(\frac{d}{dt} + \frac{\kappa_v^2}{\mathrm{R}}\right)V &= \sigma_v W^2 \\
\left(\frac{d}{dt} + \frac{\kappa_w^2}{\mathrm{R}}\right)W &= \sigma_w UW - \sigma_m MW - \sigma_v VW
\end{aligned} \tag{2.34}$$

where the amplitude of instability is $W(t)$, R is a Reynolds number, κ and σ are model coefficients defined by wave numbers, refer to [19] for details.

In the above system (2.34), the mean shear, M, is designed to be in the range $0 < M \leq 1$ for stability reasons, and its magnitude is maintained by both the forcing term $\frac{\kappa_m^2}{\mathrm{R}}$ and the feedback of instability, W. The system can be sustained only when $V > 0$ and $UV > 0$ since the streaks get energy transferred from the mean via the term $\sigma_u MV$ and $-\sigma_u UV$. Finally, the instability gives rise to W via the $\sigma_w UW$ term and sustains the rolls throughout the $\sigma_v W^2$ term.

Chapter 3 Rolls and wall shear stress

This chapter establishes two statistical relationships: (1) magnitude relations of rolls and fluctuating wall shear stress, and (2) correlation of rolls and local gradient of total pressure under various grid resolution conditions. They contribute to the later wall modeling to control the amplitude and frequency of fluctuating wall shear stress. Both relationships are fitted from rolling samples that I extracted by using a bounding box search process throughout The DNS channel flow field data [104]. Additionally, the formation of a near-wall rolling structure was traced to show how rolls affect fluctuating wall shear stress.

Fluctuation characteristics are influenced by rolling effects, which can be smoothed out on a coarse grid. To capture this effect regardless of mesh resolution, a connection between core vorticities and fluctuation magnitudes has been established through data analysis. Further investigation has revealed a correlation between core vorticity and gradients of total pressure, which might be interpreted as an indication of the presence of a local rolling structure.

3.1 Wall shear stress and Filtering effects

This section begins by presenting and comparing the performance of fluctuating wall shear stress under different filtering meshes. Then, established that a reasonably fine near-wall mesh in both wall-normal and parallel directions is essential to resolve streaks and wall shear stress. The subsequent section provides more observations on how a single rolling structure impacts fluctuations.

The DNS field data utilized in this thesis was downloaded from the Johns Hopkins Turbulence Database [104], which contains information on a fully developed turbulent channel flow at $\mathrm{Re}_\tau = 1,000$. Specifying a near-wall rectangular region, filling it with a structural fine mesh, $\Delta x_i^+ = 2$ or $\Delta x_i = 0.002$, and getting velocities from the database at each mesh point. The wall shear stress is calculated from the velocities mentioned above using the formula (3.1)

$$\tau_w = \nu \left. \frac{du_{//}}{dy} \right|_w \approx \nu \frac{\Delta u_{//}}{\Delta y} = \nu \frac{\left(u_{j=1}\right)_{//} - u_w}{y_{j=1} - 0} \tag{3.1}$$

where $u_{//}$ is the velocity component in a wall parallel projection. The derivative $\frac{du_{//}}{dy}$ at a wall is approximated by using a first-order bias finite difference approximation. The subscription $j = 1$ denotes values at the first grid point off the wall. According to the non-slip condition, $u_w = 0$. This finite difference should be accurate in the linear inner boundary layer ($d^+ = 8$).

In Figure 7, the left plot (resolution 2x2) displays distributions of wall shear stress in magnitude from the DNS data, whereas the right plot is a filtered result. The expression of such a filtering process is written as

$$\tilde{\phi}(x,z) = \int_{-\infty}^{+\infty} \int_{-\infty}^{+\infty} \phi(x,z) G(x,x') G(z,z') dx' dz', \quad G(x,x') = \begin{cases} 1/\Delta, & |x - x'| \le \Delta \\ 0, & otherwise \end{cases} \tag{3.2}$$

The above 2D box filter is applied repeatedly to existing wall shear stress, beginning with the DNS one (Figure 7 left), to build a succession of filtered distributions at various resolutions (e.g. 4x4, 8x8, …, 128x128). For clarity, Figure 7 only shows the distribution at 64x64 resolution.

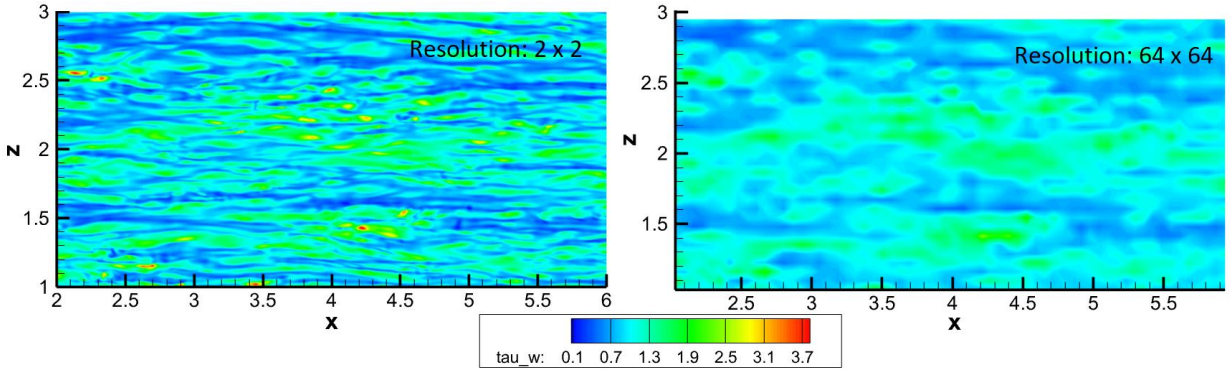

Figure 7: (Left) Distribution of wall shear stress from the lower surface of the DNS channel flow [104], @ t=10.0s; (Right) Filtered result with a mesh of 64x64 in plus units

Figure 7 shows two distributions with the same contour scale. The lower-resolution one lacks some streak details.

The fluctuation characteristics change, see the PDF of wall shear stress as shown in Figure 8 (Left). Fine resolution curves show a skewed (non-symmetric) distribution about neither the mean nor its peak, with the largest potential wall shear stress value being less than the mean (gray dash). However, filtering shifts the highest probability value to the mean and reshapes the profile to become symmetric. The right plot in Figure 8 depicts the changes in maximum, minimum, and mean values resulting from such filtering. Both the maximum and minimum values converge to the mean, and the mean value remains constant.

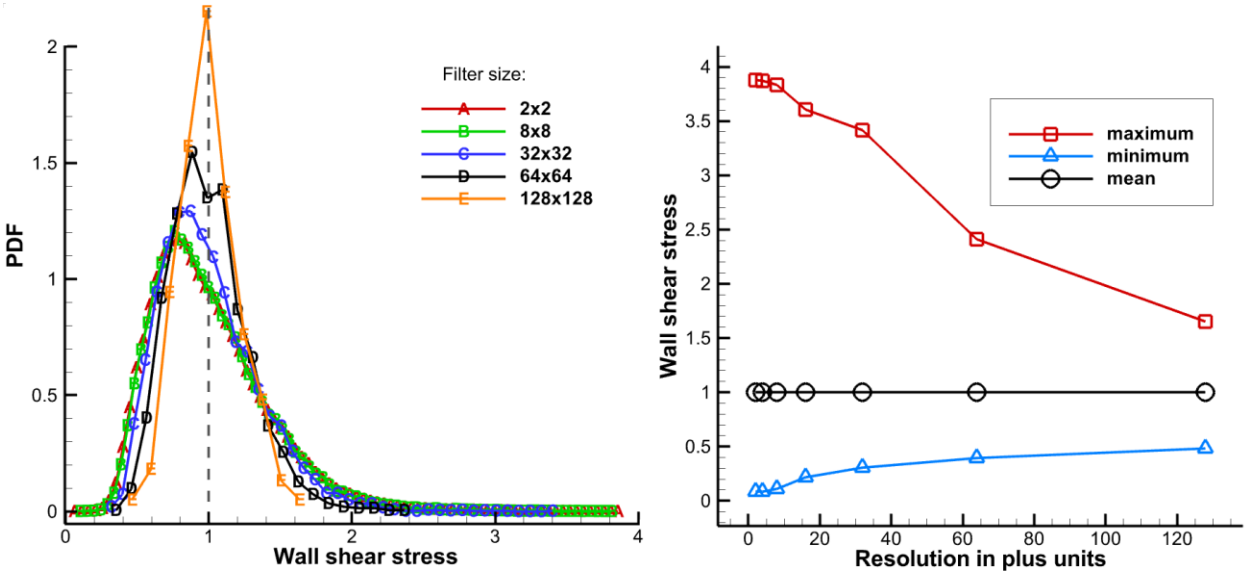

Figure 8: (left) PDF of wall shear stresses from different filtering sizes; (right) mean and extreme value changes along resolution.

To summarize, applying a 2D filter in the wall-parallel directions alters the shape of the PDF and the extreme values of wall shear stress, but it does not affect the mean value. In contrast, filtering velocities in all dimensions results in a compromised approximation of the mean wall shear stress. This is because the finite difference approximation $\frac{\Delta u_{//}}{\Delta y}$ underestimates the derivative in such a large wall normal distance condition. As shown in Figure 9, the mean value of the black curve decreases as resolution decreases (larger grid spacing). Meanwhile, the PDF's form narrows and sharpens, and its central position shifts towards the bottom left.

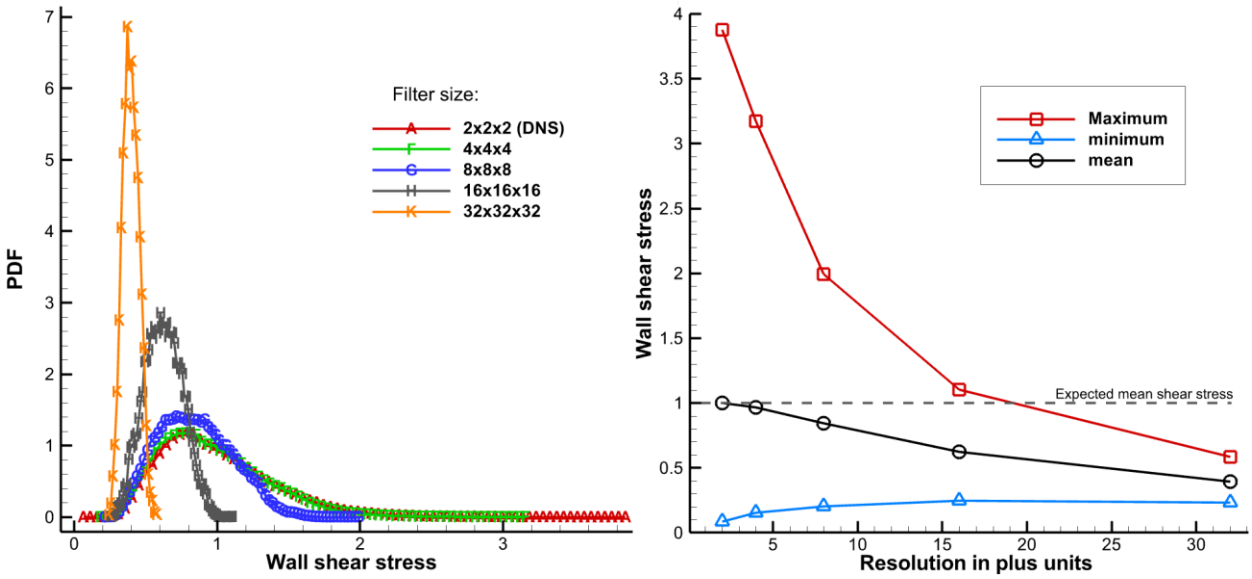

Figure 9: (left) PDF of wall shear stresses from different filtering sizes; (right) mean and extreme value changes along resolution.

To summarize the previous studies, filtering in the wall-normal direction underpredicts the mean value of wall shear stress. this inaccuracy can be as much as 50% if the filter size is greater than 16, due to finite difference approximation. On the other hand, wall parallel-direction filtering does not affect the mean, but it reduces the magnitude of wall shear stress perturbations and redistributes the PDF to make it more symmetrical in its mean value.

Further exploration is conducted to examine near-wall vertical rolling structures as a direct cause of fluctuating wall shear stress.

3.2 Near-wall rolling structures

In this section, rolling structures from the DNS near-wall field will be studied to provide statistical recommendations for the proposed wall model. The observation of an individual rolling

structure is provided initially for an intuitive summary. Following this finding, changes in rolling structural variables are traced to uncover possible relationships. Second, a significant amount of information retrieved from diverse rolling structures that were extracted from a DNS field confirms the relationships of rolls to fluctuations and rolls to total pressure gradients. These relations are used to construct the wall model in the next chapter. Finally, a brief overview of a method for extracting data and executing the aforementioned analysis is provided.

3.2.1 Overview of a single rolling structure

This example rolling structure is downloaded from a DNS channel flow (, raw field data from the Johns Hopkins Turbulence Database [104]). It is located within the coordinate range of $-0.6 \le x \le -0.2$, $-1 \le y \le -0.8$, $-0.26 \le z \le -0.14$, and has a lifespan summarized in several time frames: $t = 9.8s,\ 9.9s,\ \cdots, 10.7s$.

Vortical structures, such as streamwise rolls, are usually generated near the wall. Rolling structure strength increases as it moves downstream until it is lifted far away from the wall. These rolls assist in the exchange of lower low-speed fluid for higher (away from a wall) high-speed fluid, causing a fluctuation in wall shear stress. Figure 10 shows a typical roll lifetime as well as wall shear stresses. The flow of data from the DNS channel [104]. Both vorticity iso-contours (black spatial iso-surfaces) and wall shear stresses are displayed. A roll is formed near a wall by perturbations (fragments of the previous vortex) according to the time frames “9.8s” and “9.9s”. Then, its core vorticity increases as its internal second layer of iso-surface appears and the difference in wall shear stress becomes more apparent in the period “10.0s”. The rolling structure’s length and the area of generated wall shear continue to grow until the frame “10.1s”. Finally, the

vorticity and generated disturbance of the rolling structure diminish as it is gradually raised away from the wall.

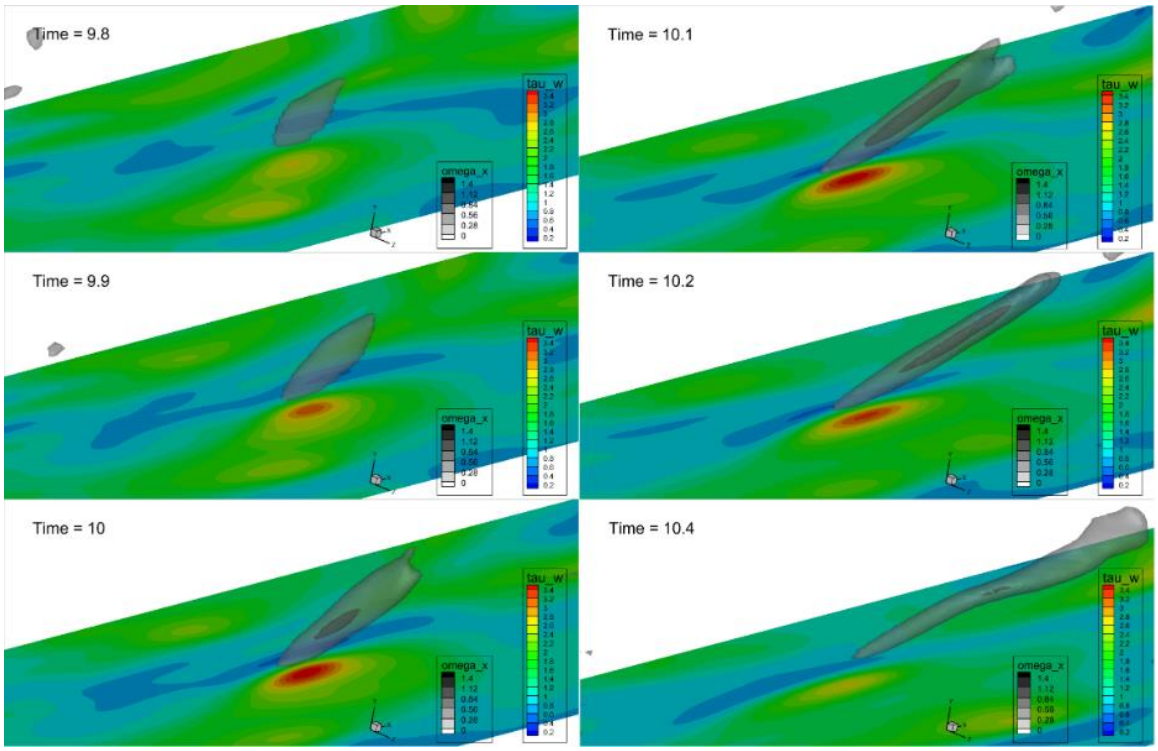

Figure 10: Development of a rolling structure, in the above-mentioned DNS [104] velocity field

Figure 11 displays a detailed view of a single frame at “Time=10”. The left plot illustrates a roll and its resulting fluctuating wall shear stress. The right two figures show the total pressure distribution and the derivative of total pressure wrt. the spanwise ‘z’ on the vertical cutting plane, corresponding to the left plot. The roll coincides with the maximum derivative of total pressure, according to velocity vectors.

Figure 12 presents a similar view at the time frame of “10.4s”, where the roll is observed to be diminishing. As the rolling structure travels upward, regions with high total pressure

derivatives move away from the wall, resulting in a more uniform and smoother distribution of total pressure across the spanwise direction, as seen in Figure 11.

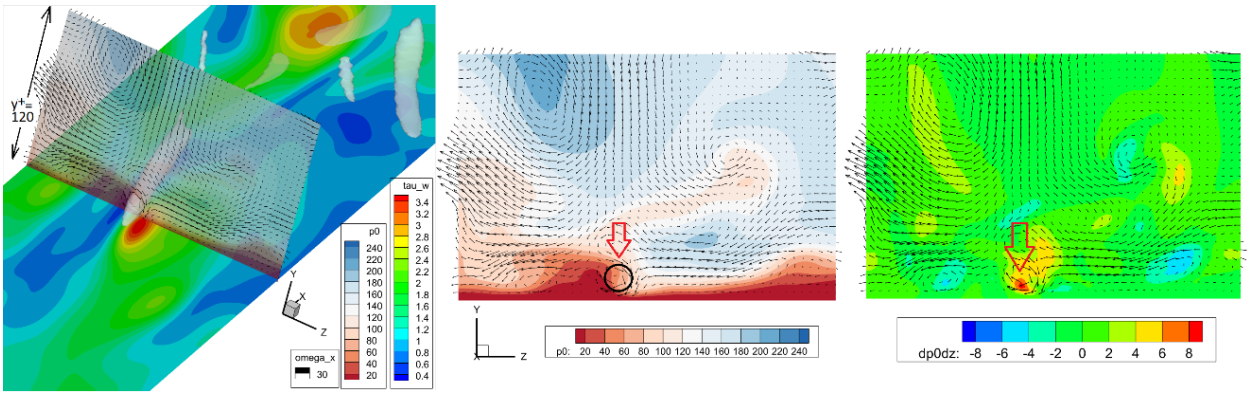

Figure 11: (left) Rolls and induced perturbation of total wall shear stress on the left, total pressure, and a derivative of total pressure wrt. z on the vertical cutting plane on the center and right. Time frame 10.0s, rendered from the above-mentioned DNS field, from [104]

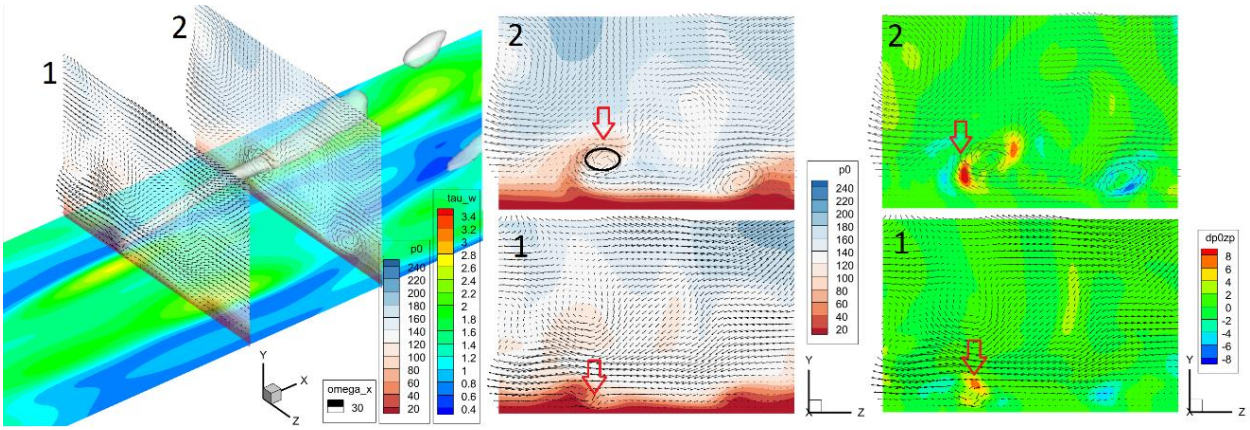

Figure 12: Weakening rolls and produced perturbations in comparison to Figure 11, Time frame= 10.4s, rendered from the above-mentioned DNS [104] field

The qualitative comparison between Figure 10 and Figure 12 above illustrates changes in stress fluctuation under rolling structures. Furthermore, the following variables will be used to statistically assess the relationships between rolls and fluctuation amplitudes:

- The highest magnitude of core vorticity, denoted by $|\Omega_{\max}|$, is extracted from a local rolling structure to quantify its strength, with the absolute value operator used to eliminate the roll direction. The distance from the core vorticity location to the nearest wall is represented by d_{Ω}.
- The magnitude of the fluctuating wall shear stress, denoted by Δ_{shear}, is assessed as the difference between the maximum and minimum wall shear stress beneath the rolling structure.
- The directional derivatives of the local total pressure are monitored, but only the maximum value wrt. 'z' spanwise component, demoted as $\max\left(\left|\frac{dp_0}{dz}\right|\right)$, or p_{0z} for simplicity, is measured. It has a wall distance of $d_{p_0 z}$.

I manually extract the above variables' values from Figure 10 frames and show their changes during a typical rolling structure lifespan, as shown in Figure 13. The blue curve in Figure 13's left plot exhibits a constant peak value of $\frac{dp_0}{dz}$ accompanied by a roll, and both wall distances are typically increasing. Additionally, both values of $|\Omega_{\max}|$ and Δ_{shear} are seen to respond similarly to changes in the strength of the rolling structure.

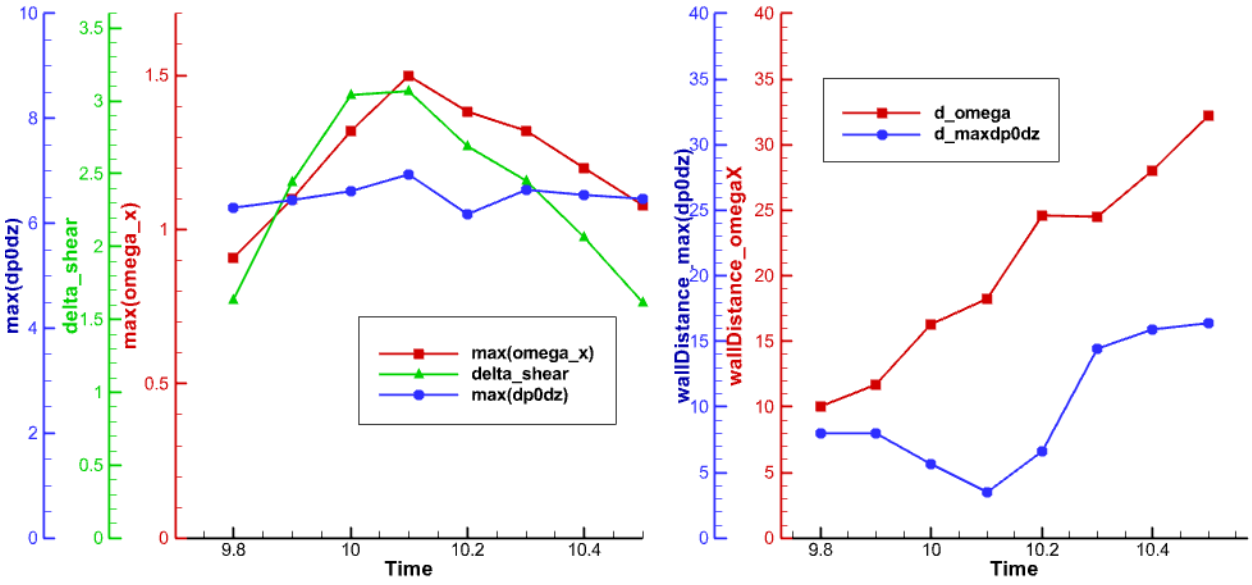

Figure 13: Tracing variable value changes across a normal roll's lifespan

As a result of the above observations:

1. Δ_{shear} is proportional to $|\Omega_{\max}|$;
2. The occurrence of a rolling structure is accompanied by an extreme value of the spanwise derivative of total pressure, and both the wall distances of the rolling structure and the extreme value are increasing.

3.2.2 Data Analysis of rolling structures

This subsection establishes two statistical relationships that will be used for wall modeling in the next chapter. These relationships are derived from 10,173 samples of vortical structures taken from the field data of the DNS channel flow [104] via a bounding box approach. The first one relates the magnitude of core vorticities and induced fluctuating wall shear stress. The second

one correlates the core vorticities between mesh resolution and gradients of total pressure. Details of the bounding box approach are followed at the end.

A wider range of DNS channel flow data downloaded from [104] has been used for analysis in this subsection. The range is within $2 \le x \le 6$, $-1 \le y \le -0.8$, $1 \le z \le 3$, and the time frames cover $t = 8.7s, \ \cdots, 15.4s$.

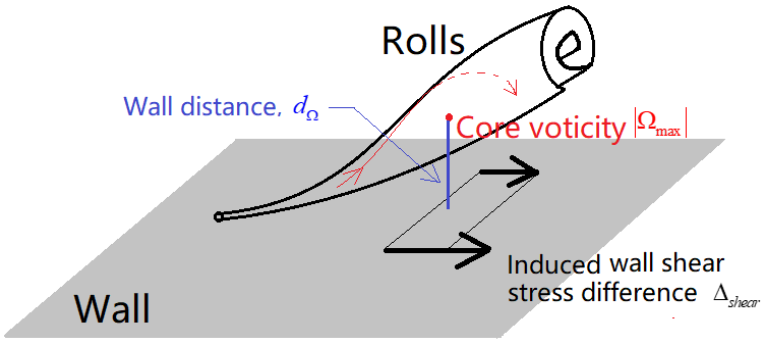

Figure 14: A sketch of the near-wall rolling structure and several variables

Typical near-wall rolls and associated variables are sketched in Figure 14. Figure 15 displays pairs of $|\Omega_{max}| - \Delta_{shear}$ from the sampled vortical structures mentioned earlier and Expression (3.3) is derived by fitting such data points in Figure 15.

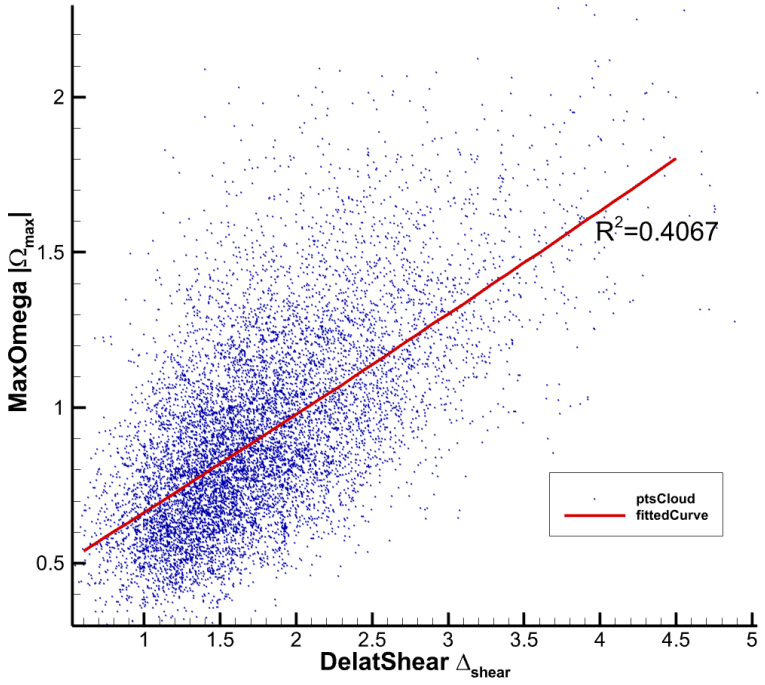

Figure 15: Curve fitting by using pairs of $\Delta_{shear} - |\Omega_{\max}|$ from 10,173 samples of vertical structures

(1) The proportional relationship between Δ_{shear} and $|\Omega_{\max}|$

$$|\Omega_{\max}| = 0.004035\Delta_{shear}^2 + 0.3034\Delta_{shear} + 0.3551 \tag{3.3}$$

This fitting has a coefficient of determination, or R^2, value 0.4067, evaluated by $\frac{\sum_{i=1}^{n}(\hat{y}_i - \bar{y})^2}{\sum_{i=1}^{n}(y_i - \bar{y})^2}$, where y_i, $\hat{y}_i$, and $\bar{y}$ represent data, predictor from fitting, and average values, respectively. Generally, this coefficient indicates the goodness of fitting. In this fitting model, 40.67% of the variation in the $|\Omega_{\max}|$ values is accounted for by the Δ_{shear} values. However, without understanding the physics of data, the resulting coefficient is meaningless.

irregular and chaotic motions of flow characterization in turbulent flow leads to fluctuations in variables. These fluctuations can significantly affect the behavior of rolling structures, making it difficult to analyze using conventional regression models. To mitigate the impact of these fluctuations, averaging techniques can be used. In my study, I grouped pairs of data based on the wall distance of core vorticity (in plus units), d_{Ω}, and calculated the average performance within each group to obtain a representative measure of the rolling structure. Figure 16 illustrates two sample groups of core vorticity wall distance in layers: $0 < d_{\Omega} \leq 10$ and $40 < d_{\Omega} \leq 50$. Although the sample dots in each group are widely spread, it is highly likely that lower rolling structures show stronger core vorticity and can induce greater fluctuations in wall shear stress.

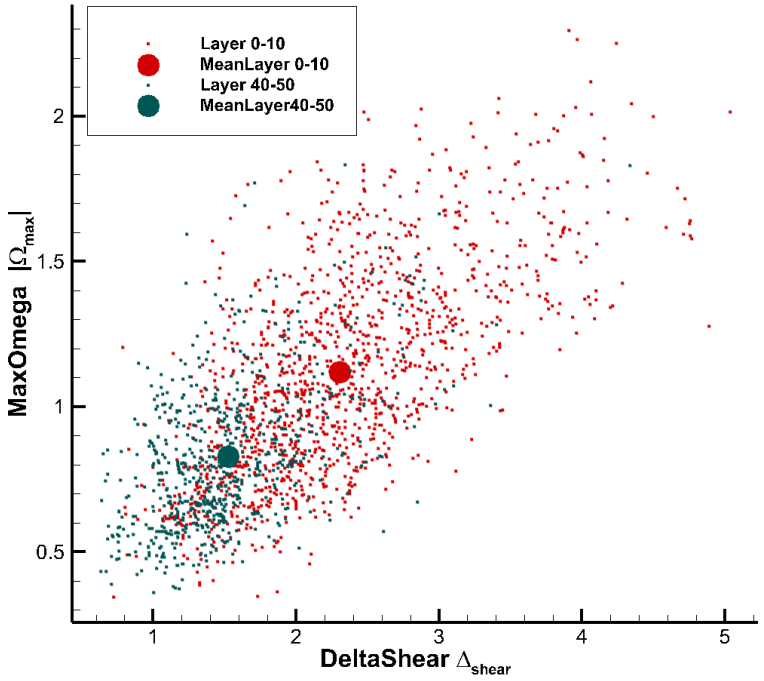

Figure 16: Groups of sample points based on core vorticity wall distance: $0 < d_{\Omega} \leq 10$ in red, and $40 < d_{\Omega} \leq 50$ in dark green. Averaged performance in bold dots

Figure 17 provides PDFs and averaged performance of each group in both Δ_{shear} and $|\Omega_{\max}|$. These profiles confirm that (1) with the increasing wall distance of core vorticity, its magnitude and the influence on wall shear stress are decreasing; (2) the high probability performance of rolling structures agrees with mean values in each group.

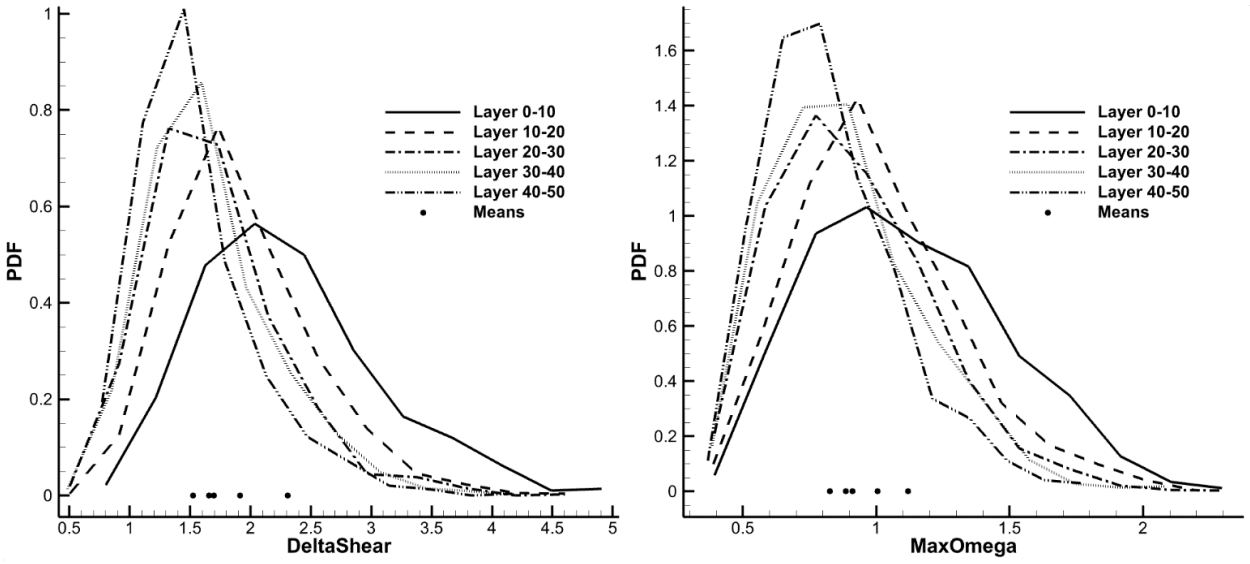

Figure 17: PDFs of Δ_{shear} and $|\Omega_{\max}|$ for each group based on wall distance of core vorticity

Therefore, redrawing Figure 15 to include averaged performance dots from each group gives Figure 18. These averaged dots are well-present rolling structures that have been smoothed to remove turbulent oscillations, and they exhibit a higher coefficient of determination value compared to blue dots, ($R^2 = 0.7975$). Finally, both the polyline and fitted curve show that a stronger rolling structure with higher core vorticity leads to larger fluctuations in wall shear stresses. This statistical result is valid at least within a range of $5^+ < d_\Omega \leq 50^+$.

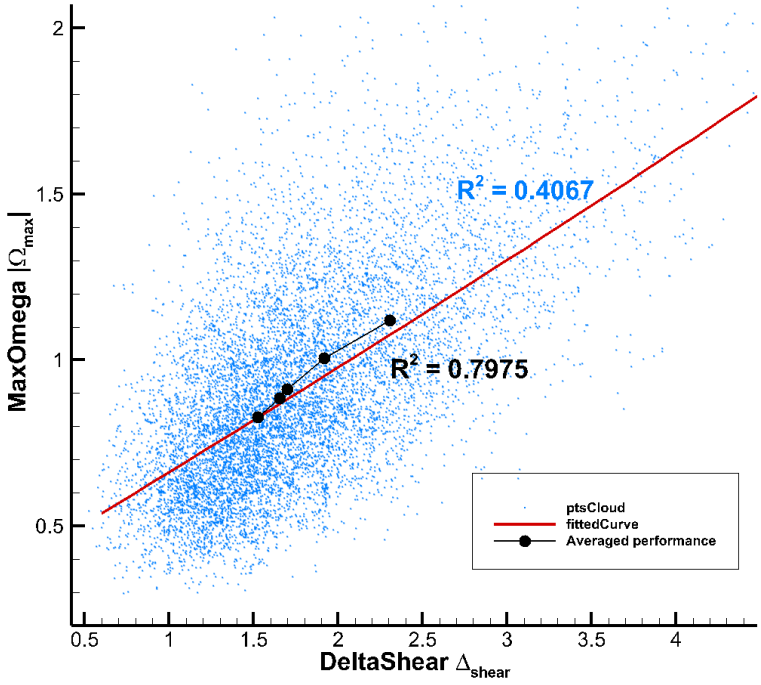

Figure 18: Averaged performance of rolling structures (in black dots) with the fitted curve from samples

(2) The extreme $\frac{dp_0}{dz}$ coincides with the rolling structures

Similarly, expression (3.4) concludes the relationship between $|\Omega_{\max}|$ and $\max\left(\left|\frac{dp_0}{dz}\right|\right)$, or $|\Omega_{\max}| - p_{0z}$

$$p_{0z} = -1.058\Omega_{\max}^2 + 6.041\Omega_{\max} + 2.647 \tag{3.4}$$

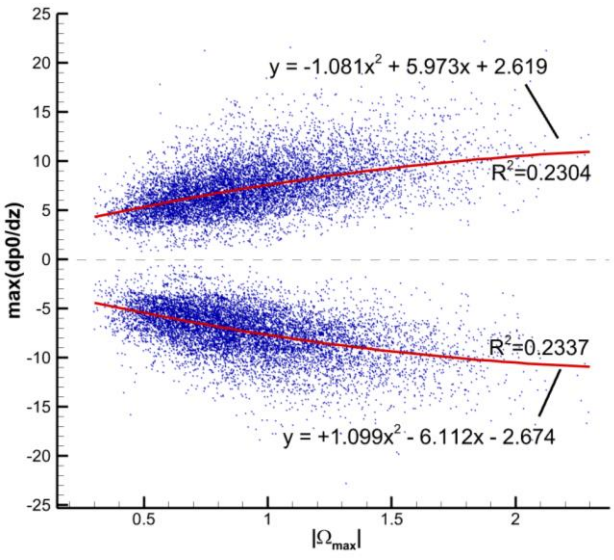

Figure 19: data of $|\Omega_{\max}| - \max(dp_0/dz)$

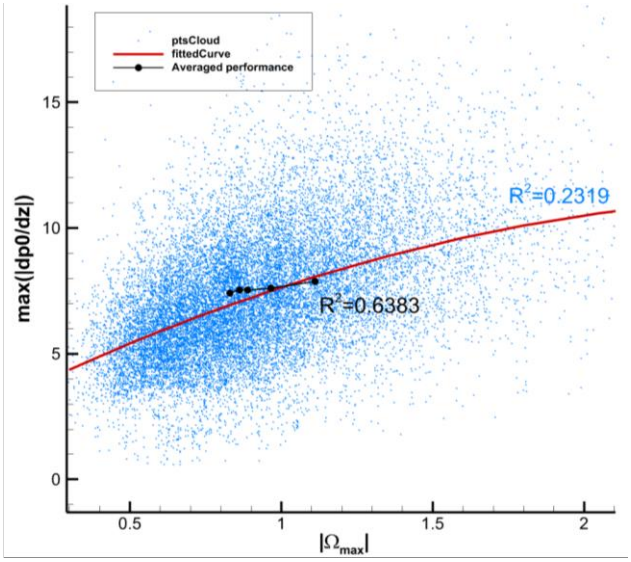

Figure 20: data of $|\Omega_{\max}| - |\max(dp_0/dz)|$

In Figure 20, the fitted solid red curve is accompanied by black dots from grouped averaging of blue samples that have flipped all negative $\frac{dp_0}{dz}$ points from Figure 19, which shows two opposed sets of original $\frac{dp_0}{dz}$ that are almost symmetric about the horizontal axis.

(3) A brief of the bounding box searching procedure

This section provides a brief of this technique to analyze the DNS data, including the extraction of rolling structures from DNS field data, parameters selection, and subsequent validation steps. For simplicity, there are limited 15 sequential time frames from $t = 10.0s$ to

$t = 10.5s$ within a small range of $0 \le x \le 2$, $-1 \le x \le -0.8$, and $0 \le x \le 1$, but it is enough to calibrate the bounding box procedure for extracting valid sample rolls.

The primary task behind bounding box searching is to locate the peak of vorticity and subsequently establish a correlation with the nearest fluctuating variables, such as wall shear stress or total pressure gradient, to determine whether it qualifies as a potential sample of a vortical structure. Assuming that the near-wall region is characterized by a dense forest of rolling structures, with each roll ongoing close to the wall and showing a core vorticity that follows an increasing-then-decreasing pattern, it is expected that there would be lots of local maxima of vorticity. To capture as much of such local maxima vorticity, a global search needs to be performed in as many subranges of its solution domain.

To effectively capture numerous local vorticity maxima, a global search should be conducted across multiple subranges of the field. However, later on, the physical distance between the core vorticity and another fluctuating variable, such as the maximum wall shear stress on a wall, imposes a limitation on how small this subrange can be. Therefore, picking the right size for the bounding box can be quite challenging. If the box is too small, it may generate false sample pairs that fail to accurately capture the rolling-induced features. Conversely, if the box is too large, it may miss relevant samples or, even worse, capture pairs not belonging to a single roll but rather span across multiple rolling structures.

This thesis tried different sizes of bounding boxes in numerical tests. Figure 21 collects outcome pairs of $\Delta_{shear} - |\Omega_{\max}|$. The subtitle of each figure indicates box sizes in Δx^+ and Δz^+ directions, to save computational cost, boxes have a constant height $\Delta y^+ = 200$ across the wall. In

Figure 21, the result from the top left corner shows that 3,575 pairs were detected, with the majority of them crowded in the lower left corner of the coordinates. This clustering could be attributed to small bounding boxes that captured numerous growing rolls with weak vorticity and minor influence from fluctuating wall shear stress. Therefore, the curve fitting based on these pairs resulted in a lower coefficient of dominance. On the other hand, using larger bounding boxes led to significantly fewer samples. These samples contained high-fidelity pairs, resulting in the highest coefficient of dominance for the fitted curve. However, the larger boxes overwhelmed small internal rolls, leading to samples that only represented large rolling features. This can adversely impact the accuracy of the fitted curve.

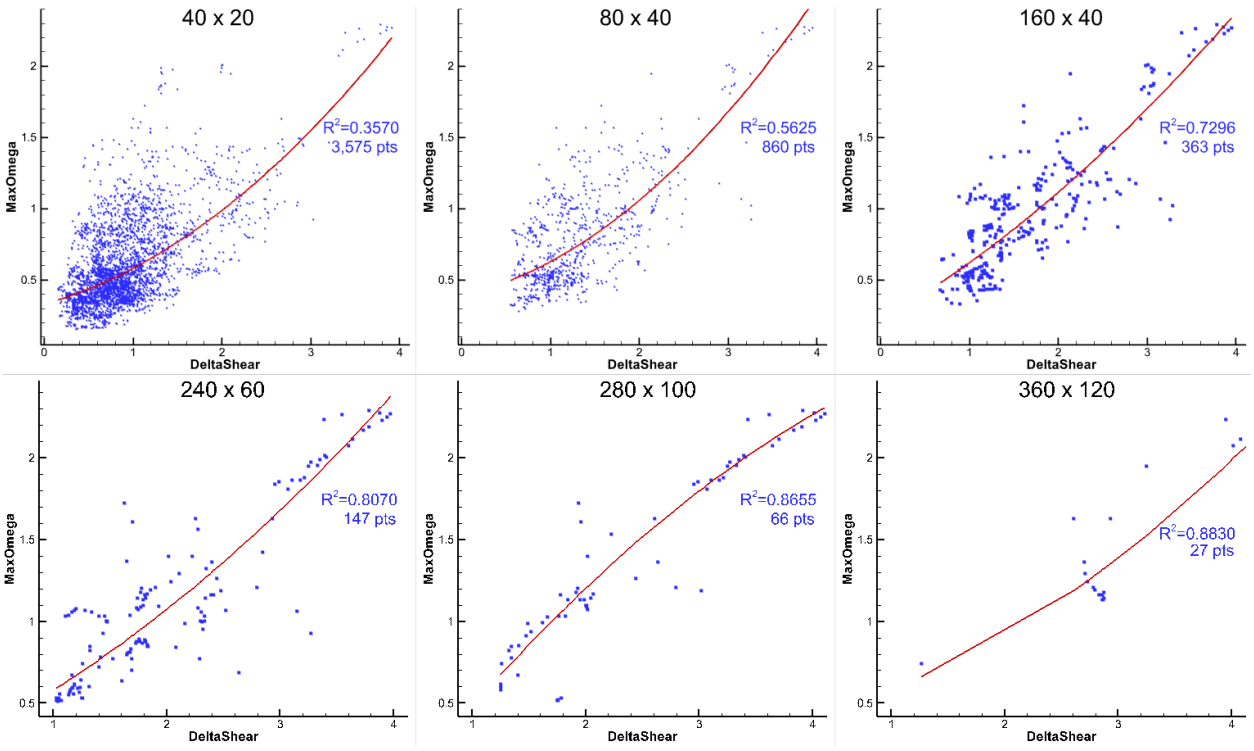

Figure 21: Search results by using variable sizes of bounding boxes

Upon overlaying six fitted curves onto a single plot, Figure 22 is obtained. Notably, the curves corresponding to box sizes 160x40 and 240x60 exhibit close alignment, indicating that varying box sizes within this range have minimal impact on the fitting outcome. Considering that the former box size (160x40) extracts a larger number of samples, which is beneficial for subsequent layer averaging, this thesis chose to utilize the bounding box with dimensions of 160x40.

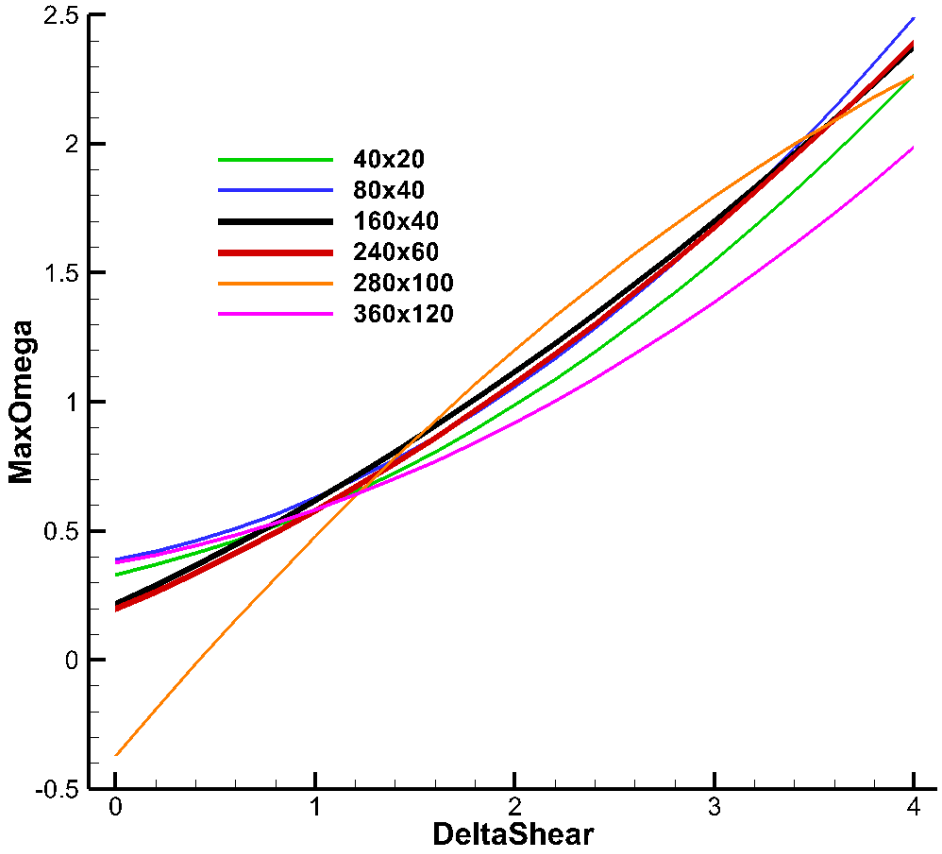

Figure 22: Comparison of fitted curves from different sizes of search boxes

3.3 Mesh size effects

This section investigates grid resolution impacts on the above relationship of $|\Omega_{\max}|$ and $\max(dp_0/dz)$, or denoted as $p_{0,z}$, and observes changes $p_{0,z}$ as a function of $|\Omega_{\max}|$, and mesh size, d. The DNS field data has a mesh resolution of 2x2x2, and this solution will be filtered step by step to generate solutions on meshes of 4x4x4, 8x8x8, …, 64x64x64. Finally, the relationship from $p_{0,z}$ to $|\Omega_{\max}|$ and d will be used to determine whether allocating fluctuations by considering local grid resolution and core vorticity. Figure 23 provides point clouds and fitted curves in various colors that indicate the results from different meshes. Despite the decrease in determination values on coarser resolutions, the fitted curves still show a similar direction of slope and trends of movement. Further considering turbulence effects and the fact that the (blue) DNS curve passes through its point cloud to symmetrically split points into both sides, the other curves exhibit this similar feature. This indicates that the fitted curves are reasonable.

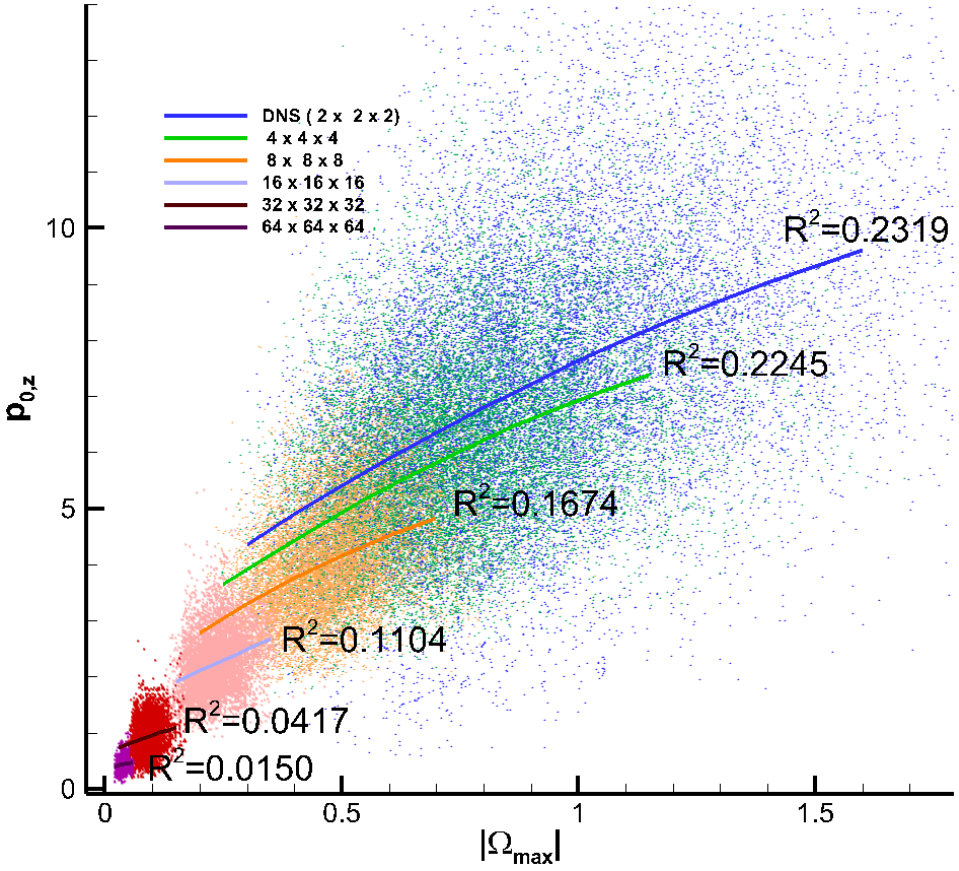

Figure 23: $|\Omega_{max}| - p_{0,z}$ relations under different resolution grid sets

Table 1 lists expressions for such curves in up to second-order polynomial form.

Resolutions	Fitted curves
2 x 2 x 2	$p_{0,z} = -1.058\|\Omega_{max}\|^2 + 6.041\|\Omega_{max}\| + 2.647$
4 x 4 x 4	$p_{0,z} = -1.552\|\Omega_{max}\|^2 + 6.326\|\Omega_{max}\| + 2.16$
8 x 8 x 8	$p_{0,z} = -2.49\|\Omega_{max}\|^2 + 6.325\|\Omega_{max}\| + 1.627$

16 x 16 x 16	$p_{0,z} = -0.8586\left\|\Omega_{\max}\right\|^2 + 3.368\left\|\Omega_{\max}\right\| + 1.398$
32 x 32	$p_{0,z} = -3.557\left\|\Omega_{\max}\right\|^2 + 3.632\left\|\Omega_{\max}\right\| + 0.6344$
64 x 64	$p_{0,z} = 1.95\left\|\Omega_{\max}\right\| + 0.3601$

Table 1: formulas for fitted curves under different mesh resolutions

When grid resolution, represented by a cell height, d, is introduced, the z-directional component of the gradient of total pressure becomes a function of two parameters, $\left|\Omega_{\max}\right|$ and d. The previous curves create a surface $p_{0,z}\left(\left|\Omega_{\max}\right|, d\right)$, as seen in Figure 24's left plotting. A further uniform of $\left|\Omega_{\max}\right|$ provides $p_{0,z}\left(\Omega, d\right)$, and its expression refers to the surface on the right of Figure 24, and its expression corresponds to the surface on the right of Figure 24.

$$p_{0,z}\left(\left|\Omega_{\max}\right|, d\right) = 2.497 + 6.771\cdot\left|\Omega_{\max}\right| - 0.07342\cdot d - 1.163\cdot\left|\Omega_{\max}\right|^2 - 0.2039\cdot\left|\Omega_{\max}\right|\cdot d + 0.0007084\cdot d^2 \quad (3.5)$$

$$p_{0,z}\left(\Omega, d\right) = 5.225 + 4.103\cdot\Omega - 0.2872\cdot d - 0.638\cdot\Omega^2 - 0.06696\cdot\Omega\cdot d + 0.003424\cdot d^2 \quad (3.6)$$

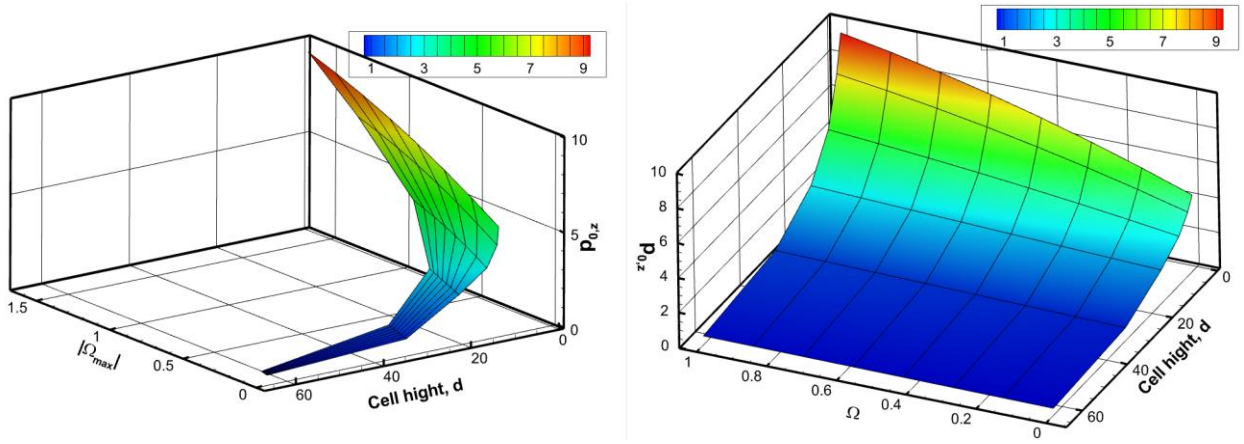

Figure 24: the statistical surface of $p_{0,z}\left(|\Omega_{\max}|, d\right)$ and $p_{0,z}\left(\Omega, d\right)$, providing a threshold value of the gradient of total pressure, above which fluctuating wall shear stresses have been applied.

3.4 Summary

This chapter focused on the near-wall rolls and the associated fluctuating wall shear stress. Based on a typical rolling lifespan observation, a variable relationship was presented between rolling core vorticity and the magnitudes of wall shear stress fluctuations. This relationship was fitted using cloud points, where each point represents a roll and fluctuating pair extracted from the DNS fields. Similarly, a curve was fitted for core vorticity against the gradient of total pressure. To make this curve more useful in the case of a coarse mesh, the grid size was added as a second dimension/parameter, enabling the extension of the curve to a surface.

In addition, this chapter presented a demonstration of how the amplitude and probability density function (PDF) of the fluctuating wall shear stress varies with filtering/grid size. The effects of changing grid sizes in the spanwise and wall-normal directions were also discussed. In

summary, the wall-parallel resolution primarily affects fluctuation characteristics, while the mean value of wall shear stress in the wall-normal dimension is significantly impacted by the grid size.

To develop a more comprehensive wall model, data analysis was conducted on DNS fields to extract samples of rolling, fluctuation, and gradient information for a curve-fitting process. This process established correlations between these variables, which will aid in the construction of the wall model.

Chapter 4 Formulation

The magnitude of wall shear stress can be decomposed into averaging and fluctuating components

$$\tau_w = \overline{\tau}_w + \tau'_w \tag{4.1}$$

This chapter focuses on modeling the latter fluctuating one. The primary aim is to present the idea of rolls as a cause of fluctuations and to establish a model for them. The following chapter begins by evaluating rolling magnitudes of rolls using LES field flow information and the SSP procedure. It then discusses the translation of the roll amplitude to the magnitude of fluctuating wall shear stress, which will be incorporated into the LES boundary conditions. This chapter provides a comprehensive overview of each step involved in this process, which is discussed in more detail in the subsequent sections.

4.1 Simulation amplitude of near-wall rolls

In general, resolving vortices in near-wall flows is challenging due to the difficulty in meeting both the minimum requirements of mesh points (3 to 5 points) and moderate aspect ratios (<5) in each dimension. This is especially true for coarse meshed practical near-wall flows, where it's not feasible to strictly enforce these conditions. To address this challenge, this section proposes a cost-effective technique that evaluates local rolls in wall-neighboring cells. This approach is less sensitive to the aspect ratio stretch and offers a practical solution to resolving vortices in near-wall flows with coarse meshes.

The SSP model is utilized in each cell adjacent to a wall. Four real-value time-dependent variables, namely the amplitudes of mean shear (M), streak (U), roll (V), and instability (W), are denoted as $\mathbf{M} = \left[M, U, V, W\right]^T$. The rolling flow is described as $V \cdot \Phi_{011}$, where the mode of a roll is

$$\Phi_{011} = \begin{bmatrix} 0 \\ \gamma \cos\left(\beta y'\right) \cos\left(\gamma z'\right) \\ \beta \sin\left(\beta y'\right) \sin\left(\gamma z'\right) \end{bmatrix} \tag{4.2}$$

The coordinates y' and z' are defined in a parameter domain ranging from -1 to 1, while γ and β represent the wave numbers. The plot for these rolls is shown in Figure 25. Further details on the remaining modes can be found in expressions (8) and (9) in reference [19].

Each iteration of the LES is denoted as a superscript t at each time. The amplitude of mean shear is updated using a local ratio of velocities from the LES field, denoted by

$$M^t = \frac{\left\| v_1^t \right\|}{\left\| v_\infty^t \right\|} \tag{4.3}$$

Subscription 1 represents the near-wall value and the ∞ represents the outer reference stream flow. The amplitudes of streak, roll, and instability remain unchanged from the previous stage.

To update the variables, an explicit forward Euler approach is employed

$$\mathbf{M}^t = \mathbf{M}^{t-1} + \Delta t \left. \frac{d\mathbf{M}}{dt} \right|^{t-1} \tag{4.4}$$

The time derivative is evaluated using an explicit SSP system (4.5). The appendix of the paper [19] provides a detailed expression of the coefficients used in this system. The wavenumber is set to $\alpha = 1.155,\ \beta = \pi/2,\ \gamma = \pi$, and the parameter $R = \frac{\|v_1\| d}{\nu}$, where the wall distance $d = 2d_1$ is twice the distance from the cell center to the wall.

$$\begin{aligned}
\left(\frac{d}{dt} + \frac{\kappa_m^2}{R}\right) M &= \sigma_m W^2 - \sigma_u UV + \frac{\kappa_m^2}{R} \\
\left(\frac{d}{dt} + \frac{\kappa_u^2}{R}\right) U &= -\sigma_w W^2 + \sigma_u MV \\
\left(\frac{d}{dt} + \frac{\kappa_v^2}{R}\right) V &= \sigma_v W^2 \\
\left(\frac{d}{dt} + \frac{\kappa_w^2}{R}\right) W &= \sigma_w UW - \sigma_u MW - \sigma_v VW
\end{aligned} \tag{4.5}$$

4.2 Modeling the fluctuations

This section deals with simulating fluctuations through the use of amplitude and wave motion. The focus is on transforming roll amplitude into fluctuating wall shear stress and modeling the motion using the PDF obtained from DNS data. Three main topics are discussed. Firstly, the use of core vorticity as an indicator and its relationship with rolling strength is explored. Next, a relationship between this vorticity and fluctuating wall shear stress is established. Lastly, a methodology for spreading this fluctuation to local wall patches is presented.

4.2.1 Core vorticity

In the previously modeled rolls (4.2), the core vorticity value is obtained when $y' = 0,\ \ z' = \pm\frac{1}{2}$:

$$\Omega'_{\max} = \frac{\partial v_w}{\partial y'} - \frac{\partial v_v}{\partial z'} = V \cdot \left(\beta^2 + \gamma^2\right) \cos(\beta y') \sin(\gamma z') \tag{4.6}$$

The sign of the core vorticity depends on the direction of the roll. It can be either positive or negative. The parameter domain is further transformed to the plus units (or physical) domain, that is $y = \frac{d}{2}\left(y' - 1\right)$, resulting in

$$\Omega_{\max} = \left(\frac{2}{d}\right)^2 \Omega'_{\max} \tag{4.7}$$

Two assumptions were made in the previous evaluation: (1) rolls are described by expression (4.2), and (2) rolls are independent of the x coordinate. However, the rotation speed distribution may not necessarily be a function of the central distance as stated in (4.2), and roll shapes can be altered by local stretching and compression. To assess the difference between the model, Figure 25 shows a qualitative comparison between true DNS rolls and those generated by the model. This distinction might lead to modeling errors. Section 5.1.1 provides more details on the calibration of core vorticities using expression (4.6) and (4.7).

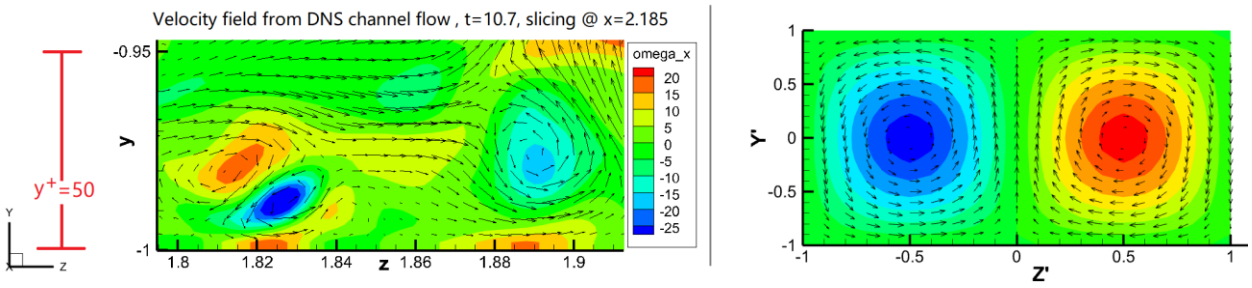

Figure 25: vertical slides depict velocity vectors and vorticity distributions for actual examples of DNS near-wall rolling structures (on the left) and modeled ones (on the right)

The use of core vorticities in describing rolls is based on their ability to indicate rolling strength and position in a reliable and easily calculated way. As shown in Figure 25, core vorticity is generally located at the center of each roll, surrounded by a gradient with a gradually decreasing magnitude. The intensity of local rolls is proportional to the levels of core vorticity.

4.2.2 The magnitude of fluctuating wall shear stress

Recall the $\Delta_{shear} - |\Omega_{\max}|$ relationship's expression (3.3). A further linearization yields

$$\Delta_{shear} = 3.293|\Omega_{\max}| - 1.170 \tag{4.8}$$

which maps core vortices to magnitudes of fluctuating wall shear stress in the plus units.

Combining (4.6)(4.7) (4.8) to get the magnitude of fluctuating wall shear stress

$$\Delta_{shear} = 3.293\left(\frac{2}{d}\right)^2 \left(\beta^2 + \gamma^2\right) \cdot V - 1.170 \tag{4.9}$$

Notes: This model only takes into account the fluctuations induced by the rolling structures.

4.2.3 Wave motion

To assign or reconstruct fluctuations induced by rolling structures, a wave motion is required after obtaining the magnitude using the method described above. However, the distribution of wall shear stress under rolling structures, as shown in Figure 10 of the DNS flow, suggests that this motion should be a complex, multi-variable function.

A brief numerical experiment on the PDF of wall shear stress caused by a single roll is presented on top of Figure 26. The experiment assumes that a roll, denoted by $V \cdot \Phi_{011}$, exists in a stream boundary layer flow described by the equation (2.3). The magnitude V is set to 3% of the free-stream velocity, and its diameter is 40 in plus units. Using the finite difference approach, the wall shear stress magnitudes in the domain are evaluated, and the resulting PDF is presented in Figure 26.

The blue curve in Figure 26 represents the PDF obtained from a numerical experiment involving only a single roll, which differs from the DNS PDF shown in the left panel of Figure 9 (red curve). However, as more rolls of varying sizes are added to the field, the resulting PDF shape more closely resembles the DNS curve. The bottom red PDF curve in Figure 26, generated using a set of rolls with diameters ranging from 30 to 60 (in increments of 10), is more realistic and reflects the growth of rolling structures in an actual flow and the consideration of a spectrum of multi-scale rolls. Thus, this experiment provides strong evidence that near-wall rolling structures are the primary factor responsible for the unique characteristics of the PDF, including (1) non-symmetry about the mean value, (2) peak and skewness to the left of the mean, and (3) the lowest shear stress value being significantly closer to the mean than the highest value.

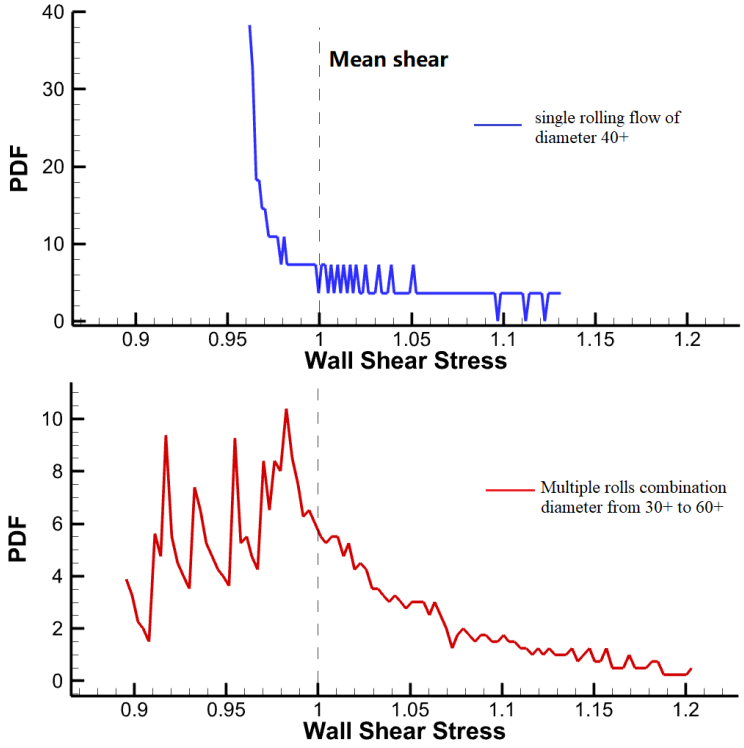

Figure 26: Comparison of PDFs resulting from a single rolling structure (top) and multiple rolls of different sizes (bottom)

This thesis further investigates statistical PDFs from the DNS flow, with a focus on extracting PDFs of wall shear stress caused by specific groupings of roll sizes. Figure 27 displays these PDFs, with the red curve representing the PDF from the original field data (all roll sizes) and the others representing the distribution of wall shear stress underneath the specified roll sizes obtained using the aforementioned boxing method. To provide more clarity, Figure 28 shows the outcomes of the PDF of each specified group of rolls that was subtracted from the original entire spectrum PDF. It reveals that larger rolls cause higher fluctuation in both the magnitude of Δ_{shear} (horizontal distance from crest to trough) and the impacted region of fluctuation (deep oscillation).

The hypothesis that near-wall rolls are the primary cause of fluctuation is supported by both statistical and numerical evidence, where the near-wall rolling velocity pattern is related to the shear stress distribution on walls. Further studies demonstrate magnitudes relationships, correlation, and alterations in PDF of wall shear stress across various sizes of rolls. Therefore, it is reasonable to use the PDF profile from the DNS to shape the distribution of wall shear stress in the proposed model.

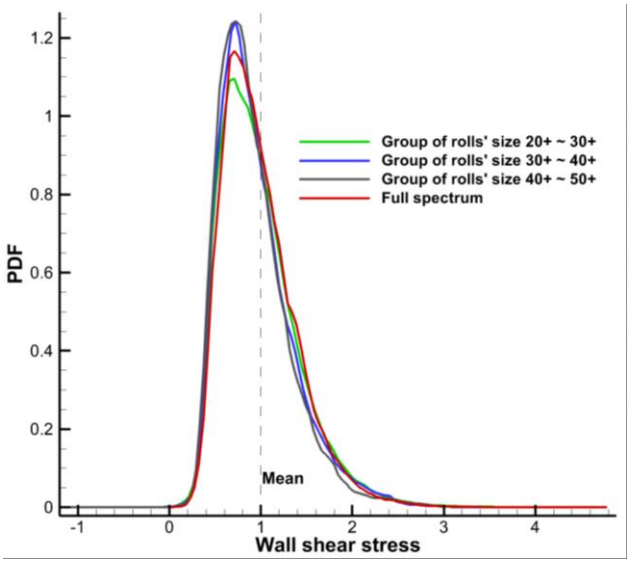

Figure 27 PDFs of specified roll sizes

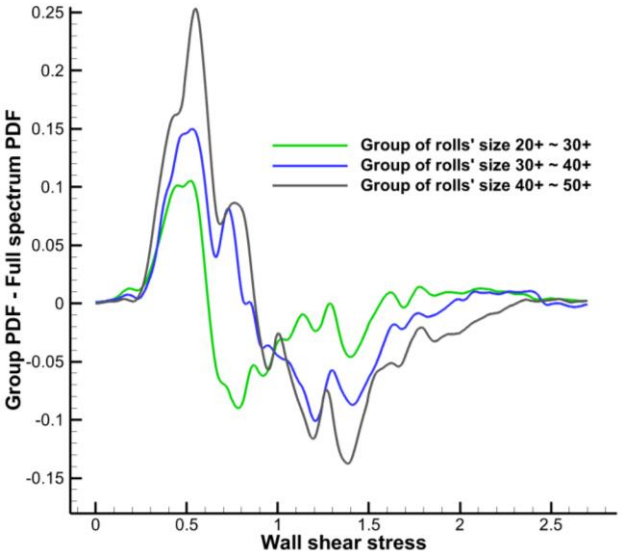

Figure 28: Subtracts each group PDF of rolls from the original entire spectrum PDF of DNS

4.2.4 The range of wall shear stress

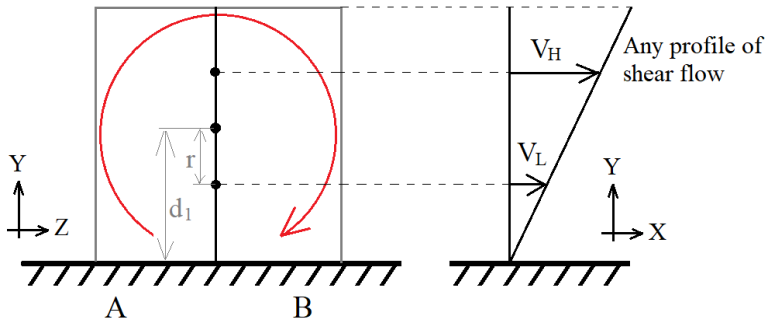

Figure 29: Sketch of a simplification of mean shear

The clockwise roll shown in Figure 29 produces an acceleration of the velocity near the wall as the roll switches high-speed flow v_H downward towards the wall at the right side B. This, in turn, speeds up the local near-wall flow and increases the streamwise component of wall shear

stress. Conversely, the wall shear stress on the left side A of the wall decreases. The wall shear stress distribution varies monotonically across the spanwise direction, ranging from the upwash side to the downwash side.

Figure 18 illustrates the relationship between statistically-averaged rolling sizes and corresponding values of Δ_{shear}, which can be used to determine an appropriate ratio $\frac{r}{d_1}$. This statistical relationship is shown in the left two columns of Table 2 and can be used to calibrate the equivalent swapping model. By enumerating r/d_1 to obtain identical results from modeled $\max(\tau_w)-\min(\tau_w)$ to the statistical Δ_{shear} for various wall distances, the final r/d_1 ratios are listed in the third column of Table 2. The black dots in Figure 30 present the calibrated points obtained during the above calibration process. The log-law profile is used to determine the value of v_1, v_L and v_H during the process.

Statistical data		Model data (4.11)			r/d_1
d_1, or d_Ω	Δ_{shear}	$\min(\tau_w)$	$\max(\tau_w)$	$\max(\tau_w)-\min(\tau_w)$	
5	2.55	0.316	2.869	2.554	0.521
15	1.96	0.229	2.189	1.960	0.613
25	1.70	0.167	1.868	1.701	0.686
35	1.60	0.128	1.734	1.606	0.741
45	1.48	0.106	1.590	1.484	0.772

Table 2: The r/d_1 values in the 6th column were calibrated by matching the modeled values of $\max(\tau_w)-\min(\tau_w)$ in the 5th, which were calculated using the model data in the 3rd and 4th columns, to the statistical Δ_{shear} values in the 2nd column

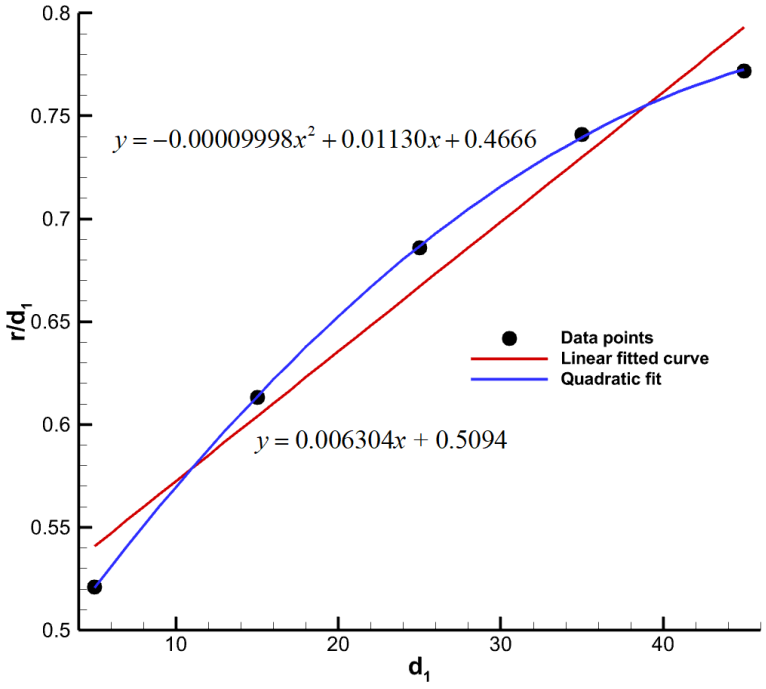

Figure 30: fitting a curve to the relationship between d_1 and $\frac{r}{d_1}$

Figure 30 shows dots representing the ratio as a function of wall distances, d_1, from the center of a wall-adjacent cell (where d_1 is equivalent to the roll radius d_Ω within the cell), and both a quadratic and linear fitting curve are plotted. The thesis will evaluate this ratio using a second-order equation

$$\frac{r}{d_1} = -0.00009998 d_1^2 + 0.0113 d_1 + 0.4666 \tag{4.10}$$

In the equation (4.11), the maximum range of fluctuation values is expressed as a function of both wall distance and the local velocity profile. However, this represents an extreme scenario where a roll with a radius r completely exchanges layers of near-wall flow. In practice, this is

unlikely to occur in its entirety but can be considered as a reference range for later shifting Δ_{shear} from the mean value.

$$\tau_w \in \left[\min(\tau_w), \max(\tau_w)\right]_{extreme} = \left[\frac{\frac{v_L}{d_1+r}}{\frac{v_1}{d_1}}\overline{\tau}_w, \ \frac{\frac{v_H}{d_1-r}}{\frac{v_1}{d_1}}\overline{\tau}_w\right] \tag{4.11}$$

To adjust for the rolling effects, an asymmetric distribution is proposed in this thesis that is proportional to (4.11), as splitting the magnitude Δ_{shear} equally around the mean value $\overline{\tau}_w$ is not appropriate. A ratio R_{tau} is defined as the value of below-averaging over above-averaging.

$$R_{tau} = \frac{\overline{\tau}_w - \min(\tau_w)}{\max(\tau_w) - \overline{\tau}_w} \tag{4.12}$$

The range of fluctuating wall shear stress will be in (4.13), based on the mean and asymmetric ratio of below- to above-averaging defined by R_{tau}

$$\left[\frac{(R_{tau}+1)\overline{\tau}_w - R_{tau}\Delta_{shear}}{R_{tau}+1}, \frac{(R_{tau}+1)\overline{\tau}_w + \Delta_{shear}}{R_{tau}+1}\right] \tag{4.13}$$

4.2.5 Assign fluctuations

The model assumes that wall shear stress increases in the direction from the upwash side to the downwash side beneath a rolling structure. As the roll is assumed to occupy a wall cell, the wall shear stress within the cell varies monotonically, either increasing or decreasing, along its spanwise direction.

This thesis proposes a method for mapping the spanwise distribution of each vertex within a wall cell onto a segment of the DNS PDF curve to obtain the corresponding wall shear stress. The red curve in Figure 27 of the DNS PDF is used as a reference. An analytical expression is derived from a third-order piecewise fitting.

$$p_{PDF}\left(\tau_w\right)=\begin{cases}10.78\tau_w^3-4.447\tau_w^2+0.5748\tau_w-0.02186 & 0.064\le\tau_w<0.304\\ 71.43\tau_w^4-156.9\tau_w^3+124.5\tau_w^2-39.22\tau_w+4.259 & 0.304\le\tau_w<0.688\\ -13.33\tau_w^3+22.97\tau_w^2-11.41\tau_w+2.421 & 0.688\le\tau_w<0.88\\ -0.5066\tau_w^4+3.397\tau_w^3-7.714\tau_w^2+6.077\tau_w-0.3057 & 0.88\le\tau_w<2.368\\ -0.004865\tau_w^3+0.05498\tau_w^2-0.2091\tau_w+0.2678 & 2.368\le\tau_w\le3.856\\ 0 & \tau_w<0.064,\ \ \tau_w>3.856\end{cases} \tag{4.14}$$

The arc length of the curve can be expressed as a function of wall shear stress, $s_{PDF}\left(\tau_w\right)$, by numerically integrating sample points from $p_{PDF}\left(\tau_w\right)$. This function is then piecewise fitted to obtain the arc length expression.

$$s_{PDF}\left(\tau_w\right)=\begin{cases}-286.37\tau_w^5+368.22\tau_w^4-160.64\tau_w^3+30.64\tau_w^2-1.566\tau_w+0.01112 & 0.064\le\tau_w<0.514\\ -8.348\tau_w^4+32.27\tau_w^3-46.01\tau_w^2+30.18\tau_w-6.247 & 0.514\le\tau_w<1.164\\ -0.04213\tau_w^4+0.4828\tau_w^3-2.0459\tau_w^2+4.803\tau_w-1.398 & 1.164\le\tau_w\le3.856\end{cases} \tag{4.15}$$

The inverse of the length function is written as

$$\tau_w\left(s_{PDF}\right)=\begin{cases}0.8098s^3-1.613s^2+1.298s+0.05694 & 0\le s<0.9157\\ -0.2846s^3+1.475s^2-1.868s+1.212 & 0.9157\le s<2.1065\\ -0.03813s^3+0.4723s^2-0.9323s+1.388 & 2.1065\le s<5.0691\end{cases} \tag{4.16}$$

Refer to Figure 31, Figure 32, and Figure 33 for the curves.

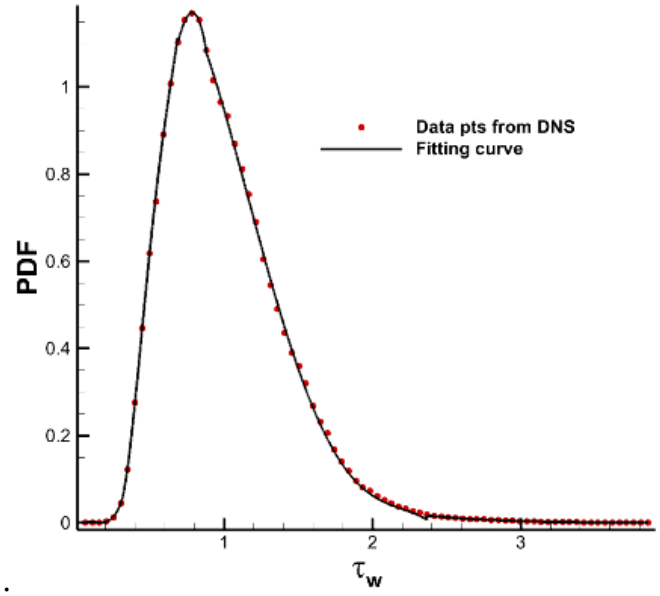

Figure 31: PDF of wall shear stress

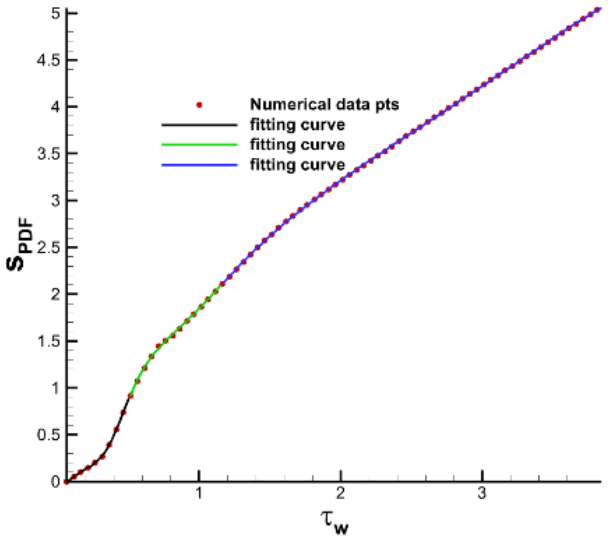

Figure 32: Arc length of the DNS PDF curve

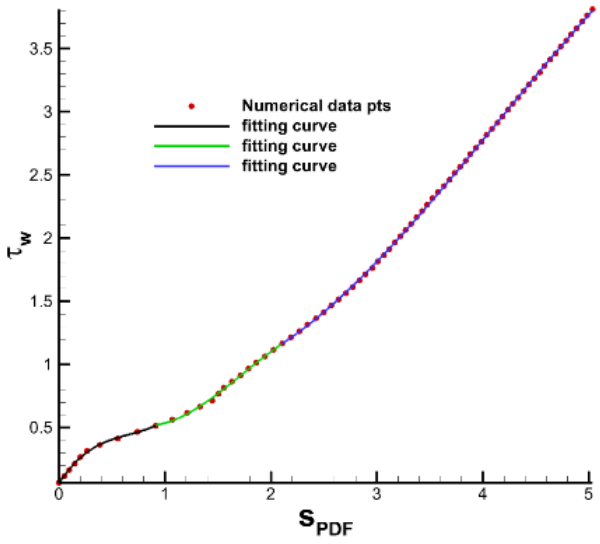

Figure 33: The inverse of arc length

Connecting all wall vertex for each cell by a sequence. This polyline will be mapped to the PDF arc curve to calculate the wall shear stress at each vertex. See Figure 34 for a polyline example.

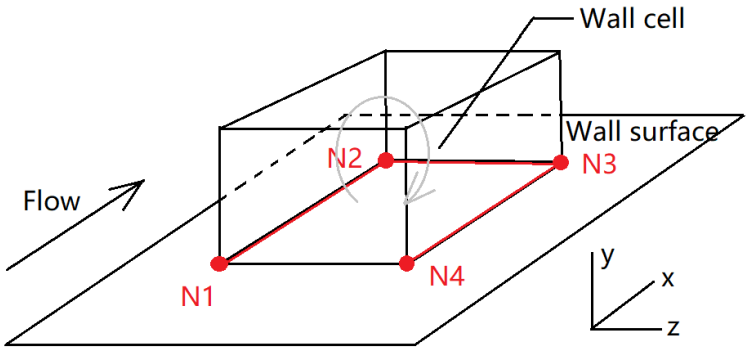

Figure 34: Sketch of a wall vertex polyline

Notes:

(1) The ordering of nodes attached to the wall is determined based on their coordinates projected onto the local spanwise direction

(2) The polyline begins from the wall-attached nodes on the upwash side to ensure that it aligns with the increase of wall shear stress along the path.

(3) This polyline is stretched and aligned to s_{PDF} through a mapping process, and the corresponding nodal values of τ_w are obtained through the inverse function $s_{PDF}^{-1}(\tau_w)$. The following algorithm outlines the process:

Step 1: Compute the local spanwise unit vector for a wall patch.

Step 2: Project all vertices onto the local spanwise vector, and sort them in ascending order. These vertices are denoted as $N_1, \cdots, N_i, \cdots, N_n$

Step 3: Connect the vertices in sequence and compute the geometric distance between each pair to obtain the path length $s_i = s_{i-1} + \left\| N_{i+1} - N_i \right\|$. Starting with $s_0 = 0$, the total path length is $s_{total} = s_n$.

Step 4: Mapping each vertex onto the segment of $s_{PDF}\left(\tau_w\right)$ between $s_{PDF}\left(\tau_w\big|_{\min}\right)$ and $s_{PDF}\left(\tau_w\big|_{\max}\right)$, refer to expression (4.13) for $\tau_w\big|_{\max}$ and $\tau_w\big|_{\min}$.

Step 5: Obtain the corresponding shear stress values by a substitute $s_{i,PDF}$ in $s_{PDF}^{-1}\left(\tau_w\right)$ to get τ_i.

In summary, the expression τ_i is written in (4.17), where $D_{PDF} = s_{PDF}\left(\tau_w\big|_{\max}\right) - s_{PDF}\left(\tau_w\big|_{\min}\right)$

$$\tau_i = \begin{cases} s_{PDF}^{-1}\left[\dfrac{\left(R_{tau}+1\right)\overline{\tau}_w - R_{tau}\Delta_{shear}}{R_{tau}+1}\right] & i = 1 \\ s_{PDF}^{-1}\left[\dfrac{\left(R_{tau}+1\right)\overline{\tau}_w - R_{tau}\Delta_{shear}}{R_{tau}+1}\right] & i = N \\ \tau_1 + \dfrac{s_i}{D_{PDF}}\left(\tau_N - \tau_1\right) & 1 < i < N \end{cases} \tag{4.17}$$

(4) To keep conservation, the above shear stresses on a vertex are shifted by their difference to the mean value. The final wall shear stress on the vertex of each wall patch is

$$\hat{\tau}_{w,i} = \tau_i - \left(\frac{\sum_{i=1\cdots N} \tau_i}{N} - \overline{\tau}_w \right) \tag{4.18}$$

4.3 Boundary conditions

4.3.1 Interactions between the LES and the wall model

This section describes the interaction between the LES and the wall model solution. Figure 35 provides an example where the LES occupies the entire computational domain, including the wall, while the wall model solves for wall shear stress in its wall cell using the current field solution. The wall model then feeds the computed wall shear stress back to the LES solver as a boundary condition.

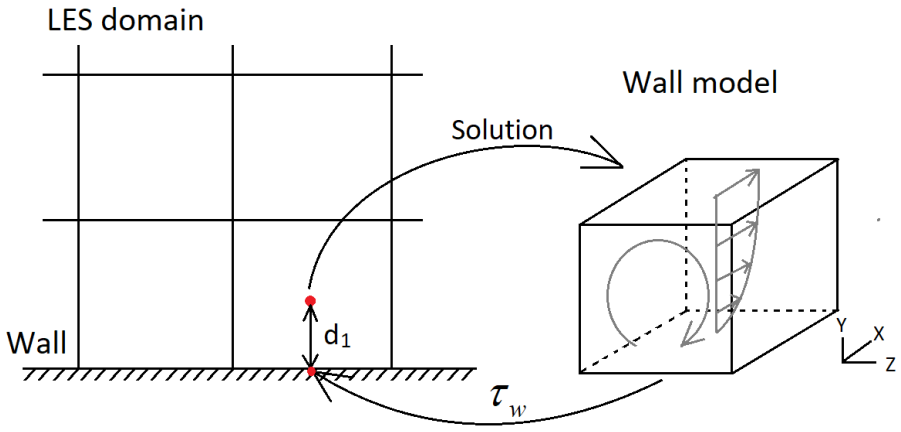

Figure 35: Sketch of coupling the wall stress model with the LES

In Figure 36, the interaction between the wall model and the LES solver is depicted in detail. the wall model is run on each wall cell, and the process begins at each time step of the LES iteration, where the wall model utilizes LES field solutions but operates independently of the LES solver. This independence means that the wall model carries on its data as internal iteration solutions of separate group equations (the SSP updates). One of its solutions, the magnitude of rolls, is further used to simulate rolling effects.

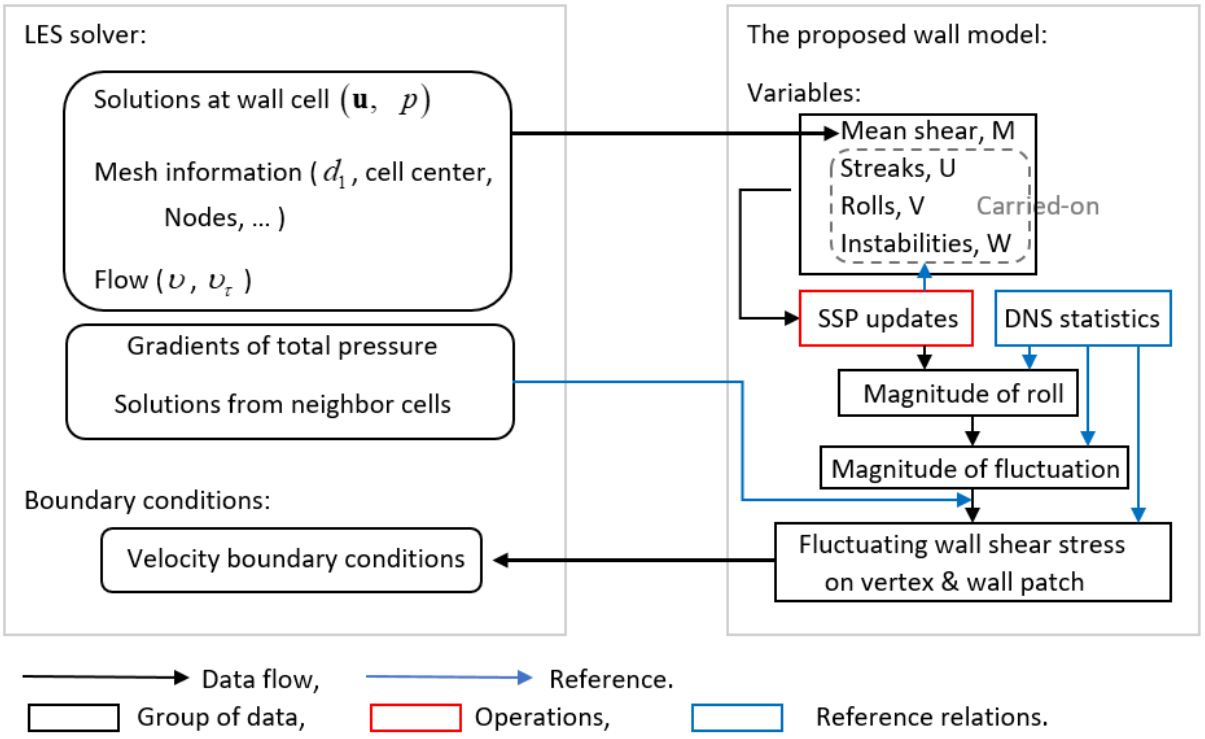

Figure 36: Interactions between the LES and the wall model

To enhance the accuracy of the final results, the wall model employs relationships derived from DNS flow. These relationships may be used to improve the accuracy and ensure the efficiency of calculations of the wall shear stress. To simplify the process, the wall model grids are obtained from the near-wall layer of the LES mesh. This ensures that the wall model is accurate as a close-to-the-wall cell can model the near-wall phenomena more precisely.

In summary, the wall model and LES solver interact through the exchange of boundary conditions, with the wall model providing the LES solver with accurate wall shear stress values that are used as boundary conditions. This process helps to improve the accuracy of the LES simulations and to capture/model the near-wall phenomena more effectively.

4.3.2 Remarks

Suggested near-wall grid height

This thesis assumes that rolling structures exchange vertical layers of shear flow, leading to changes in wall shear stresses. However, the question arises as to under what conditions and in which regions this assumption is valid. To address this question, let's first consider the force balance data from Wei, et al [105], which shows a meso viscous/advection balance layer at about $20 < y^+ < 100$. In the inner boundary layer, the normalized mean momentum equation can be expressed as follows

$$U^+ \frac{\partial U^+}{\partial x^+} + V^+ \frac{\partial U^+}{\partial y^+} = \frac{\partial^2 U^+}{\partial y^{+2}} - \frac{\partial \langle uv \rangle^+}{\partial y^+} \tag{4.19}$$

The balance between the gradient of viscous stress, $\frac{\partial^2 U^+}{\partial y^{+2}}$, and the gradient of Reynolds stress, $-\frac{\partial \langle uv \rangle^+}{\partial y^+}$ is equivalent to the mean advection given by the left-hand side of the mean momentum equation (4.19). The terms corresponding to the gradient of viscous stress and Reynolds stress represent the viscous and Reynolds stresses, respectively, and their ratio $\frac{\partial^2 U^+}{\partial y^{+2}} \Big/ -\frac{\partial \langle uv \rangle^+}{\partial y^+}$ provides information about the local flow characteristics.

Figure 37, which is taken from Wei, et al [105], illustrates that there is a region within $20 < y^+ < 100$ where the alternating effects of viscous or Reynolds stress occur, indicating the presence of rolling structures. In addition, there is another region near $y^+ \sim 50$ where this sign of

this ratio reverses. Curves showing higher Reynolds numbers will lift the rolling structures. However, this suggestion is not entirely accurate. At higher Reynolds numbers, the near-wall region becomes more turbulent, and the intensity of the turbulent fluctuations increases, which can potentially affect the dynamics of the rolling structures. However, it is not necessarily the case that higher Reynolds numbers will always lead to lifting the rolling structures. The behavior of the rolling structures depends on various factors.

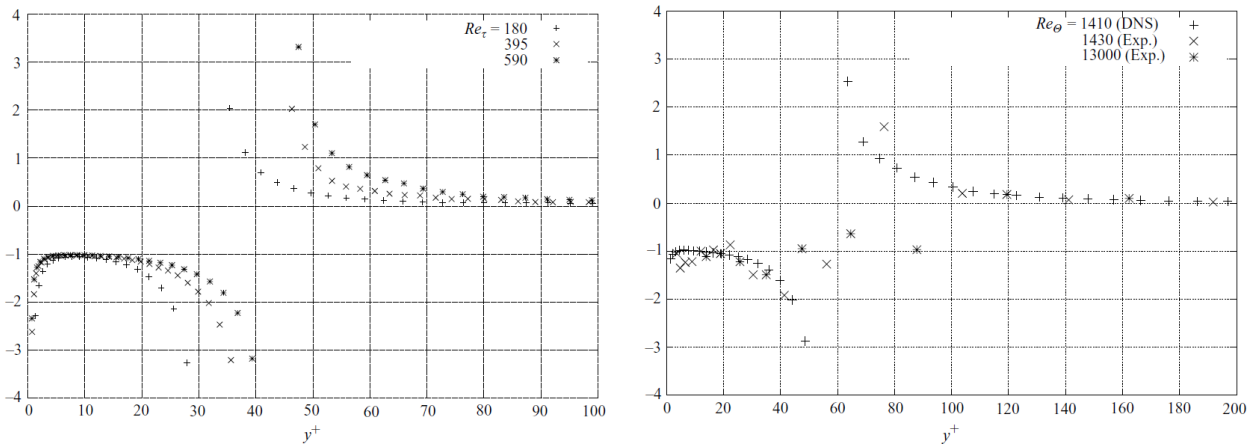

Figure 37: Originally as Figures 1 & 3 in [105], shows the ratio of the gradient of the viscous stress to the gradient of the Reynolds stress in different flow conditions. These figures demonstrate the existence of regions where the alternating impact of viscous and Reynolds stress in a fully developed channel flow DNS [106], a flat-plate turbulent boundary layer DNS [107], and experimental data [36]

These figures suggest that the assumption of rolling structures swapping vertical layers of shear flow and causing wall shear stresses to change is valid in certain regions of turbulent boundary layers, $30 < y^+ < 120$. The rolling effects can explain the above ratio curve's flipped sign and wavey appearance. This thesis suggests the wall adjacent cell height falls into the above region.

Trigger conditions of rolling perturbations

This thesis supports the view that flow in the outer layer is independent and has an influence on what occurs in the inner layer [35]. The outer-region eddies are described as detached freely moving structures [108], whereas the inner coherent structure reveals local phenomena [103][109]. The relationship between large-scale and small-scale structures from the outer to the near-wall region has been the subject of investigation [110] [111] [112].

To simulate the rolls inside the grid resolution, this thesis employs total pressure-vorticity relations that are extracted from DNS near-wall data. In this relation, the extreme value of vorticity, $|\Omega_{max}|$, serves as an indicator of rolls, and its presence is generally followed by the extreme value of the gradient of total pressure in a local field. Figure 20 illustrates this statistical relationship, along with Expression (3.4). In general, the induced wall shear stress (4.18) will be applied after a local total pressure gradient surpasses a given threshold.

To clarify, the gradient mentioned in this context is the directional derivative in the spanwise direction, which is perpendicular to both the wall-normal and the local streamwise directions. In practice, the cross product of the wall-normal vector and a local velocity vector can be used to calculate the spanwise direction. Therefore, the gradient of a variable, such as the total pressure, in the spanwise direction can be evaluated using this cross-product.

A given threshold acts as a trigger for the rolling effects to be applied. If the local total pressure gradient exceeds this threshold, the rolling effects and the induced wall shear stress are applied. This helps to avoid unnecessary computations and improve computational efficiency. A ramp function is applied to the threshold values to gradually increase to the desired value. This

gradual increase helps to avoid numerical oscillations that can occur when the rolling effects are abruptly applied. Once the threshold is reached, the rolling effects are applied by adding the induced fluctuations to the mean wall shear stress.

The local gradient of total pressure is denoted by dp_0, c_p is a constant by default as 0.9, while the local wall shear stress on each vertex of a wall patch is evaluated by

$$\tau_{w,i} = \begin{cases} \hat{\tau}_{w,i}, & dp_0 > p_{0,z}(\Omega, d) \\ \overline{\tau}_w + \left[\dfrac{dp_0 / p_{0,z}(\Omega, d) - c_p}{1 - c_p} \right] \cdot \left(\hat{\tau}_{w,i} - \overline{\tau}_w \right), & c_p \cdot p_{0,z}(\Omega, d) \le dp_0 \le p_{0,z}(\Omega, d) \\ \overline{\tau}_w & dp_0 < c_p \cdot p_{0,z}(\Omega, d) \end{cases} \quad (4.20)$$

A weighted average of the local wall shear stresses evaluated on the neighboring patches that share that vertex may be used to avoid discontinuities in the wall shear stress across different wall patches and to ensure smoothness in the results.

4.4 Summary

This chapter provides the approach to the wall treatment. The process mentioned above helps to improve the accuracy of the LES simulations by modeling the near-wall phenomena more accurately and effectively.

An explicit algorithm updates rolling magnitudes using the SSP dynamical equations. This approach has the benefit of maintaining rolling information in coarse mesh and is relatively independent of spanwise mesh spacing. The process of assigning fluctuations to wall cells using a PDF curve considers the influence of rolling in a real case and simulates these effects using a simplified model. Calibrations were performed to ensure the model's results are reasonable, and

the fluctuating wall shear stress was combined with the mean component and fed back to the LES iterations.

Chapter 5 Validation and Results

In this chapter, the implementation and validation results are presented. The model tests are conducted in two stages, namely isolated and LES-coupled testing. The isolated testing involves tracking variable changes of a single rolling structure from SSP iterations, followed by repeating this process for all possible roll sizes to summarize fluctuations curves as a function of rolling size. Finally, the obtained curves are compared with statistical data from DNS.

The second stage, known as LES-coupled tests, starts by analyzing historical force balance and residual curves to validate the model that never violates conservations. The model's performance is demonstrated by multiple aspects: (1) Tracking changes in fluctuating wall shear stress in a single wall cell with intermediate variable values; (2) a comparison test is carried out on identical settings, with and without the proposed wall model, and distributions of wall shear stress and velocity fields in a vertical spanwise sliding are compared. Quantitative plots of averaged velocity profiles and Reynolds stress components are also presented. Improved fluctuation performance at near-walls is illustrated. (3) Mesh convergence tests were conducted on cubic wall cell meshes with sizes of 60, 75, and 100 in wall units, respectively. The velocity distribution, wall shear stress, and averaged Reynolds stress curves all show consistent and stable results, indicating that the solution is not significantly affected by changes in the mesh size; (4) Model performance on meshes with wider spanwise spacing are presented.

Finally, this chapter provides a review of model highlights, issues, and potential areas for improvement.

5.1 Isolated tests of the rolling model

This section aims to verify the model's behavior in isolated examples by ensuring that the magnitude of fluctuations resulting from a single rolling structure is reasonable under certain mean shear inputs. To achieve this, the magnitude of a roll is initialized, and its development along the SSP iterations is tracked until it reaches a final "steady state," in which the magnitude of rolls and induced fluctuations in wall shear stress are calculated. Convergence history for a typical SSP iteration and intermediate magnitudes' outputs are also presented.

The model assumes that the size of the rolls is related to the height of the wall cells. Therefore, the above-mentioned procedure is repeated for all possible cell heights, and the magnitude of the rolls and induced fluctuations in wall shear stress are calculated to obtain a curve of the fluctuation in roll sizes. This curve is then compared to statistical data from the DNS.

5.1.1 Numerical setup

The SSP requires mean shear inputs, which are the averaged velocity ratios of a local to the outer boundary layer. These ratios can be expressed as a function of cell height using a velocity profile that ideally depends on wall distance/cell height. In this single rolling structure test, the near-wall velocity profile used is the law of the wall (logarithmic law) because (1) a fully developed turbulent boundary layer shares a similar log-law profile and (2) statistical data is very available for comparison. To simplify the process, Reichard's law [63], which seamlessly integrates the linear and log layers into one expression, is used for the near-wall velocity profile.

The SSP Iteration

To ensure stability, the SSP is numerically iterated using the expression (5.1), which includes an error-based term, $e_i \cdot \mathbf{M}_i^t$, added to the RHS of the expression (4.4). This term is proportional to the mean shear error and will decrease as the results converge.

$$\mathbf{M}_i^t = \mathbf{M}_i^{t-1} + \left.\frac{d\mathbf{M}}{dt}\right|_i^{t-1} \cdot \Delta t + e^t \cdot \mathbf{M}_i^t \tag{5.1}$$

Here is the vector $\mathbf{M}_i = \left[M, U, V, W\right]^T$. Only the values of U, V, W ($\mathbf{M}_i$, $i = 2,3,4$) are updated and carried forward for each iteration, and the mean shear, M^{t-1}, is evaluated using LES field values. To avoid implicitness, expression (5.1) is processed in two phases

$$\begin{aligned} \mathbf{M}_i^* &= \mathbf{M}_i^{t-1} + \left.\frac{d\mathbf{M}}{dt}\right|_i^{t-1} \cdot \Delta t \\ \mathbf{M}_i^t &= \mathbf{M}_i^* + e^* \cdot \mathbf{M}_i^* \end{aligned} \tag{5.2}$$

where the intermedia variable $\mathbf{M}_i^*$ determined by the first expression (5.2) contributes to the error term $e^* \cdot \mathbf{M}_i^* = 3 \cdot \frac{M^* - M^{t-1}}{M^*} \cdot \mathbf{M}_i^*$. This term updates the current step of SSP solutions. The detailed process is in Figure 38, which describes how to loop the updating.

The first step of the process involves evaluating the mean shear using LES field information. Following this, the SSP updating process is initiated, which involves iterating through expressions (5.1)and (5.2) while taking into account the current error information for the correction step in (5.2). After the SSP updating process is completed, the program determines whether to continue looping or start the next time step.

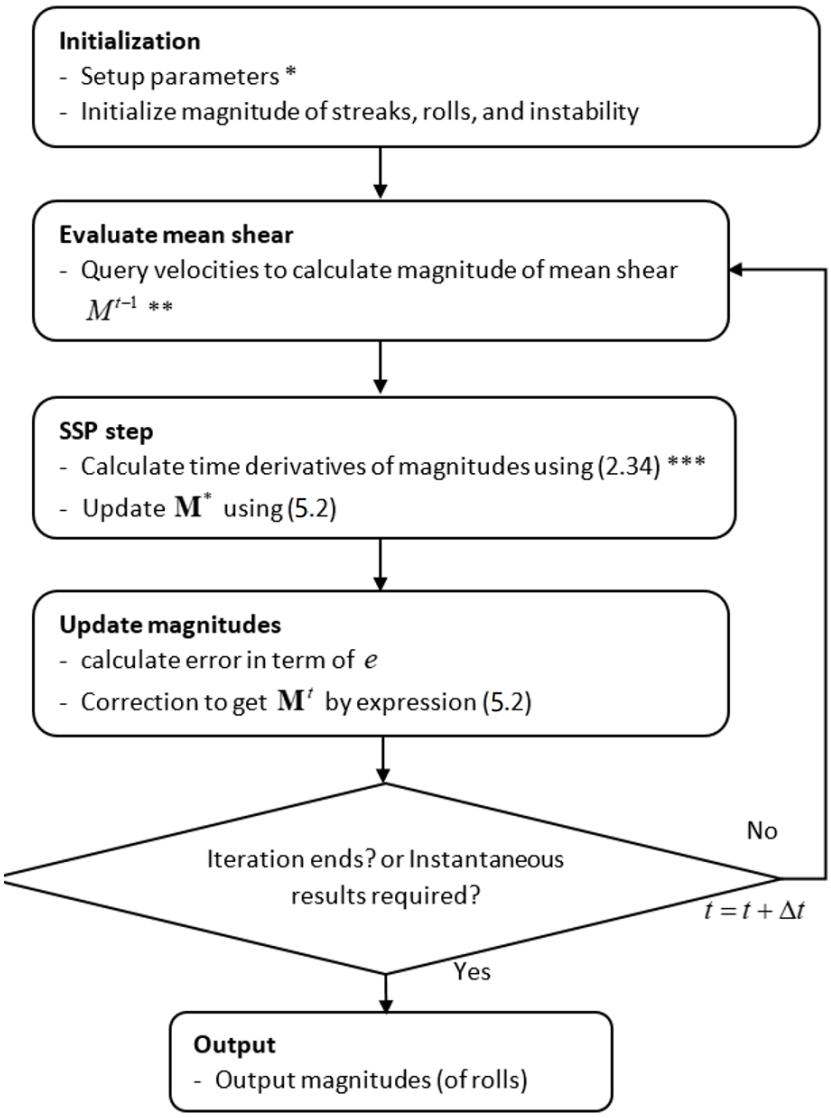

Figure 38: Flowchart of processing the SSP iteration

Some remarks on the flowchart:

* Parameters: $\alpha = 1.155,\ \beta = \pi/2,\ \gamma = \pi$, others are related to these, refer to Appendix in [19].

** The mean shear, $M = \|v_1\| / \|v_\infty\|$, is defined as the ratio of velocities between the center velocity of a wall adjacent cell, v_1, and a reference velocity from the outer boundary layer,

v_∞. In sections 5.1.2 and 0, the reference velocity is set to $v_\infty^+ = \text{loglaw}(2000)$, while v_1 is determined by the mesh size (cell height d_1), $v_1^+ = \text{loglaw}(d_1/2)$. The log law velocity profile can also be replaced with Reichard's law [63].

*** Time derivatives are rewritten as follows in the equation (4.5)

$$\begin{aligned}
\frac{dM}{dt} &= \left(1-M\right)\frac{\kappa_m^2}{R} + \sigma_m W^2 - \sigma_u UV \\
\frac{dU}{dt} &= -\frac{\kappa_u^2}{R}U - \sigma_w W^2 + \sigma_u MV \\
\frac{dV}{dt} &= -\frac{\kappa_v^2}{R}V + \sigma_v W^2 \\
\frac{dW}{dt} &= -\frac{\kappa_w^2}{R}W + \sigma_w UW - \sigma_u MW - \sigma_v VW
\end{aligned} \tag{5.3}$$

From rolls to amplitudes of fluctuating wall shear stress

Once the magnitudes of rolls have been determined using (4.6) and (4.8), the amplitude of wall shear stress fluctuation can be calculated. The process of evaluating wall shear stress fluctuation is shown in Figure 39. Instead of calculating the second invariant of the velocity gradient tensor, the evaluation of core vorticity is performed through an expression as shown in (5.4)

$$\Omega_{\max} = 7.4 \times \left(\frac{\text{loglaw}(d)}{\text{loglaw}(0.2d)} \right) \cdot V \tag{5.4}$$

An analytical solution is not appropriate for coarse resolution. Since the analytical solutions are based on idealized assumptions that the rolling structure is a perfect circular flow, and the input velocities are fine enough to capture small-scale flow features. The above factor,

$7.4\times\left(\frac{\text{loglaw}(d)}{\text{loglaw}(0.2d)}\right)$, is calibrated by comparing the estimated core vorticity curve to the DNS stratified average dots in Figure 43. The process of plotting this curve is in the next section. Figure 40 illustrates both factors from the analytic and calibrated method, with the calibrated segment applied for cell height between 30 to 120 (in plus units).

Traditionally, once the core vorticity is computed, the amplitude of the wall shear stress fluctuation can be derived by integrating the product of the core vorticity and the distance from the wall over the boundary. This integral gives the total contribution of the vortical structures to the wall shear stress fluctuation. However, this method cannot be applied due to its high demands of computational cost and its failure to consider the damping effects of the near-wall boundary layer. Therefore, the linearized statistical relationship, $\Delta_{shear} = 3.293|\Omega_{\max}| - 1.170$, is utilized.

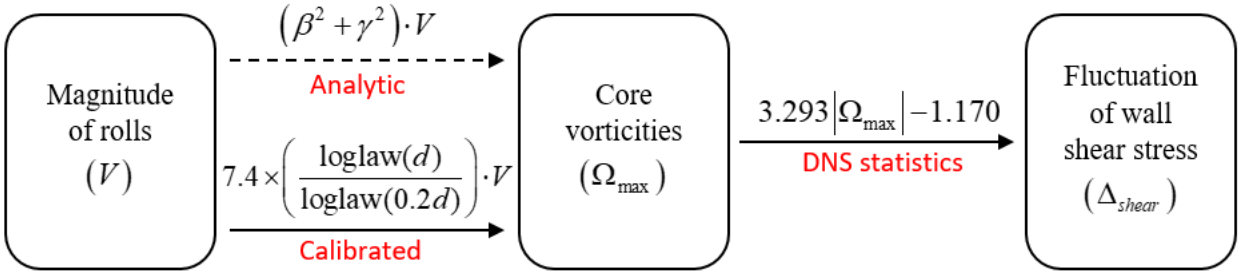

Figure 39: Derivation of the amplitude of wall shear stress by evaluating the core vorticity, which can be done using analytic and calibrated methods. This thesis uses the calibrated one.

In summary, the calibrated method for evaluating core vorticities is used to derive the amplitude of wall shear stress fluctuation by a statistical expression. This method is computationally cheap, and provides a more accurate estimate of the wall shear stress fluctuation compared to analytical solutions, especially for coarse resolutions.

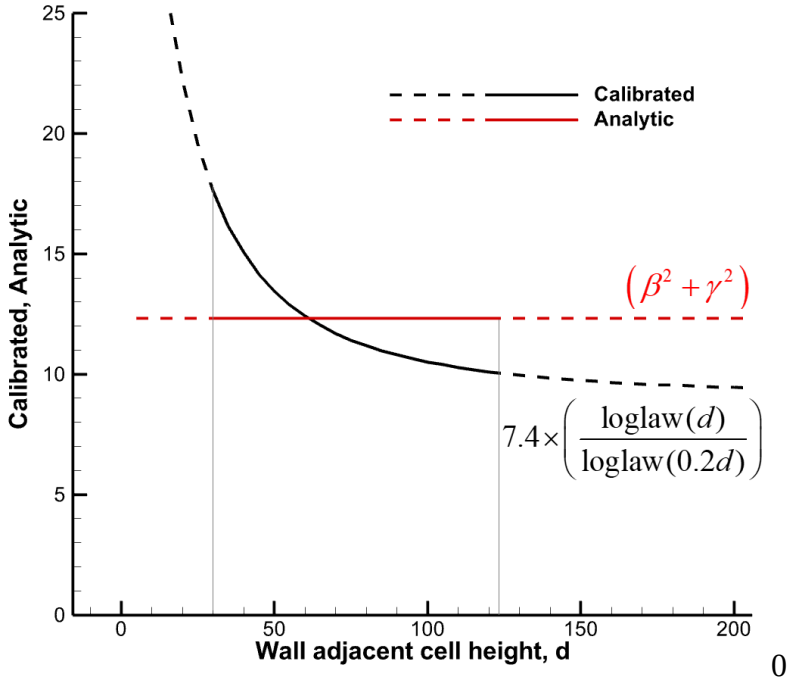

0

Figure 40: Comparison of the multiplier

5.1.2 Evaluate rolls, the SSP outputs

To demonstrate the dynamic behavior of the SSP system, consider an initial mean shear value of $M = 0.435$, which is obtained by approximating the ratio of velocities from a near-wall cell of height 60 using equation (4.3). Set the last three variables $U = 0.2$, $V = 0.03$, and $W = 0.01$ as initial values, and initiate the iteration outlined in the flowchart in Figure 38 to obtain the historical curves shown in solid lines in Figure 41. This thesis also carries out the same procedure with other sets of initial values for the carried-on variables to obtain converged solutions, indicating that a steady shear flow results in a converged solution regardless of the initial values of the carried-on variables. Note that (1) the parameter R-value in the SSP system depends on the cell height and local velocity, and (2) it is assumed that a full-size roll with a diameter equal to $d = 60$ fits inside the grid.

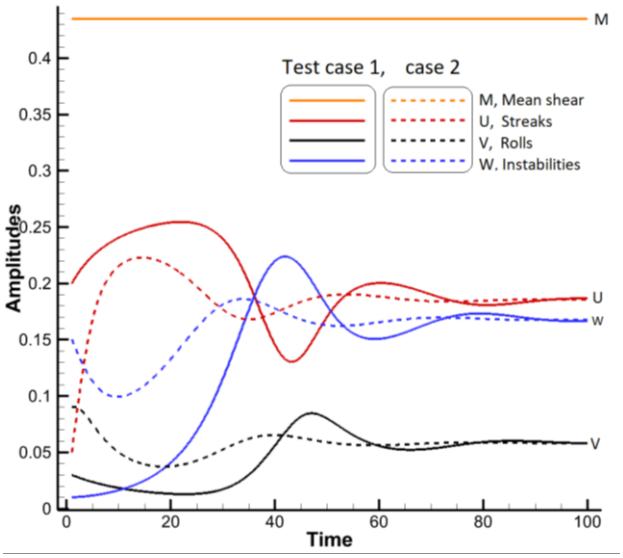

Figure 41: Historical curves of convergence test for the SSP from different initiations

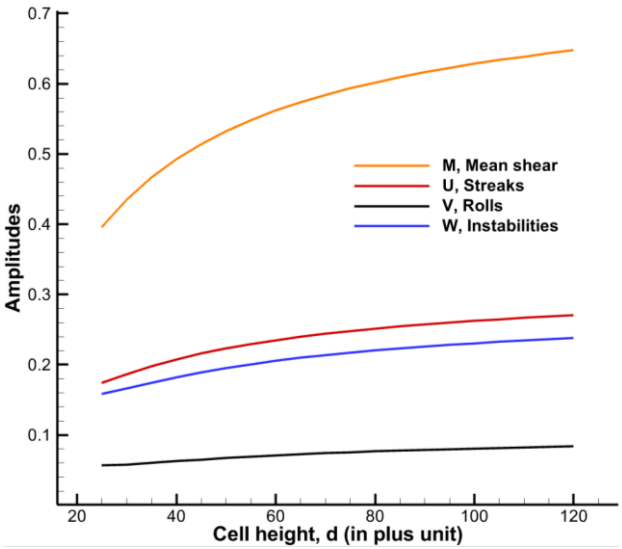

Figure 42: Relations of amplitudes to the wall cell heights

In addition, this thesis conducted further tests by varying the fixed mean shear values, corresponding to a near-wall cell height range of 25 to 120 in plus units, as per (4.3). The final stable SSP amplitudes were recorded and presented as a function/curve of cell height in Figure 42. The black curve shows a smooth transition of rolls across multiple cell heights, which may also be considered the final stable stage based on fixed mean shear input, despite the ongoing dynamic convergence process with time. The limitations of choosing cell height only in a range of 25 to 120 are (1) A laminar flow may occur under 25, resulting in zero amplitudes of rolls, streaks, and instabilities due to lower R values in the SSP, and (2) the Reynolds irrelevant effect causes minor changes in rolling amplitudes above 120, and also most intact rolls observed from the DNS field are less than 120 in diameter.

In the next section, the values of intermediate variables are compared with statistical data.

5.1.3 Core vorticities and magnitudes of fluctuation

The magnitude of core vorticity introduced in the previous section serves as an intermediate value that needs to be compared with statistical data. To ensure accuracy, a calibration technique is employed in Section 5.1.2 that accounts for core vorticities that may vary due to rolling shape deformation and unequal distribution of circular velocity. This technique involves applying an equation (5.4) to evaluate the core vorticity based on different sizes of rolls. The results are then compared to the stratified averaged dots extracted from Figure 18.

The comparison is presented in Figure 43, where the final evaluated core vorticity based on the calibration technique (black curve) matches well with the stratified averaged (red) dots. This well-matching between the evaluated and statistical core vorticities indicates that the modeling of core vorticity is accurate and reliable in a certain range of cell height (assumed rolling sizes). There are only four stratified averaged dots that fall into the desired range of 30 to 120. Based on the positions of the right two dots, the evaluation of core vorticities is slightly overestimated. This trend of overestimation continues when dealing with smaller rolls that are less than 30 in size.

The magnitude of wall shear stress fluctuation is evaluated in Figure 44, represented by the black curve, using the relationship (3.3). between core vorticity and wall shear stress fluctuation amplitude. The red and blue curves show the variations in maximum and minimum simulated wall shear stress as a function of rolling size or cell height. The black curve is slightly overestimated,

but closely follows the trend of the stratified averaged dots, indicating a good agreement between simulation and statistical data.

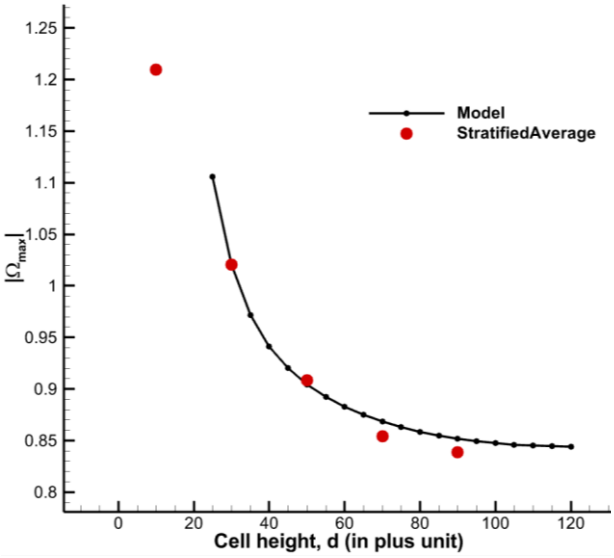

Figure 43 Comparison of modeled core vorticity with the stratified average data from DNS

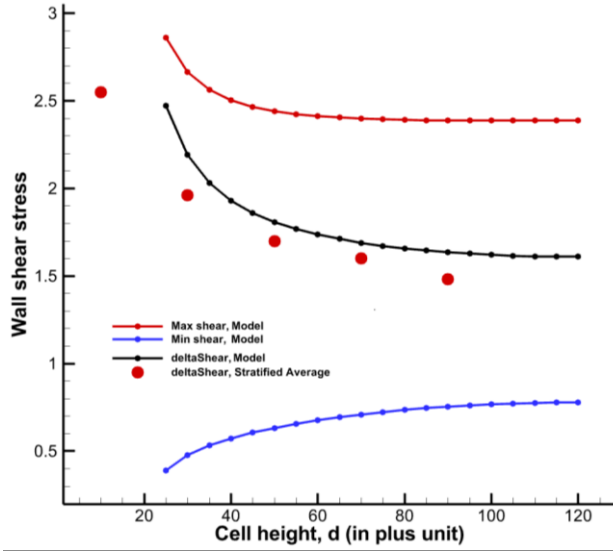

Figure 44: Comparison of modeled amplitude of fluctuating wall shear stress with the stratified average data from DNS

As the cell height approaches the lower and higher limits, both the intermediate core vorticity and fluctuation magnitude show an increasing deviation from the statistical data, although these trends are still within an acceptable range.

5.1.4 Discussion of isolated tests

Section 5.1.1 suggests avoiding the use of analytical methods to determine the induced wall shear stress. In this section as a comparison, a numerical experiment is detailed, which involves assuming mathematical rolling structures inside a boundary layer flow and deriving the stress

tensor to compare it with the one obtained from DNS flow. The purpose of this numerical experiment is to verify that the approach is following the right path, but it makes a shortcut to save computational costs.

To determine induced wall shear stress after receiving rolls from the SSP, a typical mathematical approach involves computing the stress tensor, $T_{ij} = u_i u_j - \tilde{u}_i \tilde{u}_j$, over the near-wall region based on an induced velocity field. From this tensor, near-wall stress can be extracted and then used to approximate the wall shear stress. In the preliminary report of this thesis, this numerical test was conducted and its results were compared with DNS data. The findings suggested that incorporating a series of rolls of varying sizes, which better reflect real flow characteristics, may result in a more accurate induced stress tensor than using a single uniform roll.

A numerical test was conducted to compare the stress tensors of single-size rolls and rolls of increasing size along the streamwise direction in a typical near-wall flow. The stress tensors resulting from both sets of rolls were compared.

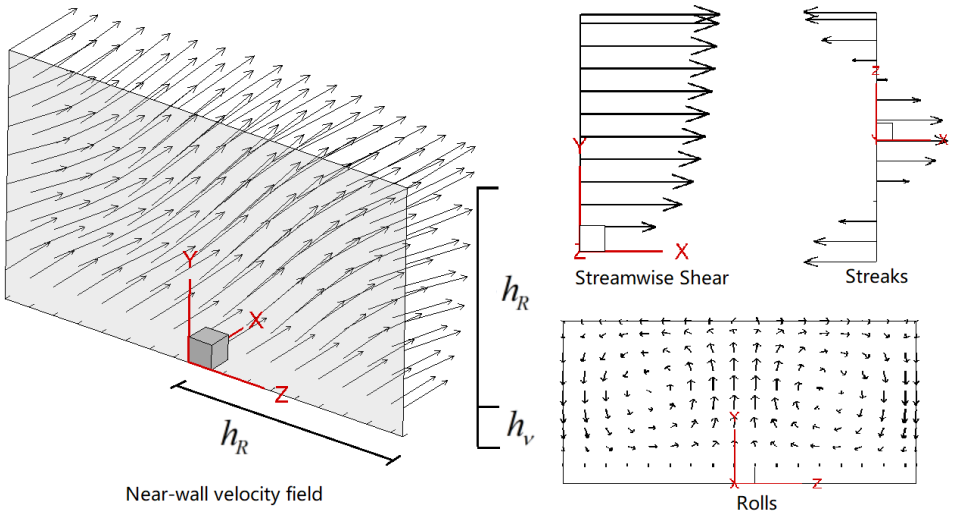

Figure 45: A near-wall velocity field modeled using shear, streak, and roll components/modes

Figure 45 presents a reconstructed near-wall field using shear, streak, and roll components, each assigned with reasonable magnitudes. The mode expressions for these components can be found in expressions (4.2) and (8), (9) in reference [19]. Notably, the equation (4.2) reveals that the roll component takes the form of a uniform cylindrical rolling structure along the streamwise direction, rather than a structure in which the rolling diameter varies with the streamwise location. As illustrated in Figure 46, modeling rolls as streamwise independent vortical structures can achieve agreement with statistical data for components of the Reynolds stress comparison. The modeled field can capture the overall trends of the stress tensor components, with the modeled field slightly underestimating the magnitude of the stress tensor components

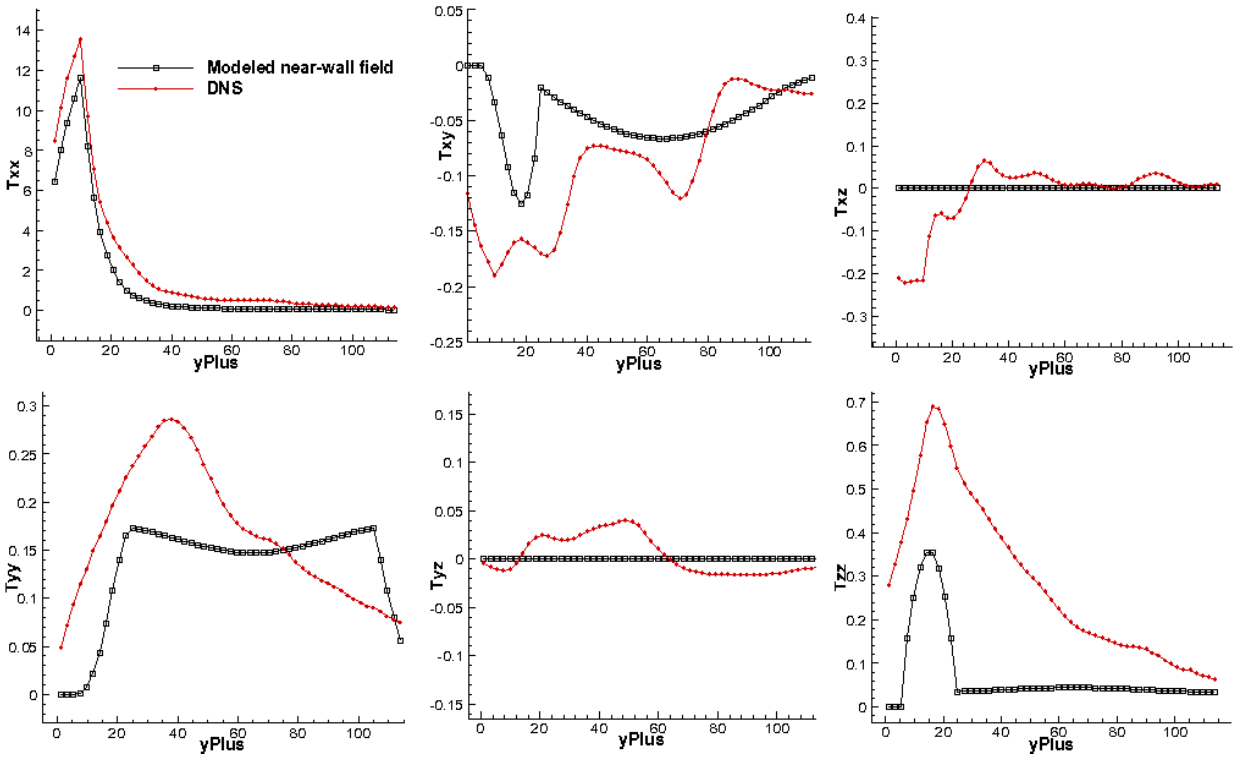

Figure 46: Stress tensor comparison from the modeled field to the DNS. Spatial averaged components of stress tensors as a function of wall distance in plus units are plotted

However, modeling the rolls as a series of gradually increasing vortical structures along the streamwise direction (in Figure 47) is expected to improve the accuracy of the resulting stress tensor, as demonstrated in the Reynolds stress comparison provided in Figure 48.

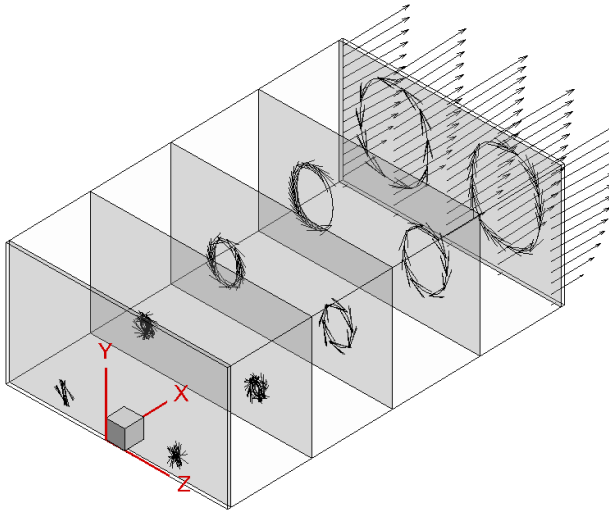

Figure 47: A sketch of modeling rolls as a gradual size-increasing series of vortical structures

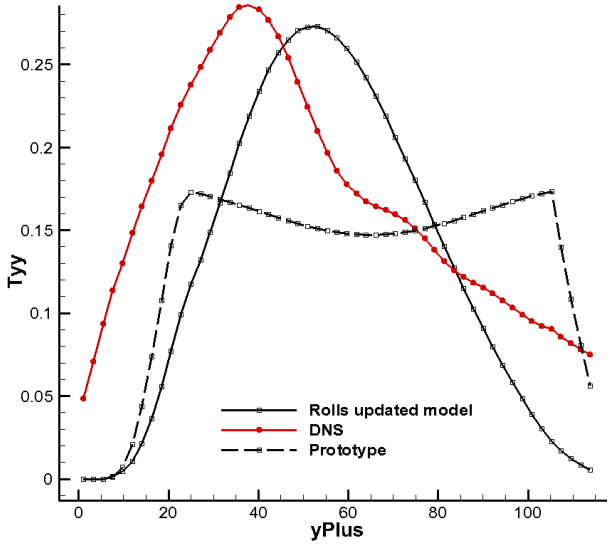

Figure 48: Reynolds stress improvements

Remarks:

(1) Two models of rolling tests described above confirm the hypothesis that rolls alter the velocity field, leading to changes in the stress tensor. This effect is particularly prominent in the near-wall region, where the wall shear stress is impacted.

(2) The computational cost associated with the modeling and sub-filtering of the near-wall field is substantial.

(3) It may be possible to reduce the computational cost by considering only the wall-adjacent tensor contributions to the wall shear stress, but will still assume an equilibrium state.

Thus, this thesis aims to develop a more cost-effective and relatively accurate method to establish the relationship between rolls and fluctuating wall shear stress by utilizing statistical data. The proposed equation (3.3) streamlines the process and demands less computational cost.

5.1.5 Summary

This section presents implementations of updating magnitudes of fluctuating wall shear stress from an input of mean velocity profile. A procedure for updating the SSP equation and utilization of statistical relationship is provided, followed by an example of tracing the development of a single rolling structure. Outcomes from both the magnitudes of core vorticity and fluctuating wall shear stress agree well with the statistical reference from the DNS channel flow. Further discussion by using numerical modeling of rolling structures confirmed their influence on the near-wall stress distributions.

5.2 LES coupled tests

Firstly, the governing equations for an incompressible flow in LES are given by

$$\begin{cases} \dfrac{\partial \tilde{u}_i}{\partial x_i} = 0 \\ \dfrac{\partial \tilde{u}_i}{\partial t} + \dfrac{\partial}{\partial x_j}\left(\tilde{u}_i \tilde{u}_j\right) = -\dfrac{\partial \tilde{p}}{\partial x_i} + 2\nu \dfrac{\partial}{\partial x_j} \bar{S}_{ij} - \dfrac{\partial}{\partial x_j} T_{ij} + s_i \end{cases} \tag{5.5}$$

where $\bar{S}_{ij}$ denotes the rate-of-strain tensor as a function of resolved velocities, $\bar{S}_{ij} = \frac{1}{2}\left(\frac{\partial \tilde{u}_i}{\partial x_j} + \frac{\partial \tilde{u}_j}{\partial x_i}\right)$, and T_{ij} is the unresolved stresses, $T_{ij} = u_i u_j - \tilde{u}_i \tilde{u}_j$, that come from filtered advection with unclosed terms. s_i is a source term. Low-pass filtering is viewed as a spatial averaging, $\tilde{\phi}(\mathbf{x},t) = \int_{-\infty}^{\infty} \phi(\boldsymbol{\varepsilon},t) G(\mathbf{x}-\boldsymbol{\varepsilon},t)\, d\boldsymbol{\varepsilon}$, to remove small-scale information from solutions.

Secondly, The PimpleFoam solver in OpenFoam is designed as a "transient" SIMPLE solver. PIMPLE algorithm used in this solver stands for "Pressure Implicit with Splitting of Operators" to solve the Navier-Stokes equations. This algorithm works by dividing the Navier-Stokes equations into two parts, a pressure equation, and a velocity equation. The velocity forecast is produced first, followed by an update to the pressure. This approach enables the solution to be stabilized and improves computational efficiency.

The Pimple algorithm used in OpenFoam is an implicit, multi-time-step approach, which means that the pressure and velocity equations are calculated simultaneously and the solution is updated at multiple time steps. This allows for accurate treatment of pressure fluctuations and complex flow patterns in turbulent flows. Figure 49 of the PimpleFoam flowchart shows how an inner iterative routing of pressure and velocity adjustments allows for the accurate treatment of pressure fluctuations and complicated flow patterns in turbulent flows.

To model turbulence, the Smagorinsky turbulent model is used in PimpleFoam. This model assumes that the turbulent eddies are characterized by a characteristic length scale, which is modeled using the Smagorinsky constant. The model applies a subgrid-scale stress tensor to account for the effects of turbulent eddies that are smaller than the computational grid size.

A quick listing of schemes for derivatives is in Table 3.

Derivatives	**Schemes**
Temporal derivative	Backward
Spatial gradient	Gauss linear
Divergence	Gauss linear
Laplacian	Gauss linear corrected

Table 3: Derivative schemes in case studies

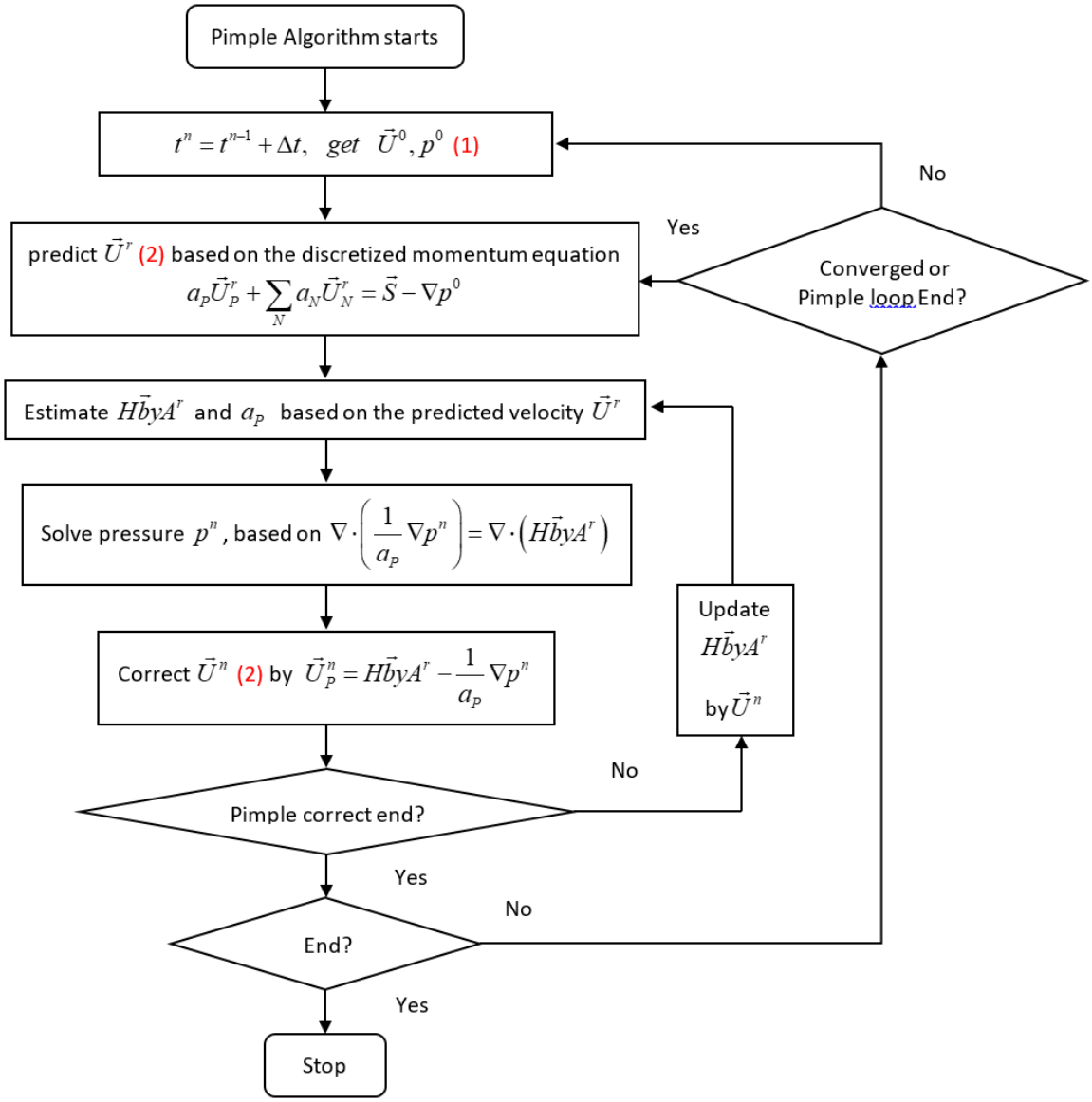

Figure 49: Flowchart of the PimpleFoam algorithm

5.2.1 Coupling the wall model with the LES

As explained in section 2.2.1, the wall shear stress model used in this study utilizes a field solution to estimate the boundary condition, which is then input back into the LES domain. The proposed wall model attempts to replicate the effects of fluctuations induced by near-wall rolls.

Once these fluctuations are obtained, they are added to the current averaged wall shear stress to construct a velocity boundary condition. This approach simulates the effects of the near-wall rolls, which are a crucial component of near-wall turbulent flow and are often ignored in coarse-resolution simulations.

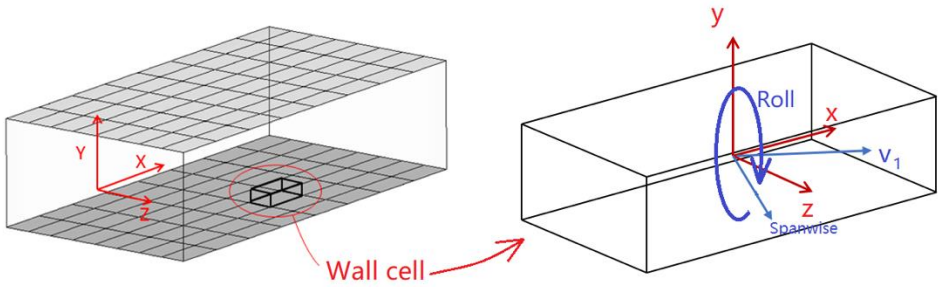

Figure 50: Sketch of a wall cell and a roll modeled inside

A wall cell containing a roll is illustrated in Figure 50, with the roll shown by a blue circle. This roll is assumed to be centered at the velocity of the cell, v_1, and extends across the entire height of the cell. The local spanwise direction is estimated by computing the cross-product of the streamwise unit vector and the wall-normal vector.

The procedure for calculating the velocity boundary condition is presented in Figure 51 as a flowchart. This process is performed on all wall cells whenever an update of the velocity boundary conditions is required by the LES solver.

At the beginning of the process, the solver checks whether it is currently in the outer loop of time-advancing. If it is, then the SSP update algorithm outlined in Figure 38 is executed to synchronize all magnitudes $\mathbf{M}$ and obtain rolling magnitudes for future fluctuations. On the other

hand, if it is within the Pimple loop, the solver skips the SSP updates and reuses the current roll magnitudes.

Secondly, obtain the current data as well as evaluate the mean and fluctuation components of the wall shear stress are evaluated. Now, the direction of the near-wall streamflow is assumed to be the same as the velocity vector at the cell center (as indicated by $\mathbf{v}_1$ a vector in Figure 50), and the rolls inside each cell are oriented in the same way. The focus of the thesis is not on modeling behaviors but rather on calculating the effects of rolls on walls. As described in sections 4.2.4 and 4.2.5, the local spanwise direction is necessary for accurately assigning shear stress on wall-attached nodes.

Thirdly, the computation of both the fluctuation and mean components of the wall shear stress. The magnitudes of the fluctuations are evaluated using equations (5.4) and (4.8), and the specific process is illustrated in Figure 39. The mean component of the wall shear stress is calculated by solving for the friction velocity using the Newton-Raphson technique and equation (5.6)

$$u_1^+\left(u_\tau\right) = f_{profile}\left[y_1^+\left(u_\tau\right)\right] \tag{5.6}$$

The left-hand side is the definition expression of $u^+\left(u_\tau\right)$ from (2.3), while the right-hand side can be either a log-law profile or Reichardt's velocity profile [63]. In this thesis, the local mean value is determined using neighborhood averaging, $\overline{\tau}_w = \frac{1}{2}\left[\overline{\tau}_{w,L} + \overline{\tau}_{w,R}\right]$, where the subscripts L and R represent two neighbor cells on either side of the spanwise direction. This approximation is made possible by a structural hexagon mesh, which perfectly aligns with the current channel flow case

being simulated. This allows the spanwise dimension to be simplified as the z dimension, and all mesh cells to have the same size and orientation.

Fourthly, assign wall shear stress to vertices using the algorithm detailed in section 4.2.5. Finally, a velocity boundary condition with a magnitude

$$u_w = u_1 + \frac{\tau'_w + \overline{\tau}_w}{\nu} \cdot d_1 \tag{5.7}$$

is calculated and sent back to the LES domain.

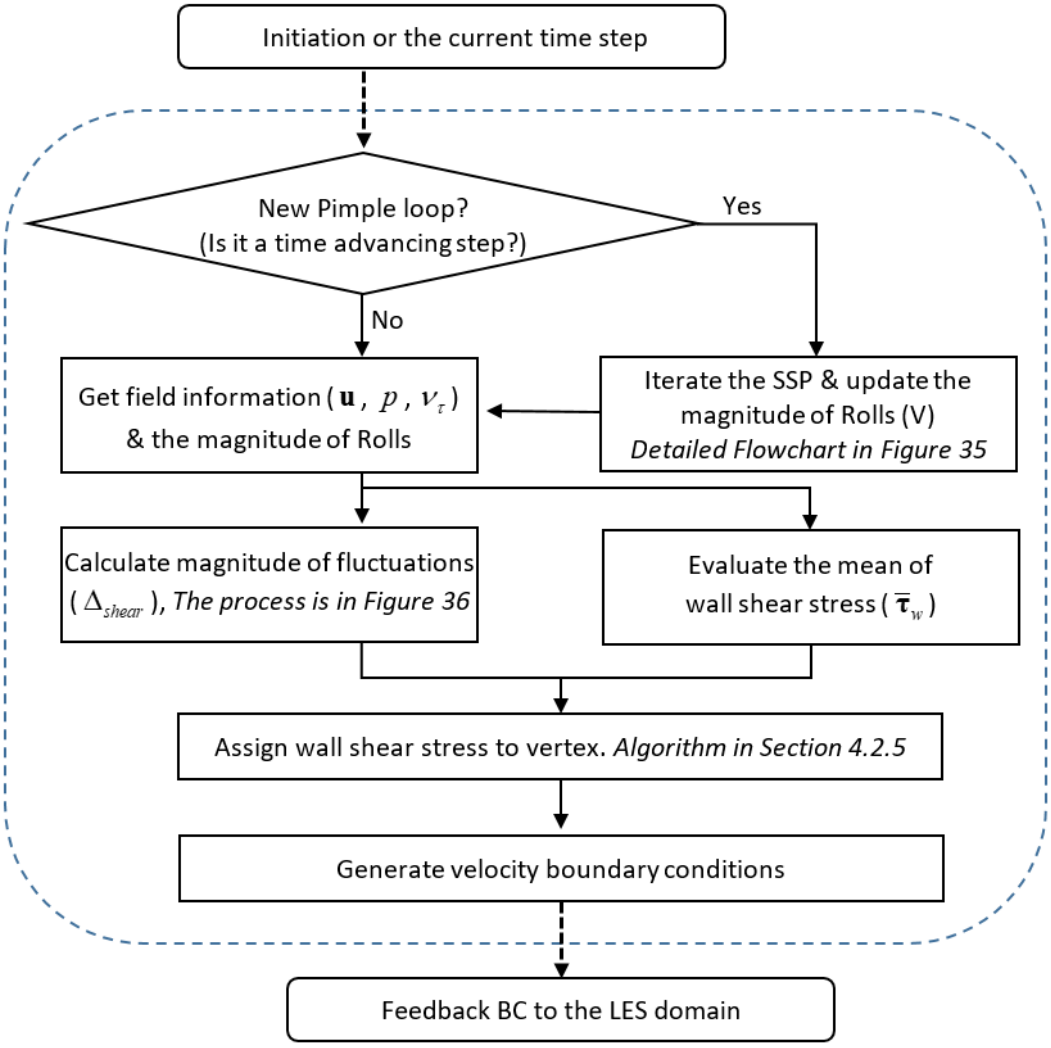

Figure 51: Process of the wall model

It is important to note that the velocity boundary condition obtained in the previous steps is a vector whose direction is determined by the cell center velocity. However, using this vector directly would probably violate the no-penetration requirement at the wall. Therefore, the wall-normal component of the velocity vector is removed before sending it back to the LES domain.

5.2.2 Channel flow configurations

A channel flow driven by pressure is characterized by two parallel plates, as illustrated in Figure 52. The streamflow moves in the positive x direction. To create a fully turbulent velocity field, cyclic boundary conditions are imposed on the inlet and outlet. Meanwhile, two sides (left and right) are set as cyclic conditions, enabling the repetition of the flow of exiting and re-entering from the sides. This setup offers a perfect wall-bounded fully turbulent velocity field at the desired Reynolds number.

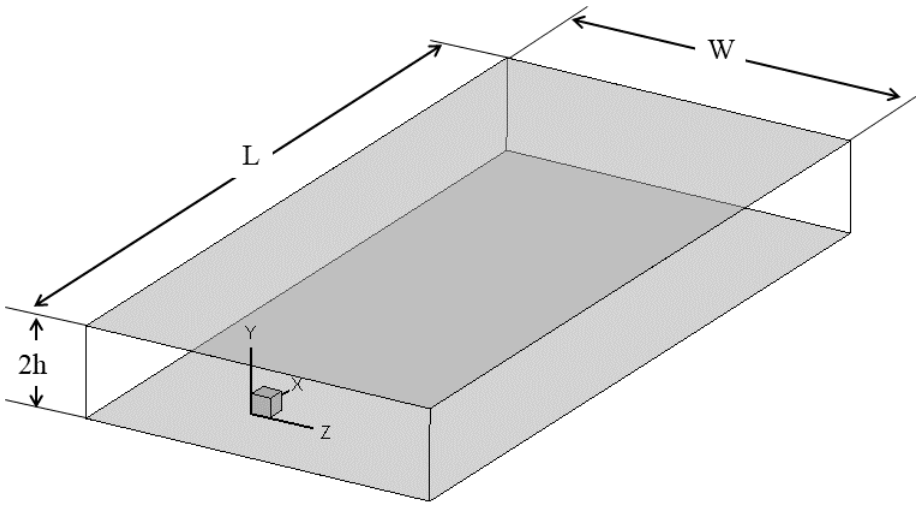

Figure 52: Sketch of a parallel channel

A pressure gradient, $\mathbf{s}$, is prescribed for the right-hand side of the equation (5.5) to simulate a channel flow. According to the force balance in the streamwise direction, the friction force from the top and bottom walls must be equal to the pressure force difference between the inlet and outlet, suggesting that

$$\frac{dp}{dx} = \frac{\tau_w}{h} \tag{5.8}$$

Based on the concept of friction velocity, $u_\tau = \sqrt{\frac{\tau_w}{\rho}}$, and a constant fluid density of $\rho = 1$ to obtain a unit wall shear stress, $\tau_w = 1$, the source term of the pressure should be set to $s_1 = \frac{dp}{dx} = \frac{\tau_w}{h} = 1$. As a result, the friction Reynolds number can be calculated

$$\mathrm{Re}_\tau = \frac{u_\tau h}{\nu} \tag{5.9}$$

A standard case with a friction Reynolds number of $\mathrm{Re}_\tau = 1{,}000$ [30] can be defined by setting the kinematic viscosity $\nu = 0.001\left(m^2/s\right)$. This configuration results in an estimated bulk velocity of approximately $20\left(m/s\right)$ and a physical Reynolds number approaching $\mathrm{Re} = \frac{u_{bulk} h}{\nu} \approx 20{,}000$

To simplify the mesh, a structural hexahedral mesh is employed in the simulation. The mesh comprises two identical blocks that are symmetric about the xz-plane. Each block is uniformly distributed with nodes along the streamwise (x) and spanwise (z) directions. The distribution along the wall-normal direction is stretched, with a minimum near-wall cell height of 60 plus units. One block contains (150, 16, and 100) cells in the (x, y, and z) directions, respectively. In total, comprises approximately 518,534 cells, which is approximately half a million cells.

The boundary conditions for the channel flow cases are listed in Table 4. The initial condition for both pressure and turbulent viscosity is uniformly set to zero. However, to ensure turbulence development, perturbation is applied to the velocities. The dimensions of the channel flow cases are as follows: $L = 9$, $W = 6$, and $h = 1$.

	Velocity ($\mathbf{u}$)	Pressure (p)	Turbulent viscosity(ν_τ)
Walls (upper & lower)	Current wall model	Zero Gradient	nutkWallFunction
Sides	Cyclic	Cyclic	Cyclic
Inlet & Outlet	Cyclic	Cyclic	Cyclic

Table 4: List of boundary conditions

5.2.3 Results and discussion

This section aims to validate the simulation results by first verifying the conservation laws and then evaluating the performance of the model. Various aspects have been taken into account, such as velocity distribution, averaged profiles, mesh convergence, and computational costs. For comparison purposes, results from DNS simulations and control groups where the proposed wall model is not applied are utilized.

Mass and momentum conservations

This subsection presents historical curves that demonstrate the validation and convergence of a test case with a consistent near-wall cell height of 60 plus units. The objective is to ensure that the proposed boundary condition does not violate force balance, where the pressure gradient force should be equivalent to wall friction in the channel flow.

Figure 53 displays a historical curve of the total force in the x-direction component, plotted as a function of time. The Y-axle value (total force) is obtained by subtracting the wall friction and

then normalizing it, that is $\frac{dp}{dx}\cdot L\cdot\left(2h\cdot W\right)-2\cdot\tau_w\cdot\left(L\cdot W\right)$, which is unitized to be $\frac{dp}{dx}-\tau_w$. In the OpenFOAM, the pressure gradient in the x-direction, $\frac{dp}{dx}$, can be found in the printout/log file, after the bulk velocity has been specified in the file "transportProperties". The friction is averaged from the top and bottom walls, to call a force function in the library "libforces.so" to do so.

Figure 54 shows the historical residuals, plotted against the simulation time. The residuals represent the difference between the computed values and the actual values and are used to assess the convergence of the simulation. There are four equations solved in the LES, one mass and three for the conservation of momentum in the three spatial directions. As shown in Figure 54, all residuals are small and steady after the initial seconds, which indicates the difference between each time step solution is relatively small.

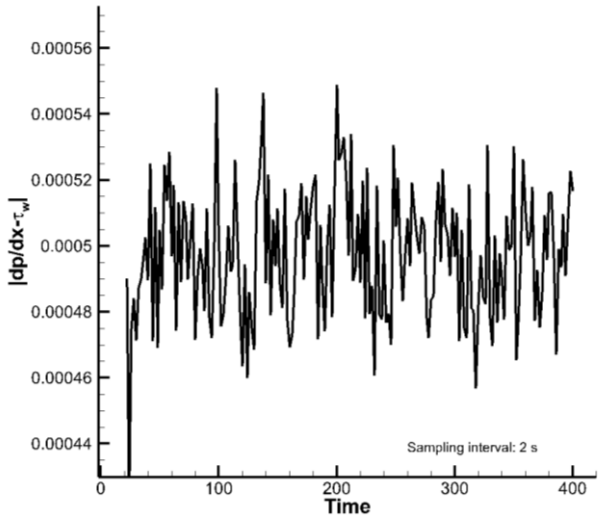

Figure 53: Force balance

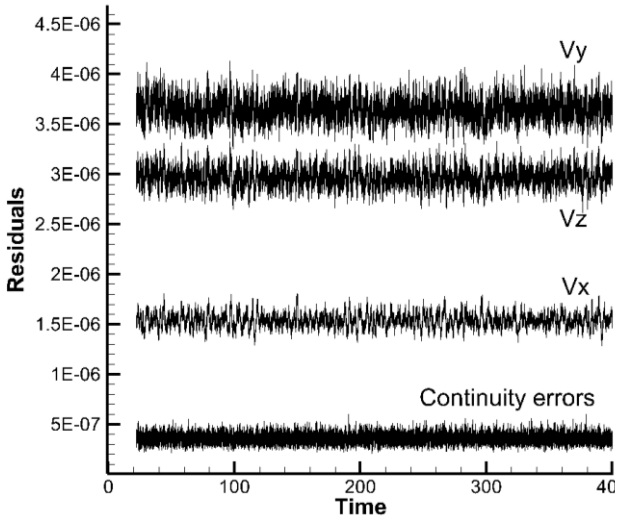

Figure 54: Residuals

SSP and wall model performance

This subsection aims to demonstrate the functionality of the proposed model by examining the changes in variables within a fixed near-wall cell to verify if the model works as expected.

Generally, the wall model collects field velocities and estimates the mean shear value of the local streamwise flow for each time step. However, this thesis attempts to trace changes in variables in certain key steps inside the wall function. After several hundred seconds of channel flow development, the variable curve becomes reasonably steady.

Figure 55 demonstrates the changes in variable values within a near-wall cell located at the bottom wall in the middle of the computational domain. The historical curve in Figure 55(a) shows the mean shear inputs supplied to the SSP, which is used to obtain a roll magnitude curve in Figure 55(b).

In Figure 55 (c), the black curve presents the changes in the absolute values of the local derivative of the total pressure with respect to the spanwise direction. The red curve presents the threshold, which in this thesis is set to 90% of a statistical value obtained from $p_{0,z}\left(\Omega, d\right)$ in (3.6). The algorithm compares the field value with the threshold and decides when to introduce fluctuations based on the trigger mechanism, which is explained in detail in (4.20).

According to this (4.20), the proposed trigger mechanism induces fluctuations in the local wall shear stress conditionally. Figure 55(d) plots the curves showing the differences in the wall shear stress values before and after the wall function processing. The red curve represents the averaged wall shear stress before the processing of the wall function, and the black curve represents the exit values. For field values greater than the threshold, the wall model adds induced fluctuating components to the mean wall shear stress. Since the averaging processes cover multiple cells, it may be difficult to examine the exact fluctuation values by tracing information from a single cell. However, for those under the trigger conditions, no perturbations shall be applied. This would be much easier to check. The blue dots in Figure 55(d) represent the moments when the gradient values are below the threshold, which means that the wall model of the adding fluctuation function should be deactivated. The matching agreements of black and red curves during these moments indicate that the wall model functioned as designed.

As a conclusion of plots in Figure 55: (1) the curve of rolling magnitudes responds with the mean shear and seems relatively steady; (2) the trigger mechanism functions as designed. Overall, these results demonstrate that the proposed wall model functions as expected inside a single wall cell.

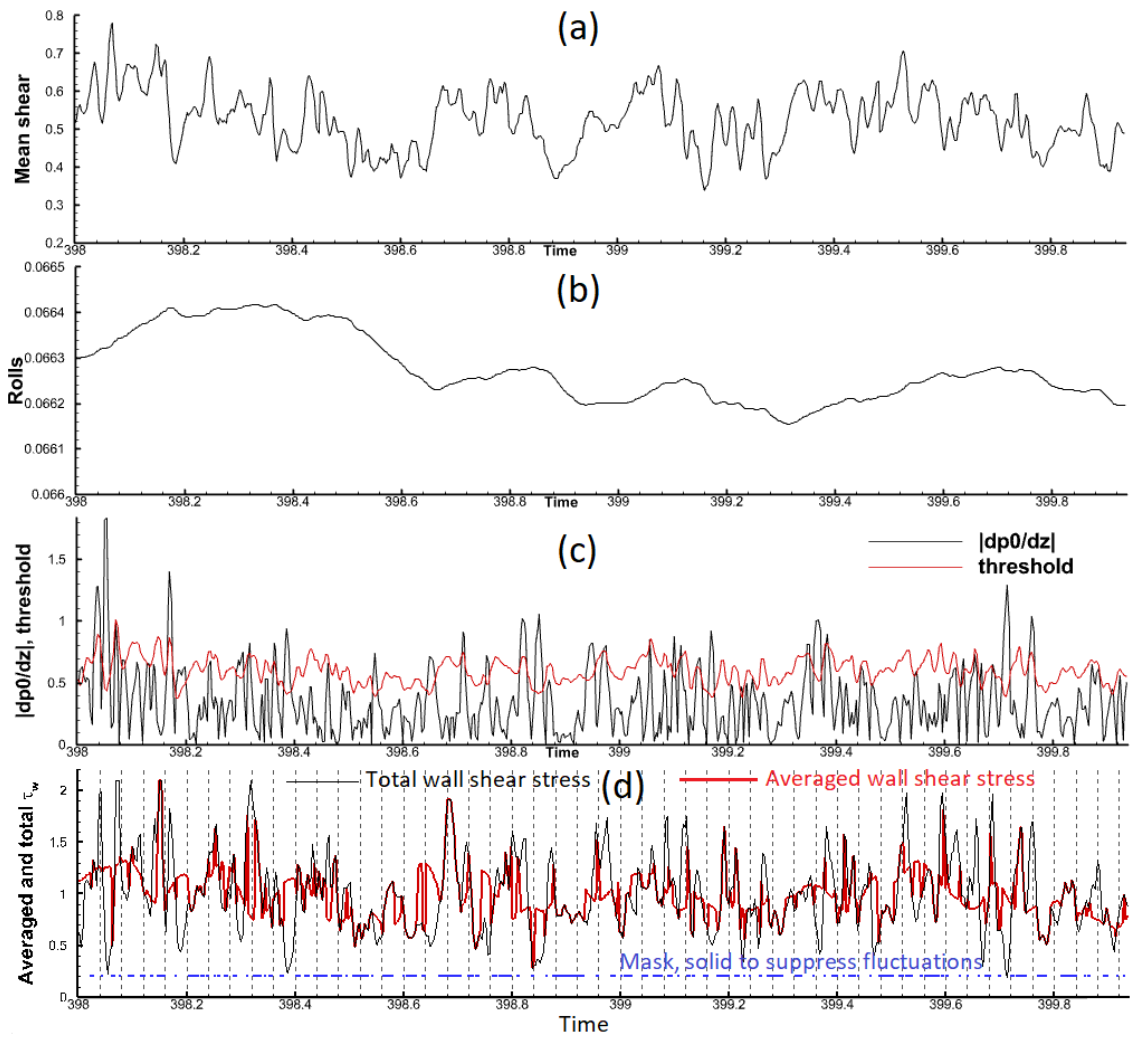

Figure 55: Tracing the evolution of intermediate variables for a single wall cell during the LES iterations

Instead of examining Figure 55, the rolling magnitude within a single cell, Figure 56 shows the development of averaged magnitudes across all bottom wall cells in the computational domain. The x-axis in Figure 56 represents simulation time. It can be observed from the plot that after about

100 seconds, the values of the averaged magnitudes of rolls become relatively steady for the channel flow case.

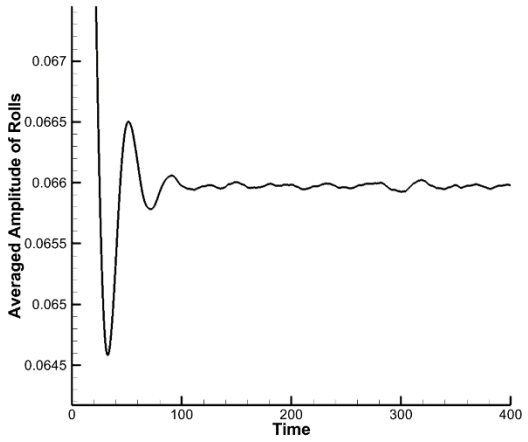

Figure 56: Changes in the bottom wall's averaged rolling amplitude

Comparisons of velocity and total pressure fields

In this subsection, the computational results of the LES perspective are presented. To demonstrate the performance of the model, certain results are compared with those of the control group, which shares identical settings, except for replacing the proposed wall model by using no-slip velocity boundary conditions.

Figure 57 provides surface contours of wall shear stress (at t=398s) for the control group (on the left) and the modeled case (on the right) to compare their distributions on the bottom wall displayed with contours that share the same scaling. This scale is used to indicate the magnitude of the wall shear stress τ_w , which is evaluated by a finite difference approximation of its definition in (5.10)

$$\tau_w = \nu \frac{\partial \|\mathbf{u}\|}{\partial y} \approx \nu \cdot \frac{\|\mathbf{u}_1 - \mathbf{u}_w\|}{d_1 - 0} \tag{5.10}$$

The visualization of wall shear stress contour plots can reveal elongated streaks as wall shear stress spots in the streamwise x-direction. These streaks are due to spanwise low and high speed swapping that is believed to be associated with near-wall rolling structures, meaning the spots are localized under rolls. The detection of these features can provide insights into the near-wall rolls and is relevant for the simulation of wall-bounded flows. The wall modeled case in Figure 57 exhibits a greater number and density of wall shear stress spots. They show a directional elongation in the streamwise direction and a distinct pattern. The greater contrast in color (red and blue) suggests that the fluctuating component of the wall shear stress is more clearly captured/modeled.

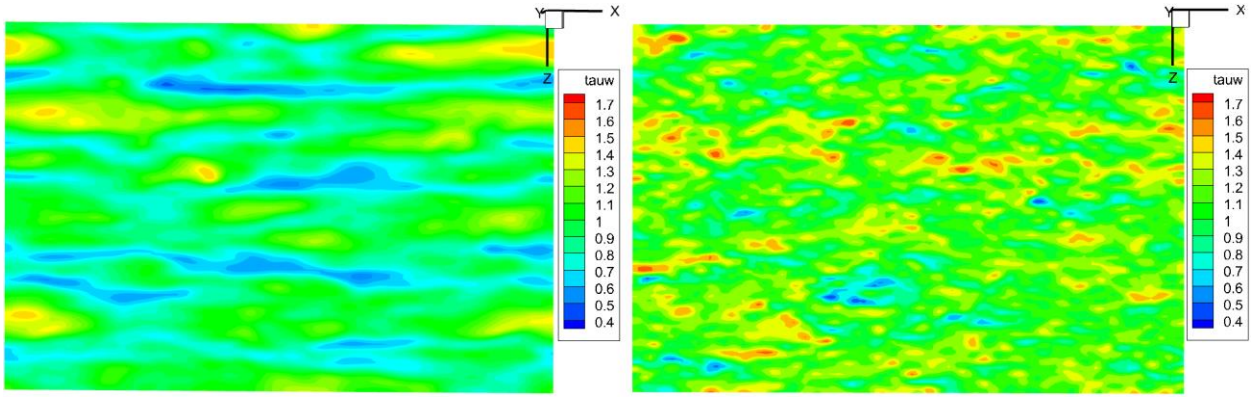

Figure 57: Comparison of wall shear stress magnitudes, (Left) the base case, and (Right) the modeled case, at the bottom wall, t=398s

The PDF profiles of the wall shear stress in Figure 58 provide further evidence that the fluctuating component is more accurately modeled in the wall modeled case. Figure 58 contains three curves: the black curve represents the wall modeled case, the blue is from the control group,

and the red curve represents a DNS result. The wall modeled curve has a wider distribution along the x-axis (representing stress) and a lower profile height compared to the curve of the control group. This wider distribution indicates better modeling of the fluctuating component of the wall shear stress.

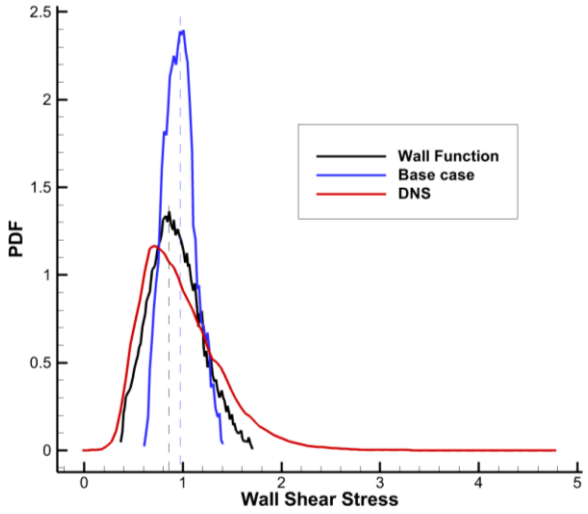

Figure 58: PDF comparison

In Figure 58, the peak probability values of wall shear stress in the wall modeled case are shifted to the left compared to the control group. This is consistent with the numerical testing results of rolling-induced fluctuations in Figure 26. Furthermore, this agreement is much closer to the DNS curve. The PDF shape of the wall-modeled case appears to be more skewed rather than symmetric, which is consistent with the behavior of near-wall turbulence.

In conclusion, after comparing the PDF curves from Figure 58, the wall model provides several improvements: (1) the PDF from the model is generally closer to the DNS profile, wider and flatter; (2) The peak location of the modeled case (the highest probability value of wall shear stress) is shifted much more to the left than the location of the mean averaging value of 1; and (3)

The PDF profile of the modeled case is skewed more to the left about its dashed axis. All three features are consistent with those observed in the DNS profile.

Figure 59 presents a comparison of streamwise velocity contours on a vertical slicing plane in the center of the channel domain, located at x=4.5. Subfigure (a) of the control group shows fewer near-wall structures and relatively larger scale features closing to wall surfaces on top and bottom sides compared to subfigure (b) of the modeled case. This difference results in fewer fluctuation spots in the control case presented in Figure 57. On the other hand, the modeled case exhibits more near-wall smaller features, indicating better modeling of the near-wall turbulence. Furthermore, the top and side view of a DNS field in Figure 60 presents detailed and similar near-wall features as the modeled case, suggesting that the modeled case provides a more comparable field in terms of both the wall shear stress distribution and internal near-wall velocity contour. Overall, the comparison of near-wall velocity fields within a channel provides evidence that the wall modeled case better models the near-wall turbulence compared to the control group.

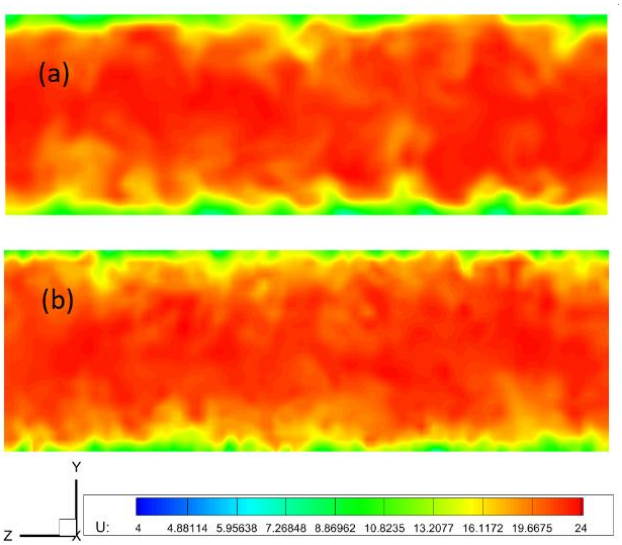

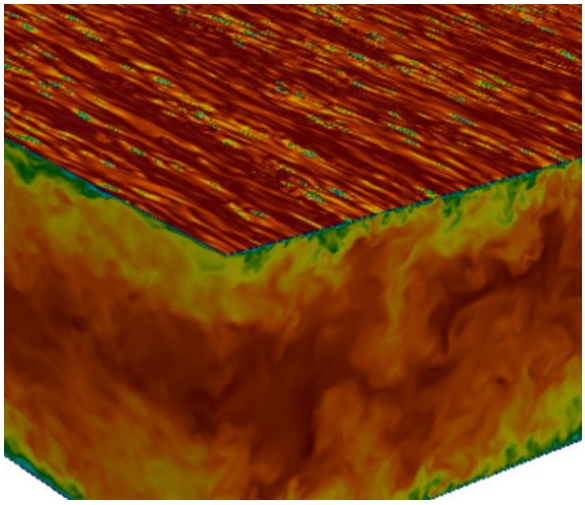

Figure 59 streamwise velocity distribution, generated by using a vertical plate cut through the middle of velocity fields.

Figure 60 the DNS results, this figure is borrowed from the DNS photo gallery in [104]

To provide clarity on the claims of enhanced modeling of near-wall features, Figure 61 and Figure 62 present Iso-contours and streamlines plots as details to the fields shown in Figure 59. While both figures are based on identical velocity and pressure fields on the same vertical sliding plane, only the lower half of the field is presented for being concise. A streamline is a visual representation of the possible trajectory that a particle may follow, as it follows a path tangent to the local velocity vectors. In Figure 61, only the velocity components corresponding to the spanwise and wall-normal directions are contributed to streamlines. Smaller yet more closely spaced wall-attached rolls are exhibited in Figure 61(b) of the wall modeled case. These rolls have a significant impact on field velocity distribution and are strongly related to the background contours of total pressure distributions. Consequently, the presence of fewer and larger size of wall-adjacent rolls leads to (1) a less change in field velocities along the spanwise direction, which, in turn, results in less alteration on wall shear stress (streaks); and (2) a less momentum exchange along the spanwise direction, which presents a less smooth gradient of total pressures distribution.

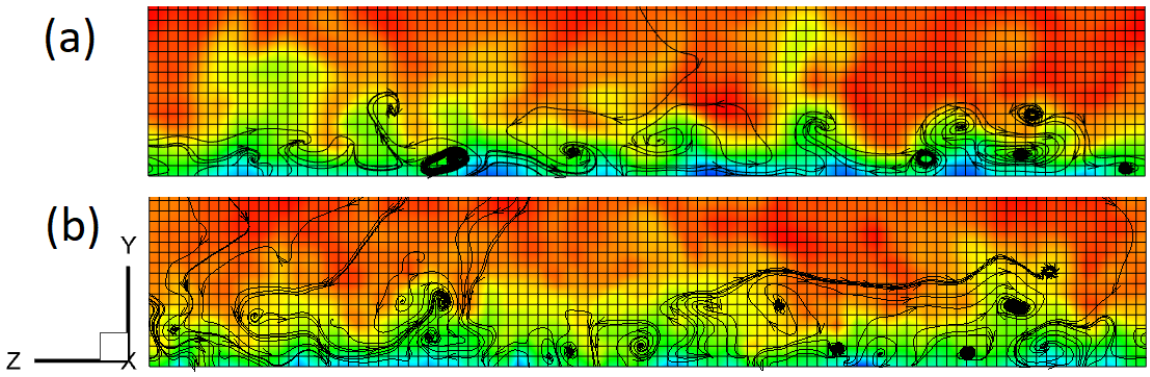

Figure 61: Streamlines and contours of total pressure for (the upper) base case and (the lower) modeled case, obtained by cutting a vertical plate through the center of the velocity fields, contours based on values of total pressure, and streamlines are from velocity vectors (in y and z components).

Regarding the second point mentioned earlier, Figure 62 presents a comparison of iso-contour lines, demonstrating that the near-wall total pressure layers are considerably smoother in the modeled case. Iso-contour lines depict a visual representation of constant values in a scale field. The near-wall lines shown in Figure 62(b) of the modeled case exhibit smaller wavy arcs, indicating a more uniform distribution of variables in the spanwise direction. In contrast, the larger near-wall rolling structures observed in the control group in Figure 61(a) lead to greater oscillations at corresponding locations of iso-contour lines in Figure 62(a), resulting in a more rough spanwise distribution of the total pressure.

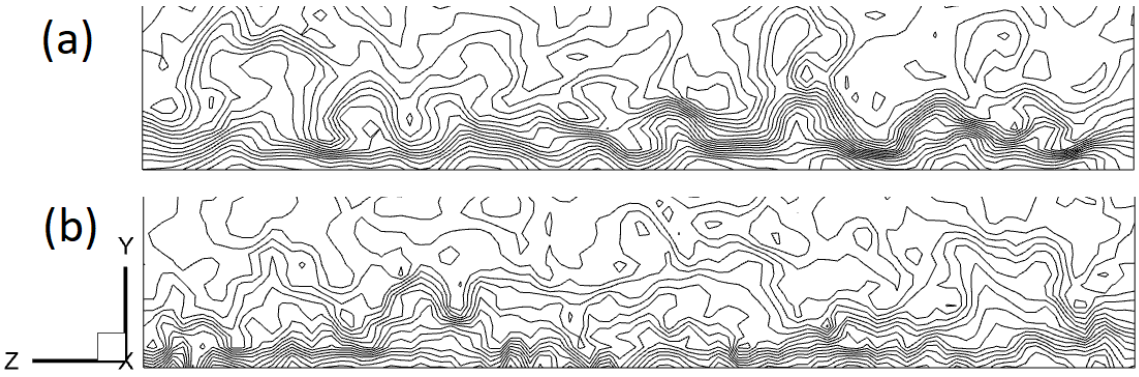

Figure 62: Iso-contours of total pressure, the (lower) modeled case appears much smoother than the (upper) base case in the near-wall region

To summarize, this subsection of field comparison indicates that: (1) confirms the approach shows more streaks and fluctuations in results, which align better with both magnitudes and distributions; (2) These fluctuations result from the presence of smaller near-wall rolling structure that was modeled; and (3) There exists a strong correlation between rolls and spanwise gradient distribution of the total pressure.

Comparisons of velocity profiles and fluctuation features

This subsection presents a quantitative comparison of averaged values, such as velocities and variances. The averaging process is based on spatial averaging, which calculates the mean value of all values on the same wall distance mesh cells. This method helps to reduce the effects of random fluctuations and provides a more accurate representation of the overall behavior of the boundary flow.

Figure 63 compares the mean velocity profiles from approaches of the wall model, control group, fine mesh LES, and the DNS. The velocities are plotted with respect to wall distances in

the plus units and displayed in both linear and logarithmic coordinates, respectively. The red line represents the DNS velocity profile, while the gray line shows the outcome of a fine mesh LES simulation. The dots or characters on each curve indicate the cell center's location from where velocities are sampled/averaged and also indicate the grid resolution. The curves in Figure 63 demonstrate that there is good agreement between the wall modeled, the control group, and reference data.

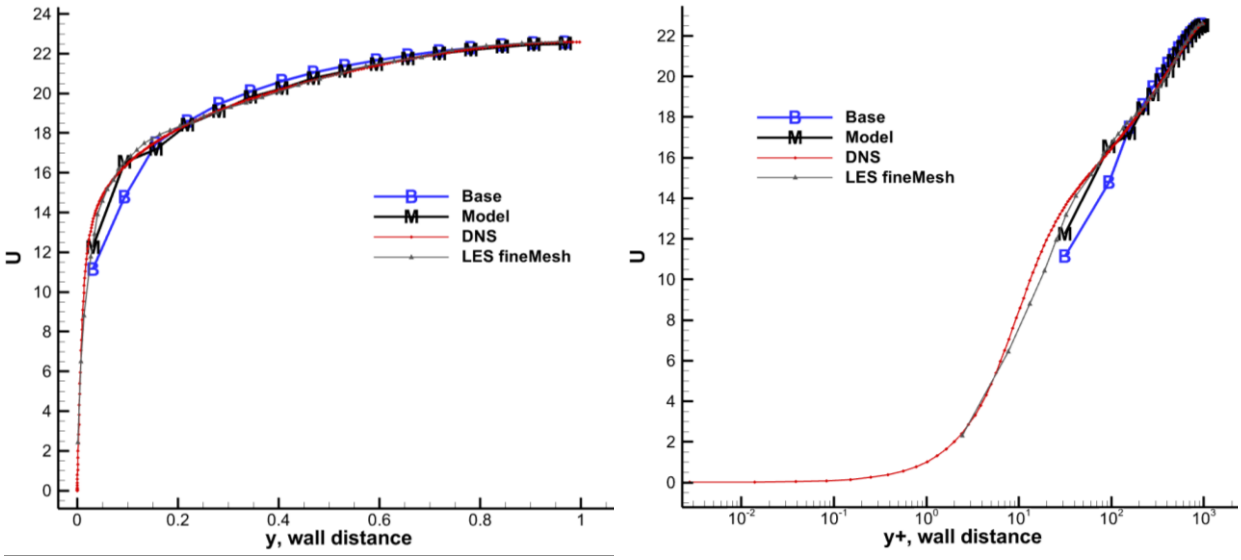

Figure 63: Mean velocity profiles, compared by the modeled and base case. The DNS and fine mesh LES profiles are presented as references.

In LES, fluctuation is a primary concern and is typically quantified using RMS (root-mean-square) velocity, TKE (turbulent kinetic energy), or Reynolds stress, since this thesis assumes a constant density for the homogeneous fluid. The Reynolds stress components for such a fluid are expressed in velocity squared, $\tau_{ij} = \overline{u_i' u_j'}$. Figure 64 compares variances, where the symbolic and curve styles remain the same as in Figure 63.

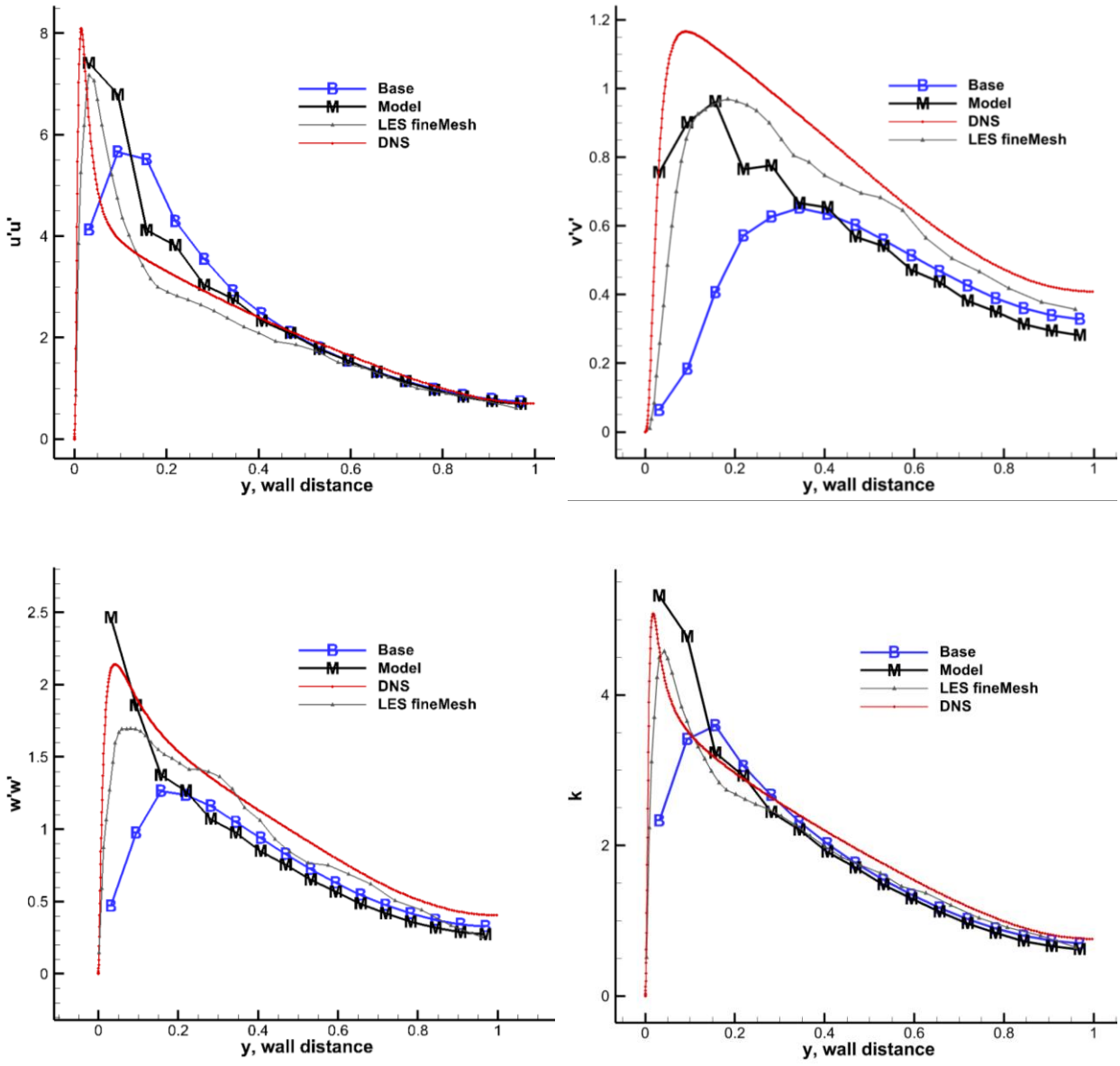

Figure 64: Variances / Reynolds stresses and kinetic energy against wall distance from the wall model, control group, fine mesh LES, and the DNS of channel flow at $\mathrm{Re}_\tau = 1,000$

All simulated Reynolds stresses follow the trend of the DNS curve. For example, as the $u'u'$ plots, all simulations capture a near-wall peak regardless of value and position, and then all values gradually drop as they approach the channel's center. This comparison shows a good

agreement among all curves when the wall distance is greater than 0.2, indicating the proposed wall model method may capture the behavior of the turbulent flow and may function as it should be at least at regions away from a certain wall distance.

The primary differences are their behaviors in the near-wall region. As per the DNS curve, which is typically considered the benchmark solution, Reynolds stress starts from zero at a wall boundary, quickly reaches a peak at approximately $y^+ \approx 10$, and then, gradually decreases as moving away from the wall. This peak is a result of the switching dominance of Reynolds and viscous stress inside the turbulence boundary layer flow. It requires enough mesh resolution to capture accurate second-order information on velocities. Hence, the fine mesh curves exhibit a slightly lower-valued peak that is shifted away from the wall. In contrast, poor results from the control group. The initial height of the wall-adjacent layer in the control group is 60, and its center is located approximately at $y^+ \approx 30$, which is much coarser than the required resolution. However, even if the accuracy is disregarded, the near-wall behaviors in the control group still make sense. Specifically, the no-slip wall conditions suppress velocity fluctuations, but after 2 or 3 cells are away from the wall the peak Reynolds stresses are reached (one of the reasons that the second-order derivative information needs such numbers of mesh points to resolute). Therefore, the coarse meshed numerical simulation still follows principles and provides results that are as “accurate” as possible, but this level of accuracy is meaningless, as it is limited by the mesh resolution.

The proposed wall model approach, on the other hand, provides a perturbed wall boundary condition that allows near-wall fluctuations to hit the desired peak value. The mesh resolution for derivative evaluation remains the same, but specifically designed data is provided to enhance the solutions. In the proposed wall model, the fluctuation is partially dependent on rolling magnitudes,

which rely on the SSP updating process that has much lower requirements for mesh resolution. This explains why the black curves of Figure 64 show a peak in the near-wall data points followed by a decrease. The lower-right subplot of Figure 64 displays the TKE profiles. The TKE is defined by $k = \frac{1}{2}\left[\overline{(u')^2} + \overline{(v')^2} + \overline{(w')^2}\right]$. In the channel flow cases, it is mainly contributed by fluctuations in the x-direction component, therefore, much similar to the $u'u'$-profile.

In summary, the proposed wall model predicts fluctuations on walls and assigns a corresponding perturbed wall boundary condition to improve the near-wall fluctuation performance of the computation. Additionally, the mean velocity profile obtained from the wall model is accurate.

Mesh convergence

As the near-wall fluctuations depend heavily on the wall model inputs, the next aspect to examine would be the mesh convergence and robustness of the proposed method. This subsection checks the performance of the wall model (with a focus on fluctuations) using different sets of meshes with specific near-wall cell heights. Three sets of meshes with cubic wall adjacent cells of dimensions 60, 75, and 100 in plus units are utilized.

Figure 65 presents the Reynolds stresses obtained from different mesh resolutions. The trends observed in the Reynolds stress curves from all mesh results agree with the DNS reference without any abrupt deviations. This indicates that the performance of the model is consistent across different mesh resolutions. Data points are gathered at the wall cells from the results of different mesh sets. There are only slight differences between the data points, which could potentially be

due to errors, as (1) curves lack smoothness and the differences have similar oscillation sizes, and (2) the deviation does not seem to be proportional to the mesh size.

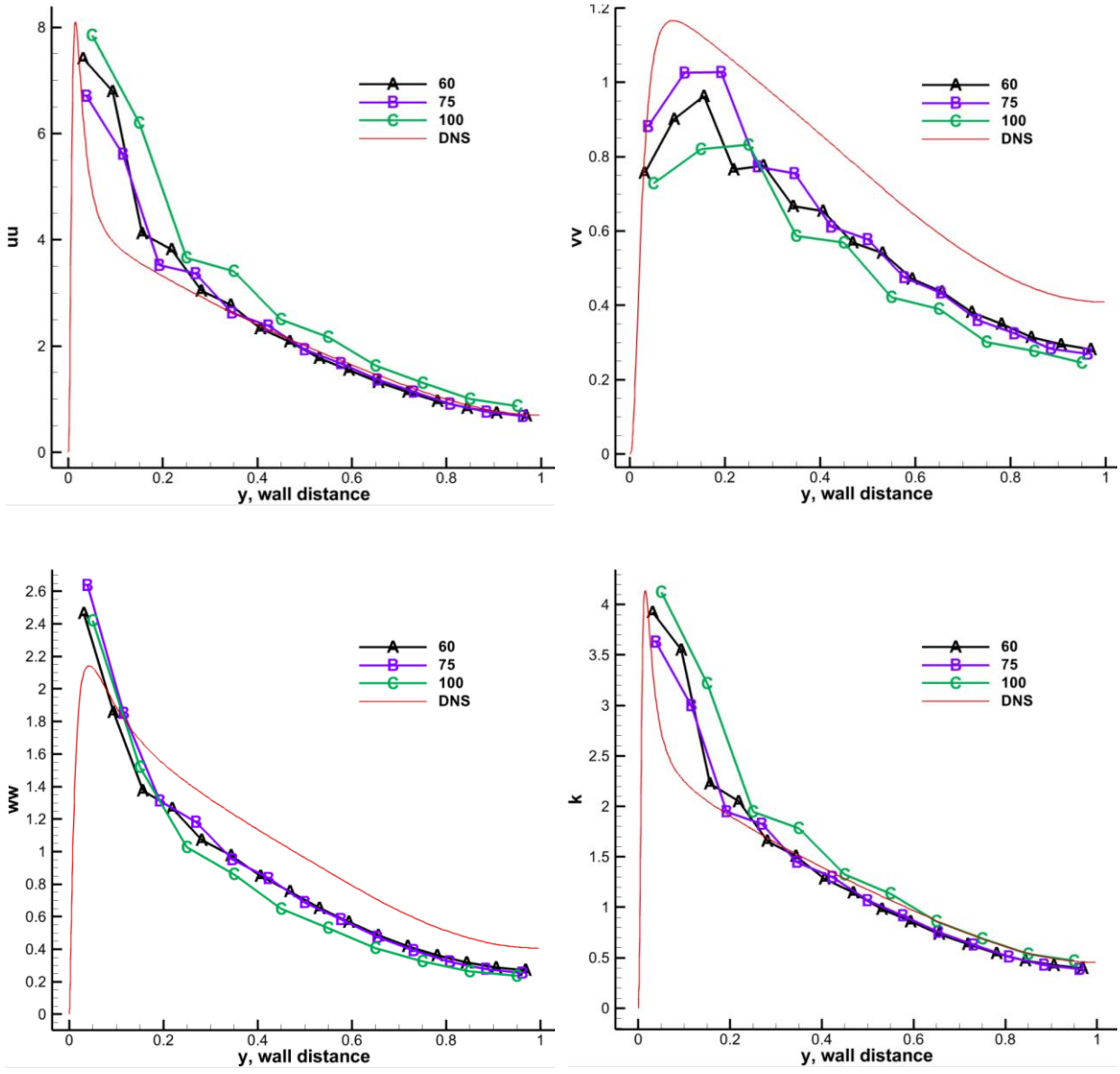

Figure 65: Variances/Reynolds stresses and kinetic energy plotting for models on different sets of grids, and the DNS reference

This thesis further examines the distributions of wall shear stresses (at the bottom wall surface) for different grid resolutions, as shown in Figure 66, where three contours are displayed. As the resolution decreases from fine to coarse mesh, the size, density of spots, as well as magnitudes of fluctuations vary. Specifically, there are fewer rolling-induced spots and weaker induced fluctuations from the top to the lower-right subplot.

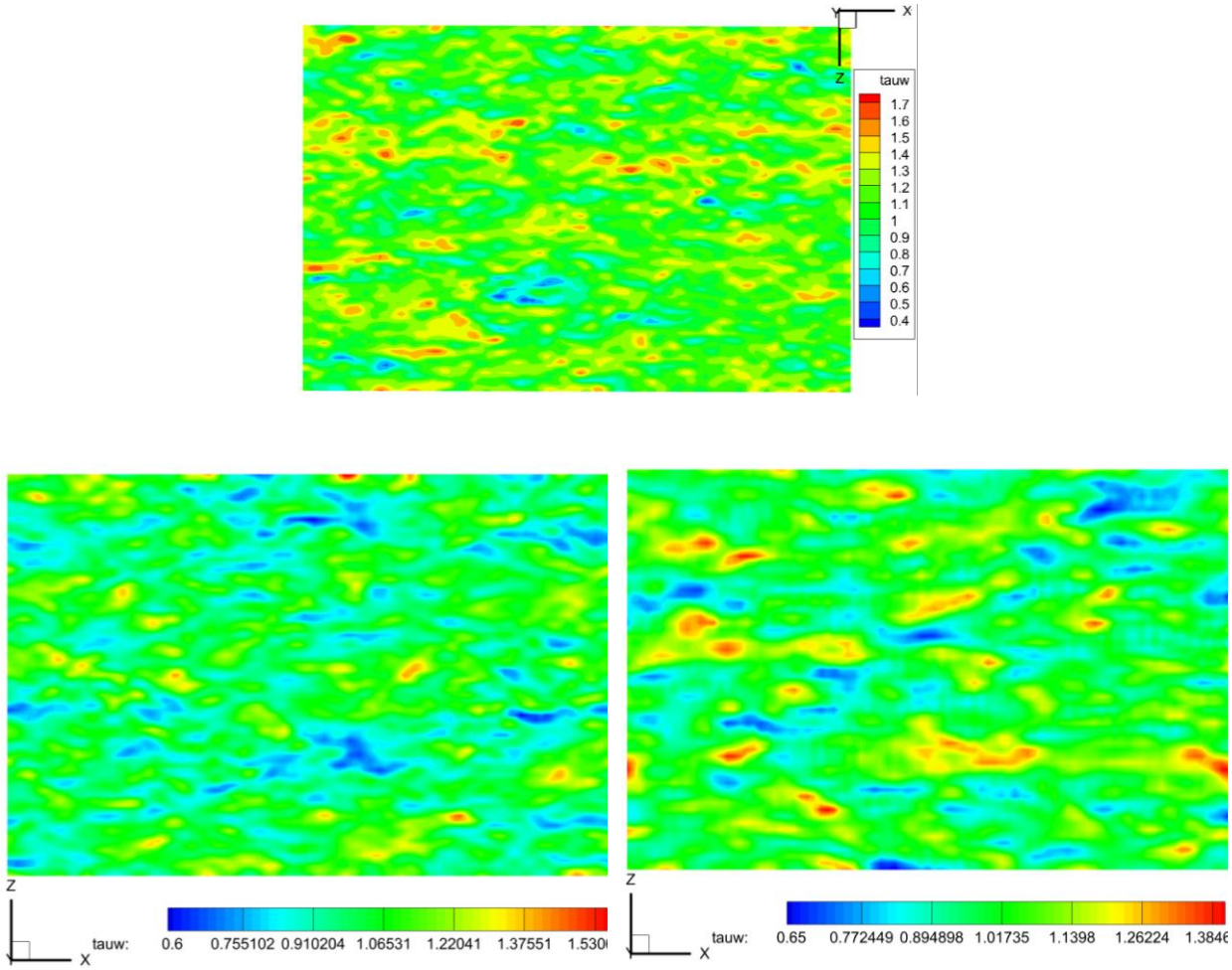

Figure 66: Distribution of wall shear stress in the streamwise components for grids 75 (left) and 100 (right), both results are from the bottom wall at t=396s

Figure 67 presents streamlines based on the velocity components in the spanwise and wall-normal directions. These streamlines are overlaid on top of velocity contours, and the mesh resolution is shown as the background grid. These plots were generated on a vertical slicing plane located at the center of the computational domain. The results show that the fine mesh provides a great number of smaller near-wall rolls, as expected.

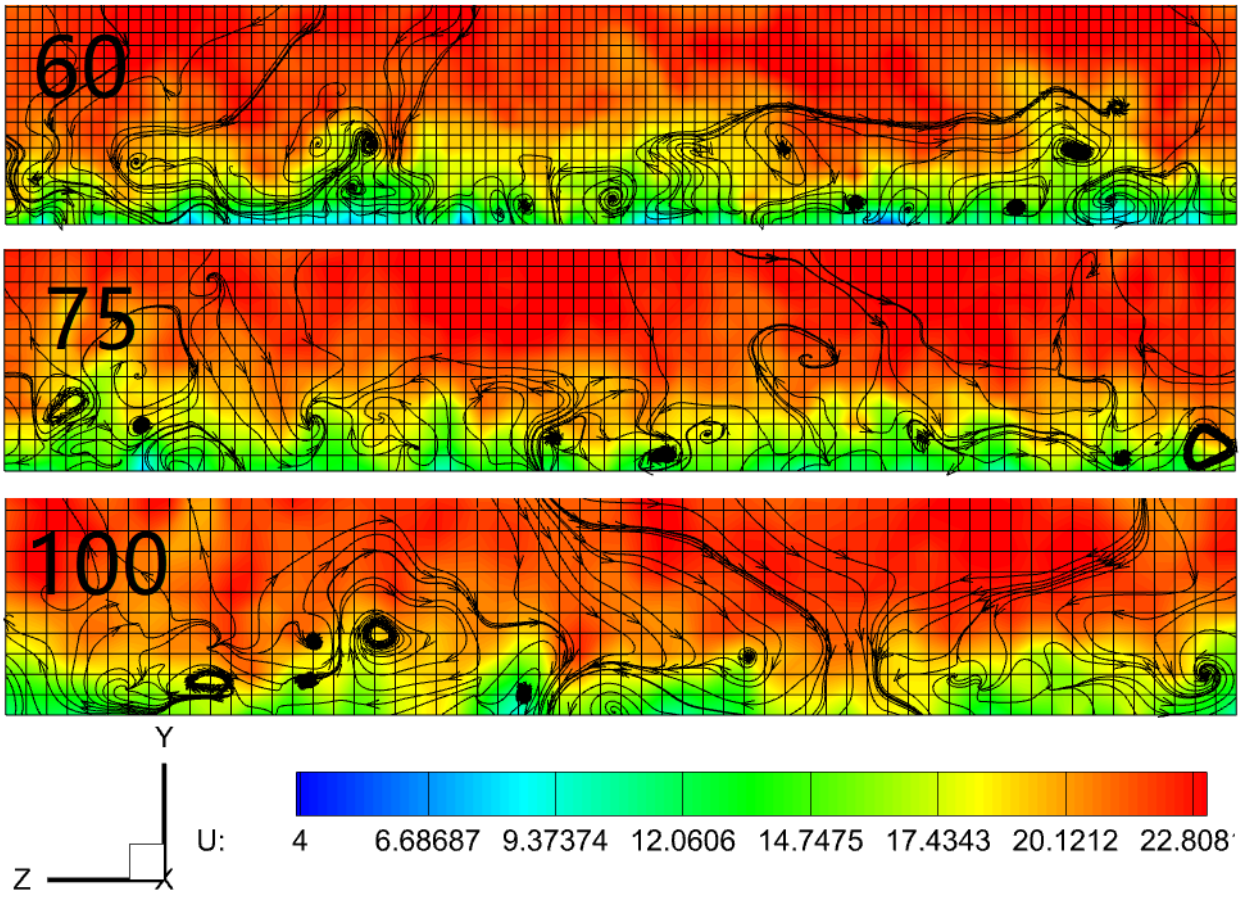

Figure 67: Velocity contour and streamlines for near-wall rolls. All plots are based on vertical slicing at x=4.5 (center of fields). Computational meshes on the background to indicate resolutions

Highlights

The proposed wall model approach has several features:

(1) Modeled near-wall fluctuations at a large wall-normal grid spacing without embedded mesh.

It was previously mentioned in fluctuation profiles that having enough wall-normal resolution is important to resolve peak fluctuations at approximately $y^+ \approx 10$. However, for a wall-modeled approach, the height of wall adjacent cells is usually much larger than 10, which makes it difficult to evaluate local fluctuations accurately. Facts such as mesh smoothing, near-wall damping, and model accuracy may introduce errors.

"Creating a thin layer sub-mesh at near-wall region" is a commonly used approach to overcome the lack of wall-normal resolutions. Therefore, this subsection compares the results from two other approaches with the proposed wall model. Figure 68 shows a comparison of RMS velocities.

The dashed blue curves represent the result from Iyer and Malik 2020 [113], where high-fidelity simulation methodologies were applied to multiple practical cases, including the channel flow at $\mathrm{Re}_\tau = 2,000$. An equilibrium wall model proposed by Kawai and Larsson 2012 [69] was used in an overlapping layer between $y = 0$ and $y = h_{wm}$, where the inner layer was modeled by solving an ODE, $\frac{d}{dy}\left[\left(\mu + \mu_{t,wm}\right)\frac{dU_{\parallel}}{dy}\right] = 0$. The $U_{\parallel}$ is the velocity projected on a wall-parallel plane, and the wall model eddy viscosity is taken from the mixing length formula

$$\mu_{t,wm} = \kappa \rho y \sqrt{\frac{\tau_w}{\rho}} \left[1 - \exp\left(-y^+ / A^+ \right) \right]^2 \tag{5.11}$$

16 mesh points are deployed along half the channel height (as the boundary layer thickness), and the location of the first grid point from the wall is assigned as the exchange location.

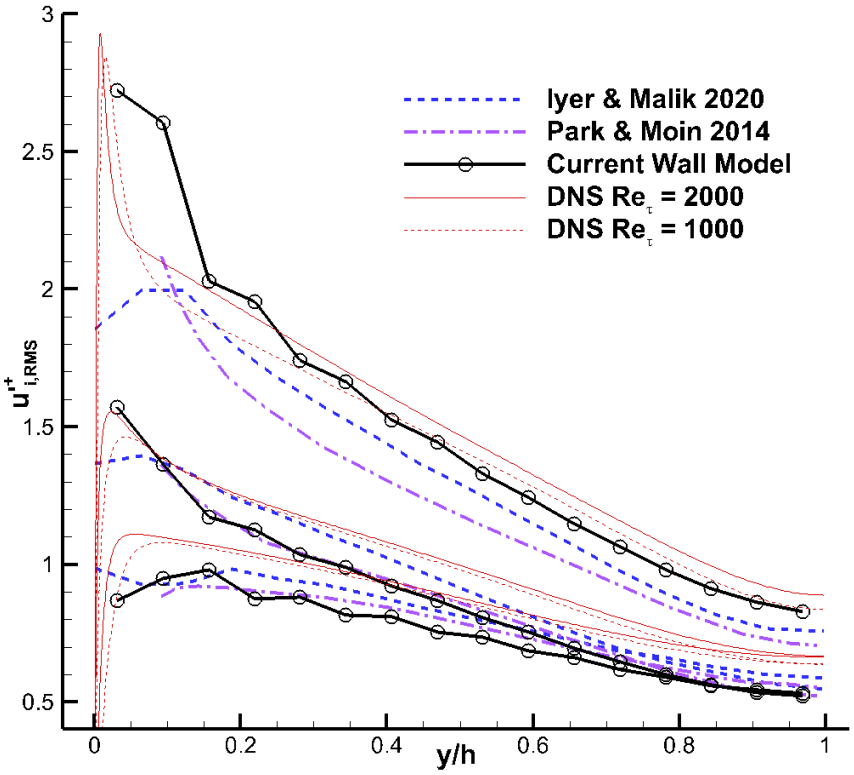

Figure 68: RMS velocities

The dash-doted magenta curves in Figure 68 correspond to results obtained by Park and Moin 2014 [49], In that study, a non-equilibrium wall model based on a dynamic eddy viscosity model was applied to an unstructured solver. The wall model zone was wrapped by a structural overlapping mesh under 200 plus units, as shown in Figure 69. This approach found a suitable value for the eddy viscosity $\mu_{t,wm}$ by requiring the conventional RANS-type model to dictate the

total Reynolds stress without reference to the LES subgrid-scale viscosity. All adjustments were dynamic, meaning that the coefficients were determined solely from the wall-model solution.

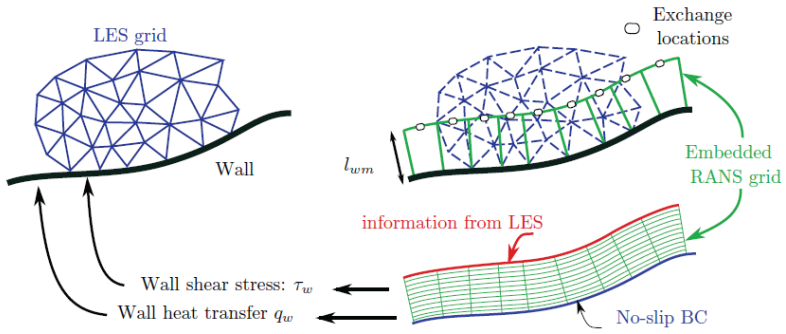

Figure 69: Sketch of the wall-modeling procedure. From Fig. 1 [49]. Copyright 2011 Dr. Julien Bodart [114]

The following are some comments on the comparison of the results presented in Figure 68. In the u'_{RMS} curves, the method behind the blue dashed curve in the figure attempted to decrease the near-wall eddy viscosity using the damping expression (5.11), but this damping approach leans on an empirical formula to reduce the coefficient regardless of the local rapid increase in streamwise fluctuations. Therefore, despite using a wall-normal refined grid and an ODE, the blue dashed curve was still over-damp and failed to capture both the value and location of the peak. The magenta dash-dotted curve did not display the embedded portion (the curve was cut off below the matching point, $y^+ = 200$, check [115] for that portion), but it was able to capture the trend of near-wall increase. This is because the RANS-type model was used in the embedded layer to dictate Reynolds stress rather than relying on the subgrid-scale viscosity. However, relying too heavily on the Reynolds stress to dictate the damping effects can lead to a global overestimation of these effects, resulting in the rest of the curve having values below the actual ones. Both

references from papers are simulated on $\mathrm{Re}_\tau = 2000$, while the proposed wall model in this thesis is on $\mathrm{Re}_\tau = 1000$, due to computational cost reasons. However, DNS curves from $\mathrm{Re}_\tau = 1000$ and $\mathrm{Re}_\tau = 2000$. provided in Figure 68 are similar to each other.

The proposed wall model shows good performance on the u'_{RMS} curve by capturing the peak and following the remainder of the DNS curve. There are two disadvantages: (1) The curve exhibits oscillations, particularly in the area near the walls; and (2) The v'_{RMS} and w'_{RMS} curves are slightly lower compared to those from DNS.

(2) Low computational cost.

Table 5 presents the computational cost for six cases, comparing both the model and control group, based on three sets of meshes used in the convergence tests. The additional computational costs over the control groups range from approximately 3 to 8 percent, making the proposed wall model relatively cost-effective.

Case & Mesh	Computational cost (wall clock) in seconds per 100 seconds of channel flow simulation (s)	Difference from Model to Base in seconds (s)	Difference in percentages
A model case, 60	412,376	12,011	3.13 %
Control group, 60	400,365		
Model case, 75	205,664	9,156	4.66%
Control group, 75	196,508		

Model case, 100	45,426	3,437	8.19%
Control group, 100	41,989		

Table 5: Computational time, the additional model cost in percentages

The computation times in seconds mentioned above were obtained from the log files of wall clock time. To ensure fairness in comparison, a single thread (non-parallel) was assigned to each case on cores of Intel i5-3470 3.2 GHz CPU.

Mesh Description	Half channel cells' distribution in x, y, and z	Total number of cells	Number of wall cells	Wall cell percentages
60	150, 16, 100	480,000	30,000	6.25%
75	120, 13, 80	249,600	19,200	7.69%
100	90, 10, 60	108,000	10,800	10%

Table 6: Mesh descriptions

This thesis assumes that the ratio of wall cells to total mesh cells affects the percentage of extra cost. A lower ratio of wall cells results in a smaller increase in computational cost, which is favorable for practical applications where a low percentage of wall cells is typically the case.

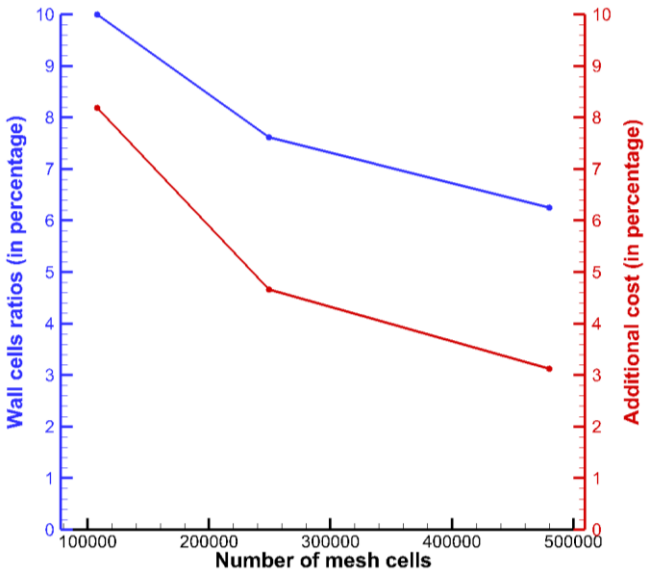

Figure 70: Additional computational costs, wall cell ratios vs. number of mesh cells

The changes in the additional computational cost of the proposed wall model can be seen graphically in Figure 70, represented by the red curve and right axis. As the mesh is refined, the percentage of wall cells decreases, resulting in a decrease in the additional cost of the wall model.

Secondly, the additional cost for wall treatment increases approximately linearly wrt. the total mesh size. This is also favorable as the wall model only affects wall-adjacent cells and does not require additional meshes. Furthermore, this wall treatment can be easily parallelized.

(3) Avoid the reduction of fluctuations when reducing the resolution in the spanwise direction

In the proposed wall model, near-wall fluctuations primarily rely on rolls, which are the output of the SSP process that relies heavily on a mean shear from the streamwise velocity profile. Therefore, accurate modeling of this streamwise velocity profile leads to precise determination of rolling magnitudes. This approach diverges from existing wall models, which typically rely on a

simplified RANS solver and a refined near-wall mesh. However, most of the embedded mesh only addresses the resolution in the wall-normal direction, resulting in a wall-parallel resolution that is too coarse to capture rolling structures.

Theoretically, the rolling magnitude in the proposed wall model is independent of the spanwise mesh resolution, but in practice, the discretization of mesh points along the spanwise direction is necessary for carrying out LES computations. The accuracy of the LES solutions, specifically the near-wall velocities, is critical for maintaining the wall model's integrity.

Comparisons of the wall shear stress are shown in Figure 71. The top two figures (identical to Figure 57) display results on a mesh with 60 spanwise intervals. Meanwhile, the bottom two figures are from another set of meshes with 200 grid point intervals in the spanwise direction. The same contour levels are applied to display stresses ranging from 0.4 to 1.7.

Upon visual inspection, the left two figures from the control group exhibit considerable smoothing, meanwhile, between the two control group cases, the deep blue and orange spots are no longer present for the $z^+ = 200$ case. However, the full-color preservation in the right two figures, regardless of the mesh resolutions. In conclusion, the proposed wall model not only offers a broader range of wall shear stresses but also better preserves such a range, even with deliberately sparse spacing designed mesh.

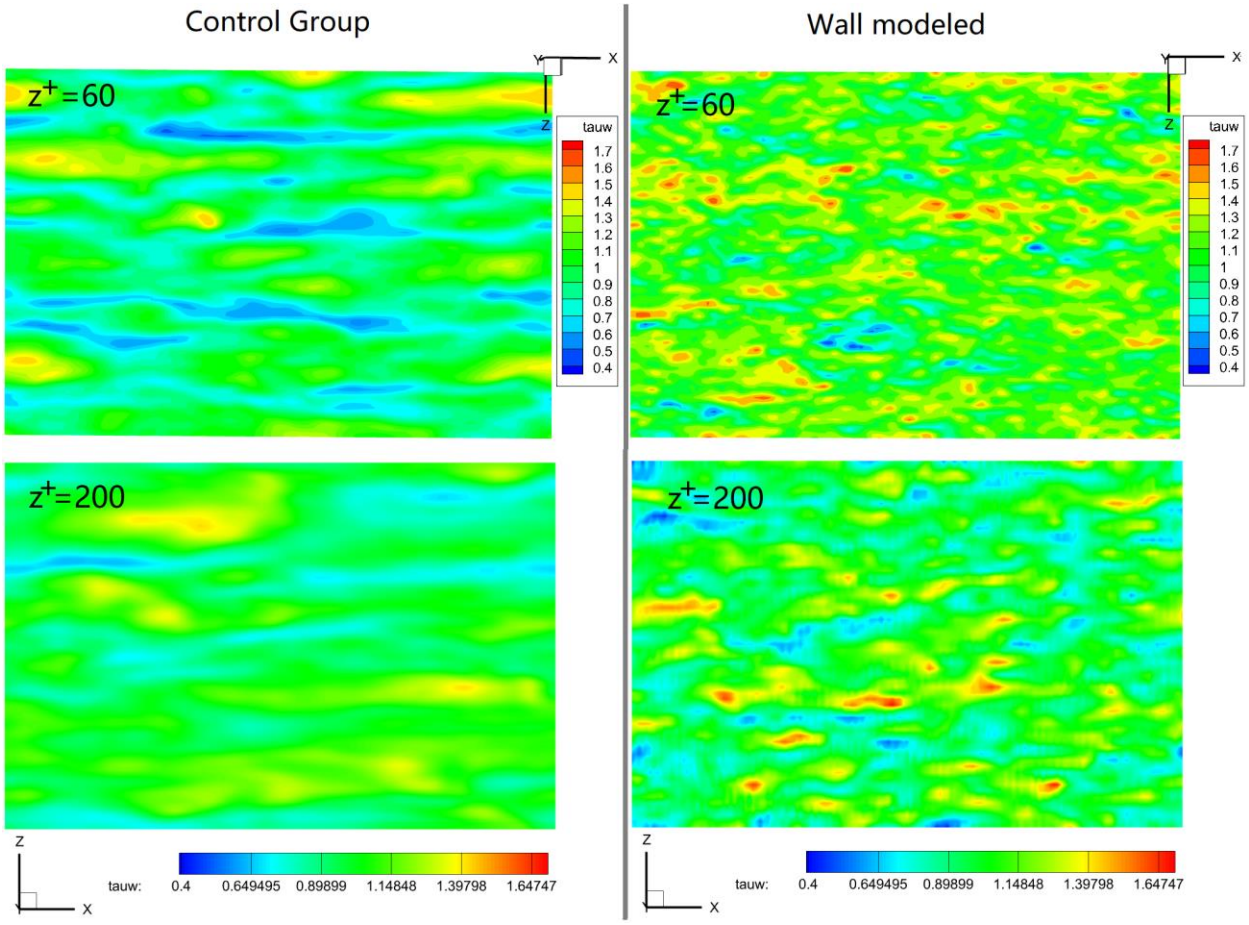

Figure 71: Comparing contours of wall shear stress in a large spanwise interval mesh (dimensions of wall cells are 50, 50, and 200 in x, y, and z directions).

Figure 72 compares velocity fluctuations quantitatively using TKE. The curves are divided into two groups: blue for the control group and black for the wall-modeled case. Within each group, dashed curves show results of cubic wall cells, while solid curves are from the stretched mesh. Overall, all curves match the DNS red curve well in the outer region of the boundary layer.

($y^+ > 200$ or $y > 0.2$), and two dashed curves of cubic cell results are slightly closer to the DNS than curves from stretched wall cells.

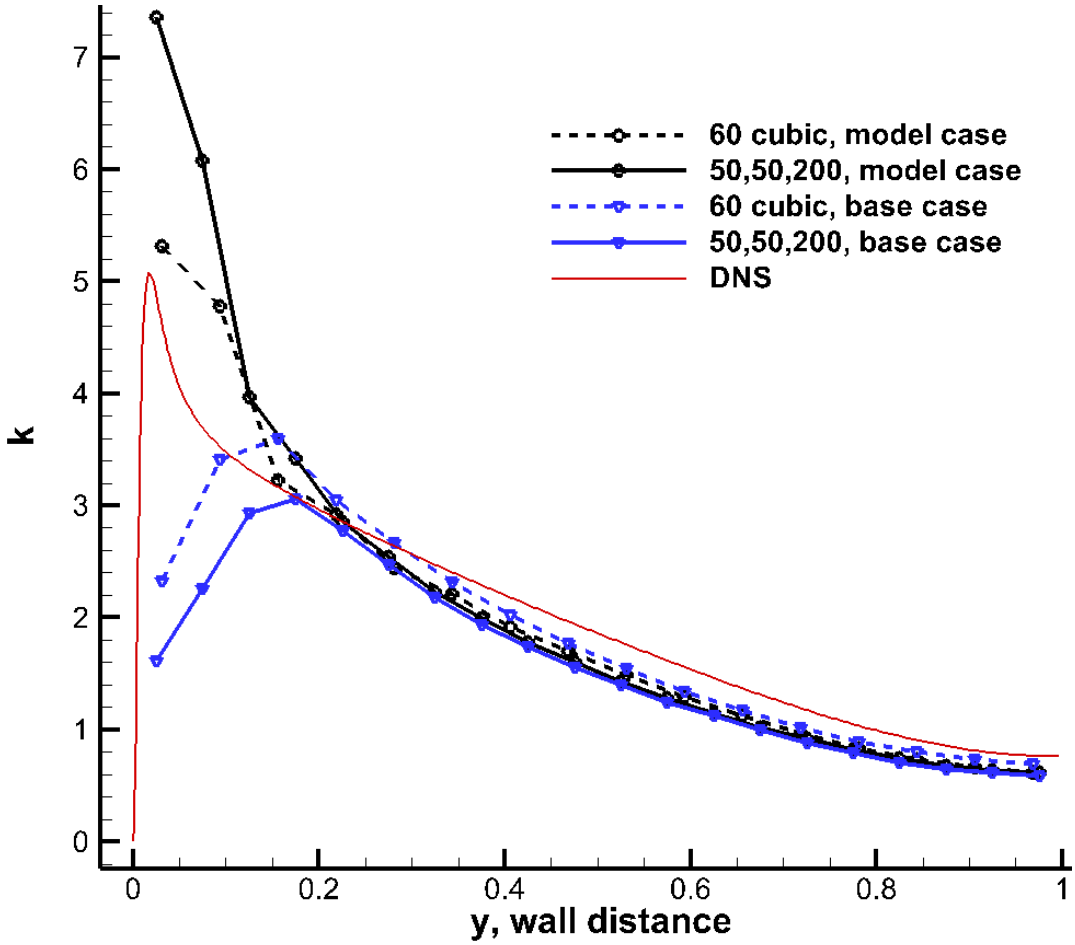

Figure 72: Comparing the turbulent kinetic energy

Two blue curves from the control group underestimate wall fluctuations, and this error becomes more significant in the stretched mesh. Conversely, the two black curves from the wall model cases show the opposite trend, with the solid curve for stretched results overestimating TKE in the near-wall region. The differences in behavior observed may be due to the treatment of the nodal distribution of wall shear stress.

Generally, the current procedure of assigning nodal fluctuations in Section 4.2.5 results in higher fluctuations for nodes crossing a larger spacing along the spanwise distance. Sketch in Figure 73 shows a stretched cell that causes the geo-distance projection of nodal S2 and S3 to shift more sideways, leading to a greater distributed fluctuation as explained in the mapping shown on the right side of Figure 73.

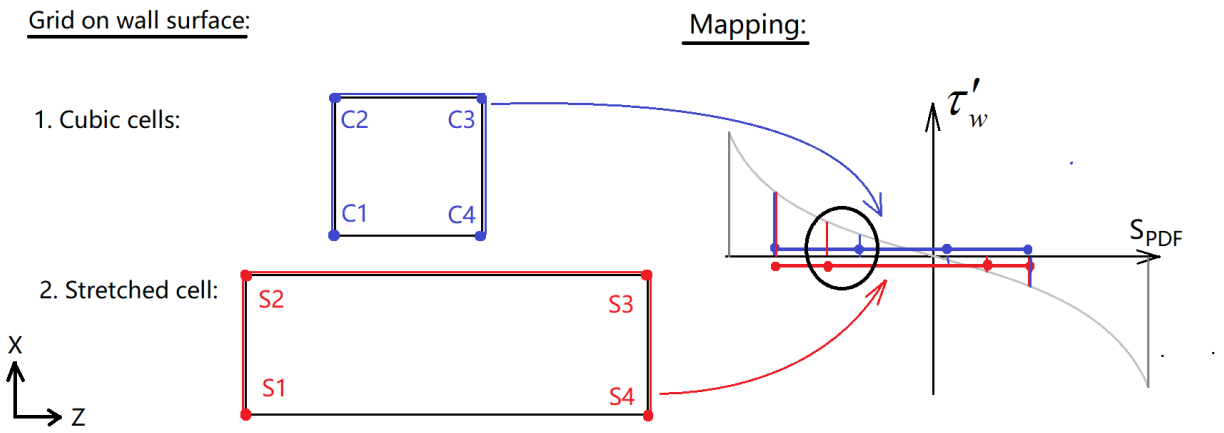

Figure 73: Sketch of difference in fluctuation assignments due to the spanwise mesh resolution

In summary, this subsection emphasized the advantages of the proposed wall model, which include its capacity of (1) using only the existing mesh, (2) high computational efficiency, and (3) working with a rough spanwise resolution.

Discussions

This subsection will provide possible improvements that were based on issues of the current wall model.

(1) General thinking toward an LES wall model

A RANS wall model only presents near-wall time averaging features, but an LES wall model should be: (1) Transient to capture fluctuations; (2) account for both viscosity and Reynolds stress; and (3) Driven by the outer flow. Traditionally in LES, a subgrid-scale model is used in the simulation to capture the effects of small turbulent scales that are unresolved in the near-wall region. In some cases, a wall model may be combined with the subgrid-scale model to provide a more accurate prediction. The accurate prediction in this context refers to correctly accounting for the effects of small turbulent scales or wall irregularities, which can be indicated by the Reynolds stresses or turbulent viscosities. Figure 2 shows the features of the physical boundary flow property, and it suggests that there is a switch in the dominance of viscous and Reynolds stress under $y^+ \sim 50$. Therefore, the turbulent viscosity, which supplements the unresolved portion of the Reynolds stress, shall be lower than the molecular viscosity.

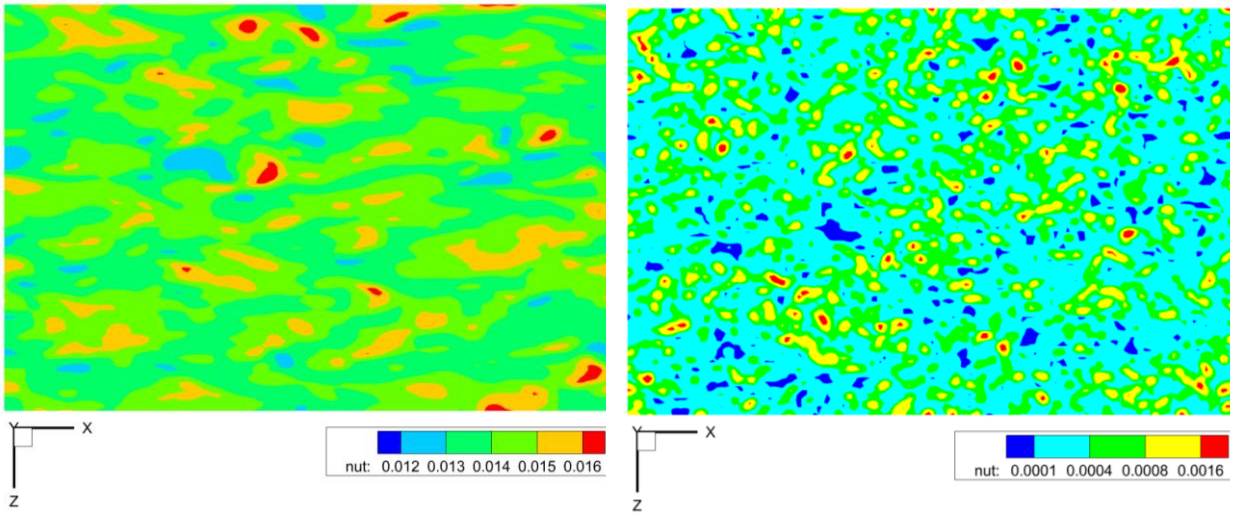

Figure 74: Turbulent viscosity distribution. Left: base case, averaging 0.014, ranging [0.012, 0.017]; Right: model case, averaging 4.2e-4, ranging [1.3e-5, 0.003]

Figure 74 provides a further comparison of turbulent viscosity for both the control group and the wall modeled case, with near-wall layer height $y^+ = 60$, and a molecular viscosity. This comparison shows that the turbulent viscosity values in the modeled case are significantly lower. The majority of the color bands are light blue and green, and they average 0.0004, which is approximately 40% of the molecular value. Lower turbulent viscosity means greater resolved Reynolds stress, which is confirmed in Figure 64.

(2) Implementation of the wall model is driven by the outer flow

To implement the concept that near-wall structures are driven by the outer flow, this thesis proposes a switch mechanism that employs the local gradient of total pressure to direct the impact of fluctuations toward the LES fields. Figure 20 illustrates the statistical correlation between gradients and the core vorticity of rolls. The expression (4.20) is used to introduce fluctuations by comparing local differences to a threshold value of total pressure gradients. This mechanism is based on the assumption that the maximum vorticity and maximum gradient co-occur.

Further clarification is needed in two aspects: (1) The spatial correlation between the maximum vorticity and maximum gradient; and (2) The conceptual explanation for this trigger mechanism.

Firstly, examining the proximity of the maximum vorticity and maximum gradient can help determine their correlation. When these two points are closer together, there is a higher probability of a relationship between them. Figure 75 analyzes all pairs of $\left|\Omega_{\max}\right|$ and $\left|\max\left(dp_0/dz\right)\right|$ from Chapter 3 to test this hypothesis. The horizontal axis shows the distance between each pair of spots, and the vertical axis represents the probability density. Referring to Figure 75, it can be observed

that the majority of pairs have distances of less than 30 wall units, which is typically smaller than the local mesh size. The local mesh size is usually several dozen units along the wall-normal direction and significantly larger along the wall parallels. Therefore, it appears reasonable to utilize local gradients for the switching mechanism mentioned above.

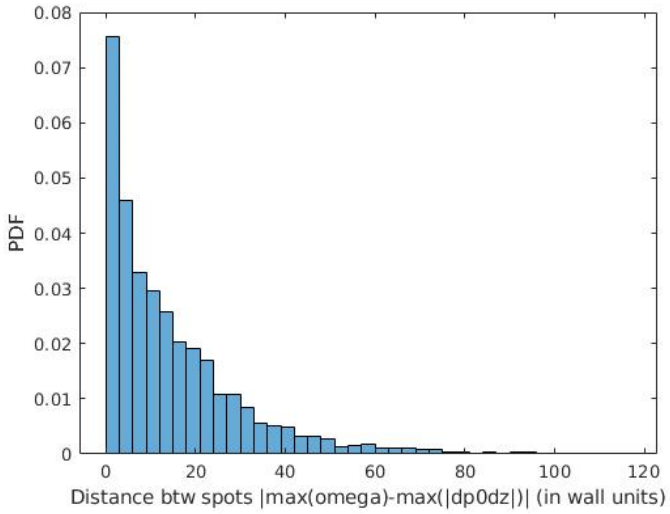

Figure 75: The probability density function (PDF) of the proximity between the locations of maximum vorticity and the maximum gradient of total pressure.

Secondly, a conceptual explanation for this trigger mechanism: Generally, this mechanism sets up a proper (reduced) frequency of rolling structures that are assumed inside local meshes. The amplitude of fluctuations on a coarse resolution is expected to be lower than their actual values due to spatial averaging effects, which lead to a loss of spatial resolution and a smoothing out of fluctuations. However, spatial averaging has a less significant effect on the frequencies of low-frequency fluctuations (Low-frequency fluctuations, having longer wavelengths, are less susceptible to the low-pass filtering effect of spatial averaging. The spectral analysis also shows that the filtering process tends to cut out high-frequency content.) On the other hand, the energy

of oscillation (suppose a sine wave) is proportional to the square of the amplitude and linear to the frequency. Therefore, artificially increasing the amplitude generally requires a decrease in its frequency. This is why a trigger mechanism was introduced to reduce the frequency of fluctuations.

(3) About the total pressure gradient

A spot of high total pressure represents a greater potential for the local fluid energy to be converted into work through different mechanisms, such as kinetic energy or viscous dissipation. For example, a static inlet flow out of a compressor gains high potential energy which is capable of converting into kinetic energy. Similarly, high potential total pressure flow dissipates its energy when it approaches walls due to viscous frictional forces. This process converts partial mechanical energy into thermal energy and creates structures (rolls and corresponding streaks with fluctuating streamwise velocities) that contain regenerated kinetic energy. These rolling structures are expected to be temporary as they do not persist in field averaging. Additionally, they are likely to appear with fluctuations in total pressure along the spanwise direction, as the rolls dissipate more energy through viscous friction. Therefore, tracing the total pressure gradient could be a good alternative to directly resolving such rolls in a coarse computational mesh. Based on such an assumption, this thesis claims a relationship between the total pressure gradient and local rolls. Intuitively, rolls are present in areas where the spanwise gradient is significant, and they eliminate this gradient to smooth the distribution of total pressure along the spanwise direction.

(4) Accuracy of the fluctuations (, or this wall modeling approach)

The precision of this wall model relies on multiple factors, including (1) the ability to predict magnitudes of wall shear stress fluctuations, (2) the underlying assumptions regarding the PDF-based distribution of perturbations, etc.

For the magnitudes, the rolling amplitude output is converted to the magnitude of fluctuating wall shear stress using Expression (4.9). This expression relies on the relationship (4.8) between statistical roll and shear stress data obtained from the DNS channel flow, which is applicable for non-pressure gradient plate flow. To ensure the best simulation of the rolling mechanism and avoid laminar boundary flow, it is suggested that the cell height should be no less than 50 wall units. Additionally, most rolling structures commonly have less than 120 wall units, so it is recommended to keep the cell height below 120.

Perturbations are assigned to each vertex based on their mapped distribution on the temporal PDF profile. The original vertices are connected in a sequence of increasing in the spanwise direction. The PDF profile utilized is under the assumption that the temporal average of the perturbation is the same as the spatial average within a wall cell. It is possible because the wall cell is large enough and has RANS-like fluid performance. The process generates fluctuations in the rolling orientations, resulting in fluctuations that mimic the characteristics of a rolling structure with higher perturbations at the outer edges and more calmness towards the center. This approach is effective and reliable. However, in grids that have a high aspect ratio, there is a noticeable mesh dependence on the fluctuations in vertices, which should be taken into consideration.

Last but not least, the assumption of incompressible flow is applied, and both the derivation process of SSP and the DNS raw data are carried out under no-pressure gradient conditions.

(5) Kinetic energy of rolls

Energy in fluctuations is proportional to the square of amplitude and the frequency. In this thesis, amplitudes are evaluated primarily by the SSP updating process, and the frequency is determined by the trigger mechanism from indicators of a local total pressure gradient. This treatment replicates the behavior of inner layer structures that are driven by external flows but fails to consider energy interaction between rolling structures of varying sizes in a turbulent flow. The noticeable oscillations from the near-wall locations in Figure 64 (5 points close to a wall) serve as evidence of neglecting such a connection.

Generally, energy is constantly transferred from larger scales of motion to smaller scales through a process called the energy cascade. More kinetic energy stored in larger scales of motion (vortices and eddies) interacts with each other, leading to a transfer of energy to smaller scales of motion. As the energy is transferred, the fluid becomes more disordered and turbulent. Successive interactions between smaller vortices and eddies generated by this energy cascade lead to further energy transfer to even smaller scales. The -5/3 spectral law is commonly used to describe the energy cascade, which explains that energy is distributed across scales according to a power law with an exponent of -5/3. This power law indicates that the energy of the turbulent flow is concentrated at large scales and gradually dissipates at smaller scales.

The behavior of rolls in wall-bounded flows may differ from that of free flows, as the presence of walls can constrain their motion as they approach. In Figure 76, the energy spectrum curves are shown, where the red curve represents the spectrum of a DNS near-wall flow, the blue one is from the average performance of rolling structures, and the black line denotes the -5/3 spectral law. This blue averaging curve is obtained from spectrums of rolls in each extracted

bounding box from section 3.2.2. Those spectrums are plotted individually on the left of Figure 77, and grouped and averaged in the right figure based on their dimensions.

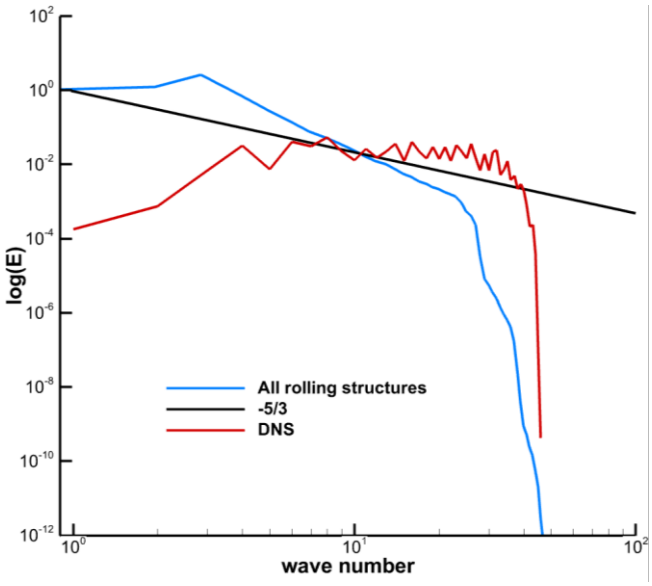

Figure 76: Energy spectrum of a DNS near-wall flow in red, rolls averaging in blue, and -5/3 in black

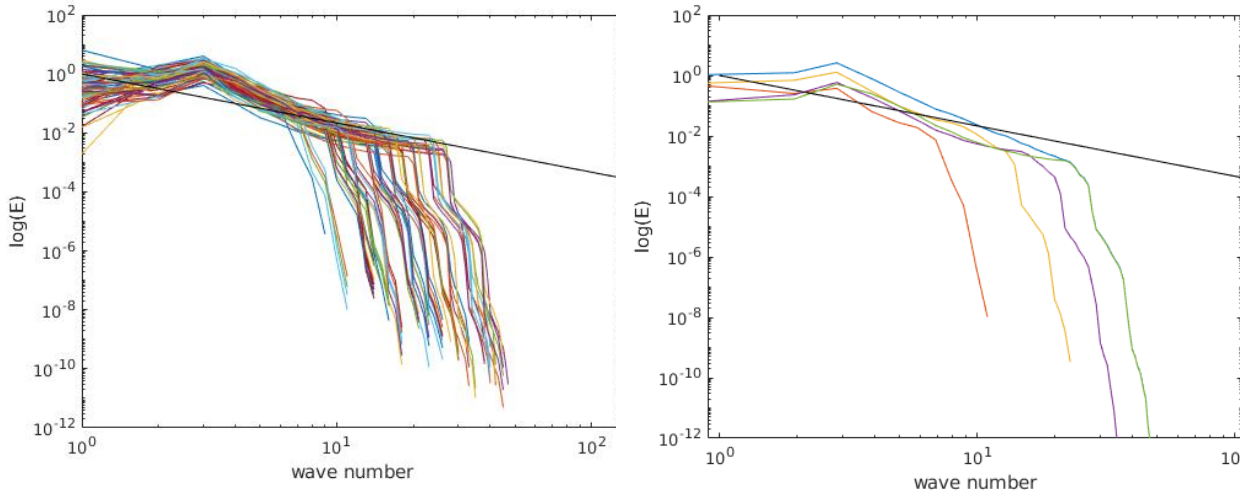

Figure 77: Energy spectrum (Left) for each sampled rolling structure, and (Right) for averaged of rolls in groups of sizing 0-20, 20-40, 40-80, 80-100

These spectrum curves contain sections that appear as flat-slope within the middle ranges of wave numbers. These sections indicate that the distribution of energy among various sizes of structures (rolls) follows a power law. Meaning, inside a bounding box that surrounds a local maximum core vorticity, there should be multiple different sizes of structures that carry kinetic energy following a power law distribution. Compared with the -5/3 slope, these indicate stronger dissipation in smaller rolls, which makes sense, as the viscosity contributes more when approaching a wall.

5.3 Summary

This chapter presents implementations and testing of the wall model. The model involves updating rolling magnitudes using SSP and converting them to fluctuating wall shear stresses, which are then assigned as boundary conditions to the LES.

The model's performance was evaluated through test studies conducted in both isolated rolling and LES-coupled cases. The isolated case confirmed that the model performed as intended, and the LES-coupled test verified its compliance with mass and momentum conservations by checking a force balance on the bottom wall. The mean velocity profile and midfield velocity contours were compared with both the control group and the DNS results. Fluctuation features in the form of Reynolds stress and TKE were also compared, and several observations confirm the model's ability to improve results. These include the presence of more streaks as fluctuating details on walls, more small near-wall rolling structures in the velocity field, and higher near-wall Reynolds stresses that are closer to DNS profiles.

Chapter 6 Future work and conclusions

6.1 Conclusion

The thesis presented a wall model for simulating fluctuations in LES. It allows the use of coarse wall-adjacent grids, while still being able to model effects from near-wall rolling structures, thus improving boundary conditions. This approach is achieved with promising results and saves a significant computational cost.

A principle idea behind this model is the outer flow modulation in a boundary layer, which means that the large-scale structures in the outer region of the boundary layer affect the smaller-scale features in the inner near-wall layers. This thesis assumes that the large-scale structures are elongated streamwise vortices (rolls) that exchange low-speed lower fluid with high-speed higher fluid (away from a wall), causing changes in the velocity field and leading to fluctuating wall shear stress. To model these rolling effects independently of the LES solver, this thesis uses a self-sustaining process and statistical relationships abstracted from a DNS flow.

In greater detail, this wall model utilizes explicit updating dynamical equations to track and evaluate the magnitudes of rolls. Moreover, algebraic expressions are utilized to convert the rolling into fluctuating wall shear stress. Such algebraic expressions are from studying rolls' behavior and their influence on the DNS flow. By integrating these techniques, this wall model achieves reasonable simulations of fluctuations in a boundary layer without requiring a local mesh refinement. The use of larger wall-adjacent cells offers several benefits, including simplifying the pre-treatment process, reducing the global mesh size, and enabling greater stability when using larger time steps in the LES.

The performances of this wall model in an LES wall-bounded flow were demonstrated through a channel flow test case. A comparison between the results from the wall model and a control group highlighted improvements in near-wall velocity, total pressure, Reynolds stress components, and TKE. These improvements were confirmed by observing cross-validation, and certain profiles, such as those of Reynolds stress and TKE, much closer to the curves from DNS were found. Additionally, this thesis verified that the intermediate values changed as intended to ensure the model functions as designed. Since there are statistical relationships applied, partial intermediate values were also compared with the DNS data, which includes rolling magnitudes and effects of fluctuating magnitudes on walls. Subsequently, the mesh convergence test demonstrated that fluctuations at the walls were effectively maintained across various near-wall mesh sizes. Although the large spanwise spacing mesh test ended up with higher fluctuations on walls, these results were reasonable and can be explained.

Statistical relationships in this wall model were extracted based on rolling samples from the DNS field data. These relationships are (1) the correlation between core vorticity and fluctuating wall shear stress magnitudes, and (2) core vorticity and the peak of total pressure gradient at various mesh resolutions. They were employed to reduce computational expenses and simulate a more practical flow. The bounding box search process was used to extract rolling samples, and the parameter in this process was carefully selected and verified. Although the samples were scattered due to turbulence, and the coefficient of determinants did not reach the expected high levels, the resulting fitted curves are still reasonable and provide a representation of the general relationships between variables.

6.2 Future work

Currently, there are simplifications in the implementations of the wall model. For example, the model only considers neighboring cells on the left and right while searching and averaging variables along the spanwise direction, instead of computing gradients and interpolating values from possible neighbors. Consequently, this limits the model to cases with streamflow along the x-direction of coordinates and on hexagonal grids only. These simplifications require revision. Furthermore, the model can only handle one face of a wall cell as a wall boundary, whereas in practical applications, a single wall cell may have two faces (edges) or even three faces (corners) that require wall boundary conditions. In such scenarios, the SSP updating procedure and the processing sequence for each face need to be revised.

Additionally, there are several improvements in the modeling and processing as follows:

(1) The fluctuation assigning process in section 4.2.5 relies on distance projections mapping of each vertex may lead to significant mesh-related solutions, particularly in drastic changes of aspect ratios as demonstrated in the test case in section 5.2.3.

(2) There is potential for further exploration of the switching mechanism in 4.3.2, as the current approach only utilizes the spanwise derivative of total pressure. More validity tests and experimentation with complex forms could be conducted by incorporating complicated components to enhance the switching mechanism.

(3) The current introduction of fluctuating wall shear stress is accompanied by pre-set expressions and switching conditions, which is an open-loop system. It works with simple flow cases, such as a channel flow where no complicated interactions happen, but a lot of statistical data

can be leaned on. Under this case, no energy constraints or feedback mechanisms are needed to adjust fluctuations from backward. As a result, this wall model works for only flat plate flow scenarios.

(4) Possible kinetic energy constraints of introduced fluctuation can be applied to the current wall model. The idea is to find the proper energy for a local size of rolling structures. Based on the existing kinetic energy of outer flows in the LES. This treatment can also smooth oscillations of near-wall kinetic energy distribution in Figure 65. To achieve the above idea, (1) a dissipation rate or energy for a small structure is needed; and (2) an energy spectrum for interpolating energy in a proper size of rolls.

Finally, more tests are needed. Such as flow over periodic hills and backward steps, which can be further selected for validation and verification. Practical cases, such as flow around an airfoil and a wing-body shape can well present model performance in real applications.

References

[1] H. Choi and P. Moin, "Grid-point requirements for large eddy simulation : Chapman ' s estimates revisited," *Cent. Turbul. Res. Annu. Res. Briefs*, no. White 2005, pp. 31–36, 2011.

[2] J. LARSSON, S. KAWAI, J. BODART, and I. BERMEJO-MORENO, "Large eddy simulation with modeled wall-stress: recent progress and future directions," *Mech. Eng. Rev.*, vol. 3, no. 1, pp. 15-00418-15–00418, 2016, doi: 10.1299/mer.15-00418.

[3] L. Davidson and S. H. Peng, "Hybrid LES-RANS : a combination of a one-equation SGS model and a k-ω model for predicting recirculating flows," *Int. J. Numer. Methods Fluids*, vol. 43, no. November 2002, pp. 1003–1018, 2003.

[4] L. Temmerman, M. Hadžiabdić, M. A. Leschziner, and K. Hanjalić, "A hybrid two-layer URANS-LES approach for large eddy simulation at high Reynolds numbers," *Int. J. Heat Fluid Flow*, vol. 26, no. 2, pp. 173–190, 2005, doi: 10.1016/j.ijheatfluidflow.2004.07.006.

[5] A. Fadai-Ghotbi, C. Friess, R. Manceau, and J. Borée, "A seamless hybrid RANS-LES model based on transport equations for the subgrid stresses and elliptic blending," *Phys. Fluids*, vol. 22, no. 5, pp. 1–19, 2010, doi: 10.1063/1.3415254.

[6] N. V. Nikitin, F. Nicoud, B. Wasistho, K. D. Squires, and P. R. Spalart, "An approach to wall modeling in large-eddy simulations," *Phys. Fluids*, vol. 12, no. 7, pp. 1629–1632, 2000, doi: 10.1063/1.870414.

[7] P. R. Spalart, S. Deck, M. L. Shur, K. D. Squires, M. K. Strelets, and A. Travin, "A new version of detached-eddy simulation, resistant to ambiguous grid densities," *Theor. Comput. Fluid Dyn.*, vol. 20, no. 3, pp. 181–195, 2006, doi: 10.1007/s00162-006-0015-0.

[8] M. L. Shur, P. R. Spalart, M. K. Strelets, and A. K. Travin, "A hybrid RANS-LES approach with delayed-DES and wall-modelled LES capabilities," *Int. J. Heat Fluid Flow*, vol. 29, pp. 1638–1649, 2008, doi: 10.1016/j.ijheatfluidflow.2008.07.001.

[9] X. I. A. Yang, S. Zafar, J. X. Wang, and H. Xiao, "Predictive large-eddy-simulation wall modeling via physics-informed neural networks," *Physical Review Fluids*, vol. 4, no. 3. 2019, doi: 10.1103/PhysRevFluids.4.034602.

[10] F. Nicoud, J. S. Baggett, P. Moin, and W. Cabot, "Large eddy simulation wall-modelling based on suboptimal control theory and linear stochastic estimation," *Phys. Fluids*, vol. 13, no. 10, pp. 2968–2984, 2001, doi: 10.1063/1.1389286.

[11] S. T. Bose and P. Moin, "A dynamic slip boundary condition for wall-modeled large-eddy simulation," *Phys. Fluids*, vol. 26, no. 1, 2014, doi: 10.1063/1.4849535.

[12] H. J. Bae, A. Lozano-Durán, S. T. Bose, and P. Moin, "Dynamic slip wall model for large-eddy simulation," pp. 400–432, 2018, doi: 10.13140/RG.2.2.24150.09285.

[13] B. Krank, M. Kronbichler, and W. A. Wall, "Wall modeling via function enrichment: Extension to detached-eddy simulation," *Comput. Fluids*, vol. 0, pp. 1–8, 2018, doi: 10.1016/j.compfluid.2018.07.019.

[14] J. W. Deardorff, "A Numerical Study of Three-Dimensional Turbulent Channel Flow at Large Reynolds Number," vol. 41, no. 2, pp. 453–480, 1970.

[15] U. Schumann, "Subgrid-scale model for finite difference simulation of turbulent flows in plane channels and annuli," *J. Comput. Phys.*, vol. 18, pp. 376–404, 1975, doi: 10.1039/b914358k.

[16] U. Piomelli and E. Balaras, "Wall Layer Models for Large Eddy Simulations," *Annu. Rev.*

Fluid Mech., vol. 34, pp. 349–374, 2002, doi: 10.1146/annurev.fluid.34.082901.144919.
[17] U. Piomelli, "Progress in Aerospace Sciences Wall-layer models for large-eddy simulations," *Prog. Aerosp. Sci.*, vol. 44, pp. 437–446, 2008, doi: 10.1016/j.paerosci.2008.06.001.
[18] G. I. Park and P. Moin, "Space-time characteristics of wall-pressure and wall shear-stress fluctuations," *Phys Rev Fluids.*, p. 10.1103/PhysRevFluids.1.024404.
[19] F. Waleffe, "On a self-sustaining process in shear flows," *Phys. Fluids*, vol. 9, no. December 1996, pp. 883–900, 1997.
[20] F. Waleffe, "Hydrodynamic Stability and Turbulence: Beyond Transients to a Self-Sustaining Process," *Stud. Appl. Math.*, vol. 95, 1995.
[21] F. Waleffe and J. Kim, "How Streamwise Rolls and Streaks Self-sustain in a Shear Flow," in *Self-sustaining mechanisms of wall-bounded turbulence*, R.L. Panto., Computational Mechanics Publications, 1997.
[22] W. Schoppa and F. Hussain, "Coherent structure generation in near-wall turbulence," *J. Fluid Mech.*, vol. 453, pp. 57–108, 2002, doi: 10.1017/S002211200100667X.
[23] B. F. Farrell and P. J. Ioannou, "Dynamics of streamwise rolls and streaks in turbulent wall-bounded shear flow," *J. Fluid Mech.*, vol. 708, pp. 149–196, 2012, doi: 10.1017/jfm.2012.300.
[24] K. M. Butler and B. F. Farrell, "Three-dimensional Optimal Perturbations in Viscous Shear Flow," *Phys. Fluids*, vol. 4, pp. 1637–1650, 1992.
[25] V. L. Thomas, B. K. Lieu, M. R. Jovanović, B. F. Farrell, P. J. Ioannou, and D. F. Gayme, "Self-sustaining turbulence in a restricted nonlinear model of plane Couette flow," *Phys. Fluids*, vol. 26, no. 10, pp. 1–17, 2014, doi: 10.1063/1.4898159.
[26] T. Duriez, J. Aider, and J. E. Wesfreid, "Self-Sustaining Process through Streak Generation in a Flat-Plate Boundary Layer," *Phys. Rev. Lett.*, vol. 103, no. October, p. 144502, 2009, doi: 10.1103/PhysRevLett.103.144502.
[27] M. D. Graham and D. Floryan, "Exact Coherent States and the Nonlinear Dynamics of Wall-Bounded Turbulent Flows," *Annu. Rev. Fluid Mech.*, vol. 53, pp. 227–253, 2021, doi: 10.1146/annurev-fluid-051820-020223.
[28] J. S. Park and M. D. Graham, "Exact coherent states and connections to turbulent dynamics in minimal channel flow," *J. Fluid Mech.*, vol. 782, pp. 430–454, 2015, doi: 10.1017/jfm.2015.554.
[29] S. B. Pope, *Turbulent Flows*. Cambridge University Press, 2000.
[30] M. Lee and R. D. Moser, "Direct numerical simulation of turbulent channel flow up to Re $\tau \approx 5200$," *J. Fluid Mech.*, vol. 774, pp. 395–415, 2015.
[31] S. K. Robinson, "Coherent Motions in the Turbulent boundary layer," *Annu. Rev. Fluid Mech.*, vol. 23, pp. 601–639, 1991.
[32] B. S. J. Kline, W. C. Reynolds, F. A. Schraub, and P. W. Runstadlers, "The structure of turbulent boundary layers," *J. Fluid Mech.*, vol. 30, pp. 741–773, 1967.
[33] I. Marusic, G. J. Kunkel, and F. Porte-agel, "Experimental study of wall boundary conditions for large-eddy simulation," *J. Fluid ...*, vol. 446, pp. 309–320, 2001, doi: 10.1017/S0022112001005924.
[34] A. A. TOWNSEND, *the Structure of Turbulent Shear Flow*, no. (1976: 2ND ED.). Cambridge University Press, 1956.
[35] J. F. Morrison, "The interaction between inner and outer regions of turbulent wall-bounded

flow," *Philos. Trans. R. Soc. A Math. Phys. Eng. Sci.*, vol. 365, no. 1852, pp. 683–698, 2007, doi: 10.1098/rsta.2006.1947.

[36] D. B. Degraaff and J. K. Eaton, "Reynolds-number scaling of the flat-plate turbulent boundary layer," *J. Fluid Mech.*, vol. 422, pp. 319–346, 2000, doi: 10.1017/S0022112000001713.

[37] M. R. Head and P. Bandyopadhyay, "New aspects of turbulent boundary-layer structure," *J. Fluid Mech.*, vol. 107, no. 1981, pp. 297–338, 1981.

[38] Y. Guezennec, U. Piomelli, and J. Kim, "Conditionally-averaged structures in wall-bounded turbulent flows," 1987. [Online]. Available: https://www.researchgate.net/publication/234465051%0AConditionally-averaged.

[39] R. J. Adrian, C. D. Meinhart, and C. D. Tomkins, "Vortex organization in the outer region of the turbulent boundary layer," *J. Fluid Mech.*, vol. 422, pp. 1–54, 2000, doi: 10.1017/S0022112000001580.

[40] J. Zhou, R. J. Adrian, B. S., and K. T. M., "Mechanisms for generating coherent packets of hairpin vortices in channel flow," *J. Fluid Mech.*, vol. 387, pp. 353–396, 1999, doi: 10.1017/S002211209900467X.

[41] H. T. Corp, B. A. Singer, and R. D. Joslin, "Metamorphosis of a Hairpin Vortex into a Young Turbulent Spot," Hampton, VA, 1995. [Online]. Available: http://citeseerx.ist.psu.edu/viewdoc/download?doi=10.1.1.76.7609&rep=rep1&type=pdf.

[42] R. J. Adrian and R. J. Adrian, "Hairpin vortex organization in wall turbulence," *Phys. Fluids*, vol. 19, p. 041301, 2007, doi: 10.1063/1.2717527.

[43] E. R. Corino and R. S. Brodkey, "A visual investigation of the wall region in turbulent flow," *J . Fluid Mech.*, vol. 37, pp. 1–30, 1969.

[44] H. P. Bakewell and J. L. Lumley, "Viscous Sublayer and Adjacent Wall Region in Turbulent Pipe Flow," *Phys. Fluids*, vol. 10, pp. 1880–1889, 1967, doi: 10.1063/1.1762382.

[45] R. L. Panton, "Overview of the self-sustaining mechanisms of wall turbulence," *Prog. Aerosp. Sci.*, vol. 37, pp. 341–383, 2001.

[46] M. Wang and P. Moin, "Dynamic wall modeling for large-eddy simulation of complex turbulent flows," *Phys. Fluids*, vol. 14, no. 7, pp. 2043–2051, 2002, doi: 10.1063/1.1476668.

[47] W. H. Cabot and P. Moin, "Approximate wall boundary conditions in the large-eddy simulation of high Reynolds number flow," *Flow, Turbul. Combust.*, vol. 63, pp. 269–291, 1999, doi: 10.1023/A:1009958917113.

[48] S. Kawai and J. Larsson, "Dynamic non-equilibrium wall-modeling for large eddy simulation at high Reynolds numbers," *Phys. Fluids*, vol. 25, no. 1, 2013, doi: 10.1063/1.4775363.

[49] G. I. Park and P. Moin, "An improved dynamic non-equilibrium wall-model for large eddy simulation," *Phys. Fluids*, vol. 26, no. 1, 2014, doi: 10.1063/1.4861069.

[50] G. I. Park and P. Moin, "Numerical aspects and implementation of a two-layer zonal wall model for LES of compressible turbulent flows on unstructured meshes," *J. Comput. Phys.*, vol. 305, pp. 589–603, 2016, doi: 10.1016/j.jcp.2015.11.010.

[51] J. Calafell, F. X. Trias, O. Lehmkuhl, and A. Oliva, "A time-average filtering technique to improve the efficiency of two-layer wall models for large eddy simulation in complex geometries," *Comput. Fluids*, vol. 188, pp. 44–59, 2019, doi: 10.1016/j.compfluid.2019.03.026.

[52] G. I. Park, "Wall-modeled large-eddy simulation of a high reynolds number separating and

reattaching flow," *AIAA J.*, vol. 55, no. 11, pp. 3709–3721, 2017, doi: 10.2514/1.J055745.
[53] W. Cabot, "Near-Wall Models in Large Eddy Simulations of Flow Behind a Backward-Facing Step," *Annu. Res. Briefs—+ 1996*, p. 199, 1996.
[54] G. Hoffmann and C. Benocci, "Approximate wall boundary conditions for large eddy simultions," *Adv. Turbul. V proceeding fifith Eur. turbluence Conf.*, pp. 222–228, 1995.
[55] M. Wang, "Dynamic wall modeling for LES of complex," *Annu. Res. Briefs*, pp. 241–250, 2000.
[56] P. Catalano, M. Wang, G. Iaccarino, and P. Moin, "Numerical simulation of the flow around a circular cylinder at high Reynolds numbers," *Int. J. Heat Fluid Flow*, vol. 24, no. 4, pp. 463–469, 2003, doi: 10.1016/S0142-727X(03)00061-4.
[57] C. Duprat, G. Balarac, O. Métais, P. M. Congedo, and O. Brugière, "A wall-layer model for large-eddy simulations of turbulent flows with/out pressure gradient," *Phys. Fluids*, vol. 23, no. 1, 2011, doi: 10.1063/1.3529358.
[58] Z. L. Chen, S. Hickel, A. Devesa, J. Berland, and N. A. Adams, "Wall modeling for implicit large-eddy simulation and immersed-interface methods," *Theor. Comput. Fluid Dyn.*, vol. 28, no. 1, pp. 1–21, 2014, doi: 10.1007/s00162-012-0286-6.
[59] M. Wang, "LES with Wall Models for Trailing Edge Aeroacoustics," 1999. doi: 10.1.1.458.8697.
[60] X. I. A. Yang, J. Sadique, R. Mittal, and C. Meneveau, "Integral wall model for large eddy simulations of wall-bounded turbulent flows," *Phys. Fluids*, vol. 27, no. 2, 2015, doi: 10.1063/1.4908072.
[61] S. Hickel, E. Touber, J. Bodart, and J. Larsson, "A parametrized non-equilibrium wall-model for large-eddy simulations," 2012, doi: 10.13140/2.1.1281.6324.
[62] G. Grotzbach, "Direct numerical and large eddy simulations of turbulent channel flows," in *Encyclopedia of Fluid Mechanics*, N.P.Cherem., 1987, pp. 1337–1391.
[63] H. Reichardt, "Vollständige darstellung der turbulenten geschwindigkeitsverteilung in glatten leitungen . ZAMM-J. Appl. Math. Mech.," *J. Appl. Math. Mech.*, vol. 31, pp. 208–219, 1951.
[64] D. B. Spalding, "A single formula for the law of the wall," *J. Appl.*, pp. 455–458, 1961, [Online]. Available: http://arxiv.org/abs/cond-mat/9507132.
[65] U. Piomelli, J. Ferziger, P. Moin, and J. Kim, "New approximate boundary conditions for large eddy simulations of wall-bounded flows," *Phys. Fluids A*, vol. 1, no. 6, pp. 1061–1068, 1989, doi: 10.1063/1.857397.
[66] E. Balaras, C. Benoeei, and U. Piomelli, "Finite-Difference Computations of High Reynolds Number Flows Using the Dynamic Subgrid-scale Model," *Theor. Comput. Fluid Dyn.*, vol. 7, pp. 207–216, 1995.
[67] H. Werner and H. Wengle, "Large-Eddy Simulation of Turbulent Flow over a Square Rib in a Channel," in *Advances in Turbulence 2*, 1989, pp. 418–423.
[68] H. Werner and H. Wengle, "Large-Eddy Simulation of Turbulent Flow Over and Around a Cube in a Plate Channel," in *Turbulent Shear Flows 8*, 1993, pp. 155–168.
[69] S. Kawai and J. Larsson, "Wall-modeling in large eddy simulation: Length scales, grid resolution, and accuracy," *Phys. Fluids*, vol. 24, no. 1, 2012, doi: 10.1063/1.3678331.
[70] P. J. Mason and N. S. Callen, "On the magnitude of the subgrid-scale eddy coefficient in large-eddy simulations of turbulent channel flow," *J. Fluid Mech.*, vol. 162, pp. 439–462, 1986.

[71] X. Wu and K. D. Squires, “Prediction of the three-dimensional turbulent boundary layer over a swept bump,” *AIAA J.*, vol. 36, no. 4, pp. 505–514, 1998.
[72] C.-H. Moeng, “A large-eddy simulation model for the study of planetary boundary-layer turbulence,” *J. Atmos. Sci.*, vol. 41, pp. 2052–2062, 1984.
[73] Y. Maciel, T. Wei, A. G. Gungor, and M. P. Simens, “Outer scales and parameters of adverse-pressure-gradient turbulent boundary layers,” *J. Fluid Mech.*, vol. 844, pp. 5–35, 2018, doi: 10.1017/jfm.2018.193.
[74] G. L. Mellor, “The effects of pressure gradients on turbulent flow near a smooth wall,” *J. Fluid Mech.*, vol. 24, no. 2, pp. 255–274, 1966, doi: 10.1017/S0022112066000624.
[75] N. Afzal, “Wake Layer in a Turbulent Boundary Layer with Pressure Gradient: A New Approach,” no. November, pp. 95–118, 1996, doi: 10.1007/978-94-009-1728-6_9.
[76] M. Skote and D. S. Henningson, “Direct numerical simulation of a separated turbulent boundary layer,” *J. Fluid Mech.*, vol. 471, pp. 107–136, 2002, doi: 10.1017/S0022112002002173.
[77] Y. Hou, D. Angland, and X. Zhang, “A comparison of wall functions for bluff body aeroacoustic simulations,” *22nd AIAA/CEAS Aeroacoustics Conference, 2016*. 2016, doi: 10.2514/6.2016-2771.
[78] M. Manhart, N. Peller, and C. Brun, “Near-wall scaling for turbulent boundary layers with adverse pressure gradient : AAA priori tests on DNS of channel flow with periodic hill constrictions and DNS of separating boundary layer,” *Theor. Comput. Fluid Dyn.*, vol. 22, no. 3–4, pp. 243–260, 2008, doi: 10.1007/s00162-007-0055-0.
[79] M. Wang and P. Moin, “Dynamic wall modeling for large-eddy simulation of complex turbulent flows,” *Phys. Fluids*, vol. 14, no. 7, pp. 2043–2051, 2002, doi: 10.1063/1.1476668.
[80] T. J. Craft, A. V. Gerasimov, H. Iacovides, and B. E. Launder, “Progress in the generalization of wall-function treatments,” *Int. J. Heat Fluid Flow*, vol. 23, no. 2, pp. 148–160, 2002, doi: 10.1016/S0142-727X(01)00143-6.
[81] K. Suga, T. J. Craft, and H. Iacovides, “An analytical wall-function for turbulent flows and heat transfer over rough walls,” *Int. J. Heat Fluid Flow*, vol. 27, no. 5, pp. 852–866, 2006, doi: 10.1016/j.ijheatfluidflow.2006.03.011.
[82] K. Suga, T. Sakamoto, and Y. Kuwata, “Algebraic non-equilibrium wall-stress modeling for large eddy simulation based on analytical integration of the thin boundary-layer equation,” *Phys. Fluids*, vol. 31, no. 7, 2019, doi: 10.1063/1.5099658.
[83] S. Wilhelm, J. Jacob, and P. Sagaut, *A New Explicit Algebraic Wall Model for LES of Turbulent Flows Under Adverse Pressure Gradient*, vol. 106, no. 1. Springer Netherlands, 2021.
[84] P. R. Spalart, W. H. Jou, M. Strelets, and S. R. Allmaras, “Comments on the feasibility of LES for wings and on a hybrid RANS/LES approach,” *Adv. DNS/LES*, vol. 1, no. JANUARY, pp. 4–8, 1997, doi: 10.1006/jado.2001.0433.
[85] J. Smagorinsky, “General Circulation Experiments With the Primitive Equations: 1. The Basic Experiment,” *Mon. Weather Rev.*, vol. 91, no. 3, pp. 99–164, 1963, doi: 10.1126/science.27.693.594.
[86] P. R. Spalart and S. R. Allmaras, “A one-equation turbulence model for recirculating flows,” *La Rech Aerosp.*, vol. 1, pp. 5–21, 1994, doi: 10.1007/s11433-016-5800-1.
[87] F. R. Menter, M. Kuntz, and R. Langtry, “Ten Years of Industrial Experience with the SST Turbulence Model Turbulence heat and mass transfer,” *Cfd.Spbstu.Ru*, vol. 4, no. July 2014,

pp. 625–632, 2003, [Online]. Available: https://cfd.spbstu.ru/agarbaruk/doc/2003_Menter, Kuntz, Langtry_Ten years of industrial experience with the SST turbulence model.pdf%0Ahttp://cfd.mace.manchester.ac.uk/flomania/pds_papers/file_pds-1068134610Menter-SST-paper.pdf.

[88] A. K. Travin, M. L. Shur, P. R. Spalart, and M. K. Strelets, "Improvement of delayed detached-eddy simulation for LES with wall modelling," *Proc. Eur. Conf. Comput. Fluid Dyn. (ECCOMAS CFD 2006)*, vol. 47, no. 2, pp. 345–360, 2006.

[89] R. A. Baurle, C.-J. Tam, J. R. Edwards, and H. A. Hassan, "Hybrid Simulation Approach for Cavity Flows: Blending, Algorithm, and Boundary Treatment Issues," *AIAA Journal*, vol. 41, no. 8. pp. 1463–1480, 2003, doi: 10.2514/2.2129.

[90] J. U. Schlüter, X. Wu, S. Kim, S. Shankaran, J. J. Alonso, and H. Pitsch, "A Framework for Coupling Reynolds-Averaged With Large-Eddy Simulations for Gas Turbine Applications," *Journal of Fluids Engineering*, vol. 127, no. 4. p. 806, 2005, doi: 10.1115/1.1994877.

[91] L. Temmerman, M. A. Leschziner, and K. Hanjalic, "a-Priori Studies of a Near-Wall Rans Model Within a Hybrid Les/Rans Scheme," *Eng. Turbul. Model. Exp. 5*, vol. 0, pp. 317–326, 2002, doi: 10.1016/b978-008044114-6/50030-2.

[92] U. Piomelli, E. Balaras, H. Pasinato, K. D. Squires, and P. R. Spalart, "The inner-outer layer interface in large-eddy," *Int. J. Heat Fluid Flow*, vol. 24, pp. 538–550, 2003, doi: 10.1016/S0142-727X(03)00048-1.

[93] P. G. Tucker and L. Davidson, "Zonal k-l based large eddy simulations," *Comput. Fluids*, vol. 33, no. 2, pp. 267–287, 2004, doi: 10.1016/S0045-7930(03)00039-2.

[94] G. Park, X. Yang, and P. Moin, "The Cause and Resolution of Log-layer Mismatch in Wall modeled LES: a New Perspective and its Implication in Complex flows," *APS Division of Fluid Dynamics (Fall)*. 2017.

[95] X. I. A. Yang, G. I. Park, and P. Moin, "Log-layer mismatch and modeling of the fluctuating wall stress in wall-modeled large-eddy simulations," *Phys. Rev. Fluids*, vol. 2, no. 10, pp. 1–13, 2017, doi: 10.1103/PhysRevFluids.2.104601.

[96] J. Larsson, F. S. Lien, and E. Yee, "Feedback-controlled forcing in hybrid LES/RANS," *Int. J. Comut. Fluid Dyn.*, vol. 20, no. 10, pp. 687–699, 2006, doi: 10.1080/10618560701214724.

[97] J.-I. Choi, J. R. Edwards, and R. A. Baurle, "Compressible Boundary Layer Predictions at High Reynolds Number Using Hybrid LES RANS Methods," *AIAA J.*, vol. 47, no. 9, pp. 2179–2193, 2009.

[98] S. Jakirlic, S. Saric, B. Kniesner, G. Kadavelil, B. Basara, and B. Chaouat, "Sgs modelling in les of wall-bounded flows using transport rans models: From a zonal to a seamless hybrid les/rans method," *6th Int. Symp. Turbul. Shear Flow Phenomena, TSFP 2009*, vol. 2009-June, no. June, pp. 1057–1062, 2009.

[99] B. Krank and W. A. Wall, "A novel approach for wall modeling in LES of wall-bounded high-reynolds-number flow via function enrichment," *J. ofComputational Phys.*, 2015, doi: 10.1007/978-3-319-63212-4_23.

[100] T.-P. Fries, "A corrected XFEM approximation without problems in blending elements," *Int. J. Numer. Meth. Engng*, vol. 75, pp. 503–532, 2008, doi: 10.1002/nme.

[101] H. T. Kim, S. J. Kline, and W. C. Reynolds, "The production of turbulence near a smooth wall in a turbulent boundary layer," *J. Fluid Mech.*, vol. 50, no. 1, pp. 133–160, 1971, doi: 10.1017/S0022112071002490.

[102] Y. Hwang and Y. Bengana, "Self-sustaining process of minimal attached eddies in turbulent

channel flow," *J. Fluid Mech.*, vol. 795, pp. 708–738, 2016, doi: 10.1017/jfm.2016.226.
[103] J. M. Hamilton, J. Kim, and F. Waleffe, "Regeneration mechanisms of near-wall turbulence structures," *J. Fluid Mech.*, vol. 287, pp. 317–348, 1995.
[104] "Johns Hopkins Turbulence Database (JHTDB)." http://turbulence.pha.jhu.edu/webquery/query.aspx.
[105] T. Wei, P. Fife, J. Klewicki, and P. McMurtry, "Properties of the mean momentum balance in turbulent boundary layer, pipe and channel flows," *J. Fluid Mech.*, vol. 522, no. April 2014, pp. 303–327, 2005, doi: 10.1017/S0022112004001958.
[106] R. D. Moser, J. Kim, and N. N. Mansour, "Direct numerical simulation of turbulent channel flow up to Reτ=590," *Physics of Fluids*, vol. 11, no. 4. pp. 943–945, 1999, doi: 10.1063/1.869966.
[107] P. R. Spalart, "Direct simulation of a turbulent boundary layer up to Rθ= 1410," *J. Fluid Mech.*, vol. 187, no. December, pp. 61–98, 1988, doi: 10.1017/S0022112088000345.
[108] M. V. Zagarola and A. J. Smits, "Mean-flow scaling of turbulent pipe flow," *J. Fluid Mech.*, vol. 373, pp. 33–79, 1998, doi: 10.1017/S0022112098002419.
[109] J. Jiménez and A. Pinelli, "The autonomous cycle of near-wall turbulence," *J. Fluid Mech.*, vol. 389, pp. 335–359, 1999, doi: 10.1017/S0022112099005066.
[110] N. Hutchins and I. Marusic, "Large-scale influences in near-wall turbulence," *Philos. Trans. R. Soc. A Math. Phys. Eng. Sci.*, vol. 365, no. 1852, pp. 647–664, 2007, doi: 10.1098/rsta.2006.1942.
[111] B. Ganapathisubramani, N. Hutchins, J. P. Monty, D. Chung, and I. Marusic, "Amplitude and frequency modulation in wall turbulence," *J. Fluid Mech.*, vol. 712, pp. 61–91, 2012, doi: 10.1017/jfm.2012.398.
[112] H. Wang and Q. Gao, "A study of inner-outer interactions in turbulent channel flows by interactive POD," *Theor. Appl. Mech. Lett.*, vol. 11, no. 1, p. 100222, 2021, doi: 10.1016/j.taml.2021.100222.
[113] P. S. Iyer and M. R. Malik, "Wall-modeled les of the nasa juncture flow experiment," *AIAA Scitech 2020 Forum*, vol. 1 PartF, no. January, pp. 1–23, 2020, doi: 10.2514/6.2020-1307.
[114] J. Bodart AND J. Larsson, "Wall-modeled large eddy simulation in complex geometries with application to high-lift devices," *Cent. Turbul. Res. Annu. Res. Briefs*, p. 37, 2011, doi: 10.1520/E2168-06.2.
[115] P. Studies, "LARGE EDDY SIMULATION OF WALL-BOUNDED TURBULENT FLOWS AT HIGH REYNOLDS NUMBERS Hadi Hosseinzade Halqesari," no. May, 2022.